

# Untethered Microrobots of the Rolling, Jumping & Flying kinds

*Palak Bhushan  
Claire Tomlin*



Electrical Engineering and Computer Sciences  
University of California at Berkeley

Technical Report No. UCB/EECS-2019-128

<http://www2.eecs.berkeley.edu/Pubs/TechRpts/2019/EECS-2019-128.html>

August 16, 2019

Copyright © 2019, by the author(s).  
All rights reserved.

Permission to make digital or hard copies of all or part of this work for personal or classroom use is granted without fee provided that copies are not made or distributed for profit or commercial advantage and that copies bear this notice and the full citation on the first page. To copy otherwise, to republish, to post on servers or to redistribute to lists, requires prior specific permission.

**Untethered Microrobots of the Rolling, Jumping & Flying kinds**

by

Palak Bhushan

A dissertation submitted in partial satisfaction of the

requirements for the degree of

Doctor of Philosophy

in

Engineering - Electrical Engineering and Computer Sciences

in the

Graduate Division

of the

University of California, Berkeley

Committee in charge:

Professor Claire Tomlin, Chair

Professor Ronald Fearing

Professor Kristofer Pister

Professor Liwei Lin

Summer 2019

# **Untethered Microrobots of the Rolling, Jumping & Flying kinds**

Copyright 2019  
by  
Palak Bhushan

## Abstract

Untethered Microrobots of the Rolling, Jumping & Flying kinds

by

Palak Bhushan

Doctor of Philosophy in Engineering - Electrical Engineering and Computer Sciences

University of California, Berkeley

Professor Claire Tomlin, Chair

In this dissertation we study microrobot design for three modes of locomotion, namely rolling, jumping, and flying. This work covers power electronics, actuator and mechanical transmission design for these types of microrobots along with power source selection. Though interesting, we do not cover the sensors, controllers/computers, communications and useful payloads for these bots. This remains a topic for future work.

Piezoelectric and electrostatic actuators generally have been the actuators of choice for researchers working in microrobotics, since conventional electromagnetic motor designs don't scale down well. Here we design an electromagnetic actuator in a way that significantly reduces its scaling down disadvantages, while still retaining its original advantages. This has enabled us to achieve untethered operation for our bots, which is one of the coveted goals for researchers working in this domain. Though untethered rolling and jumping is demonstrated, the untethered flying bot reported in this dissertation remains underpowered and doesn't take flight yet.

First a micro-ratcheting mechanism is developed as a means to convert small periodic motions of actuators to continuous rotational motion. A supercapacitor, a fixed frequency H-bridge, and a low-voltage electromagnetic actuator is then used to drive this micro-ratchet to achieve untethered rolling motion for 8 seconds at 27mm/s. At 130mg mass, this is the lightest and fastest untethered rolling microrobot reported yet.

The same continuous rotation mechanism developed for the rolling bot is then used to load a spring in an energy storage mechanism that can then release the stored energy rapidly and passively, via use of magnets, after the stored energy crosses a certain threshold. In this case, the continuous rotation mechanism is driven using laser-powered photovoltaic cells and untethered jumping up to heights of 8mm is demonstrated. At 75mg mass, it is the lightest untethered jumping microrobot with onboard power source.

Next, a highly efficient resonant low-voltage electromagnetic actuator is developed to generate insect-like flapping wing motion. It is demonstrated to produce 90% of its weight in lift. Further light-weight and power-efficient power electronics are developed to power this actuator using laser-powered photovoltaic cells. The designed power electronics are an

order of magnitude lighter and two orders of magnitude more efficient than all other power electronics units reported yet for flying microrobots. While sufficient lift for flight is not achieved, due to the actuator being underpowered because of power source overheating, untethered flapping wing motion is demonstrated.

To provide inspiration to future generations of microroboticists, a fruit fly scale flapping winged robot is developed. At 0.7mg mass, even though tethered, it is the lightest and smallest bot to demonstrate flapping wing kinematics.

To all the teachers in my life.

# Contents

<b>Contents</b>	<b>ii</b>
<b>List of Figures</b>	<b>iv</b>
<b>List of Tables</b>	<b>ix</b>
<b>1 Introduction</b>	<b>1</b>
1.1 What Are Microrobots? . . . . .	2
1.2 Previous Work and Challenges . . . . .	3
1.3 Solutions to Common Challenges . . . . .	7
1.4 Common Design Framework . . . . .	9
1.5 This Work . . . . .	10
<b>2 Rolling <math>\mu</math>bot</b>	<b>11</b>
2.1 Micro-ratchet . . . . .	11
2.2 Double-ratchet . . . . .	13
2.3 Electromagnetic Actuator . . . . .	14
2.4 Starting Torque & Mechanical Losses . . . . .	15
2.5 Power Electronics . . . . .	18
2.6 Assembly . . . . .	19
2.7 Rolling Using Photovoltaics . . . . .	20
2.8 Rolling Using Supercapacitor . . . . .	22
2.9 Summary . . . . .	22
<b>3 Jumping <math>\mu</math>bot</b>	<b>25</b>
3.1 Underlying Principle . . . . .	25
3.2 Spring Design . . . . .	26
3.3 Spring Loading Mechanism . . . . .	26
3.4 Spring Release Mechanism . . . . .	27
3.5 Shaft Rotation Mechanism . . . . .	28
3.6 Assembly . . . . .	29
3.7 Starting Torque . . . . .	30

3.8	Jumping Using External Power . . . . .	33
3.9	Jumping Using Photovoltaics . . . . .	34
3.10	Summary . . . . .	35
<b>4</b>	<b>Flapping Wing <math>\mu</math>bot</b>	<b>39</b>
4.1	Design Choices . . . . .	39
4.2	Electromagnetic Actuator . . . . .	41
4.3	Increasing Coil's Travel . . . . .	43
4.4	Mechanical Transmission . . . . .	44
4.5	Spring Material Choice . . . . .	45
4.6	Spring Energy Density . . . . .	46
4.7	Spring Design . . . . .	47
4.8	Spring Non-idealities . . . . .	49
4.9	Wing Fabrication . . . . .	49
4.10	Assembly . . . . .	50
4.11	Power Efficiency . . . . .	53
4.12	Flapping Motion Using External Power . . . . .	53
4.13	Further Increasing Actuator Efficiency . . . . .	57
4.14	Power Electronics . . . . .	61
4.15	Flapping Motion Using Photovoltaics (Without Wings) . . . . .	64
4.16	Flapping Motion Using Photovoltaics (With Wings) . . . . .	66
4.17	Summary . . . . .	66
<b>5</b>	<b>Sub-milligram Flapping Wing <math>\mu</math>bot</b>	<b>68</b>
5.1	Electromagnetic Actuator . . . . .	68
5.2	Wing Fabrication . . . . .	69
5.3	Assembly . . . . .	70
5.4	Flapping Motion Using External Power . . . . .	73
5.5	Summary . . . . .	73
<b>6</b>	<b>Conclusion and Future Work</b>	<b>77</b>
6.1	Rolling $\mu$ bot . . . . .	77
6.2	Jumping $\mu$ bot . . . . .	78
6.3	Flying $\mu$ bot . . . . .	78
6.4	Sub-milligram flying $\mu$ bot . . . . .	79
	<b>Bibliography</b>	<b>80</b>

# List of Figures

1.1	Basic building blocks for $\mu$ bots. . . . .	3
1.2	Relevant (to this work) subsystems for a real insect. . . . .	3
1.3	Classification of $\mu$ bots with increasing capability and complexity. . . . .	4
1.4	$\mu$ Bot classification based on locomotion strategy. . . . .	4
1.5	Biomimetic wing trajectory for use in flapping wing $\mu$ bots. . . . .	6
1.6	Composite 4-bar-type mechanical transmission used in prior flapping wing bots. . . . .	6
1.7	Challenges and performance metrics for the different building blocks of $\mu$ bots. . . . .	8
1.8	Common framework for all $\mu$ bots in this work. . . . .	10
2.1	Cross-section of a micro-ratchet mechanism made using flexible beams on a shaft and a patterned hole. The peaks in the pattern are $25\mu\text{m}$ high and are spaced $4^\circ$ , or, approximately $70\mu\text{m}$ apart. . . . .	12
2.2	Fabrication of the shaft for the micro-ratchet mechanism. $60^\circ$ spaced flexible beams are obtained by wrapping a laser cut Kapton sheet with tabs on to a Kapton tube. . . . .	12
2.3	(a) Laser-cut patterned steel rings are slid in to the shaft such that (b) the ring passes through the slots in each of the tabs/elastic beams. (c) & (d) show a better view of the rings passing through the slots. . . . .	13
2.4	Operation principle of the double ratchet. . . . .	14
2.5	Fabricated double ratchet corresponding to Fig. 2.4. Seen in black are the 0.3mm CF rods that join the pairs of rings. . . . .	15
2.6	Double-ratchet mechanism operated manually, and thus time stamps are just indicative. Input is provided at the back ratchet, and output is observed using the black CF indicator rod attached perpendicularly to the shaft. Asymmetry in clockwise vs anti-clockwise operation can be observed. . . . .	16
2.7	An electromagnetic actuator (magnet + coil) driving the input ratchet via a long moment arm. Rings and coil supports are attached to a common base plate that acts as a mechanical ground. . . . .	17
2.8	A long narrow slot in the alignment plate keeps the moment arm in a single plane. This slot also restricts the moment arm from rotating more than $\approx 12^\circ$ . . . . .	18

2.9	Conceptual circuit diagram. Supercapacitor acts as the supply for the coil, oscillator and the H-bridge. The standard opamp based oscillator circuit functions by charging and discharging the capacitor C, whose time constant is tuned using R.	19
2.10	Actual circuit. (a) To avoid any manual alignment copper traces are laser-cut in place, and then the Kapton + adhesive laminate is hot pressed on to it. (b) The surface mount electrical components are glued and soldered in place manually.	20
2.11	Fully assembled device. The supercapacitor is kept close to the ground so that it can be charged using probes from a function generator and then released quickly.	21
2.12	(a) Supercapacitor powered rolling microbot. Compared to (b) an index finger, and, (c) a quarter dollar. . . . .	22
2.13	Stationary laser-powered bot with continuously rotating but slipping wheels. The wheels are made to slip by smoothening it out (eliminating the spikes) and then placing them at a bump that they cannot climb due to low traction. . . . .	23
2.14	Microrobot rolling forwards in real time. The bot is operated over a piece of paper for better traction and to avoid any slipping between the spiked wheels and the level surface. . . . .	24
3.1	Underlying principle of the jumping bot. (a) Neutral state of the spring. (b) Spring deflected by the maximum amount storing potential energy. (c) Released spring just before losing ground contact. (d) Bot at the maximum jump height.	25
3.2	(a) Planar spring design showing connection slots later used to attach parts perpendicularly to the spring. (b), (c) & (d) Different views of the stand and feet glued to the spring. . . . .	26
3.3	Different views of the spring at full deflection (FEA). . . . .	27
3.4	Spring loading mechanism tested on a simple leaf spring. . . . .	28
3.5	Passive spring release concept using magnets. . . . .	29
3.6	Passive spring release in action. (a) Spring at maximum deflection just before the magnets snap. (b) String vibrating just after the release. (c) String vibrations dampening over time. . . . .	30
3.7	The double ratchet mechanism used to produce continuous rotation motion. (a) Shaft colored in blue. (b) All parts acting as one rigid part colored in blue. . .	31
3.8	(a) & (b) Two extreme positions of the moment arm separated by $\approx 2^\circ$ rotation. (c) & (d) Magnet limiter in action. . . . .	32
3.9	Fully assembled bot compared with a millimeter ruler. . . . .	33
3.10	(a) Jumping $\mu$ bot, with (b) a quarter dollar, and, (c) an index finger. . . . .	34
3.11	The 2 extreme ratchet positions, separated by $\approx 2^\circ$ . Also seen is the small magnet from the release mechanism. . . . .	35
3.12	Spring loading in conjunction with the double-ratchet. . . . .	36
3.13	Tethered jump of the bot using external power supply. . . . .	37
3.14	Circuit with 2 PV cells for tetherless $\mu$ bot operation. . . . .	38
3.15	Tetherless jump of the $\mu$ bot using laser power. . . . .	38

4.1	Lorentz force and the relative motion between the coil and magnet. . . . .	42
4.2	Simulation of generated back emf using equation 4.4 for $h = 3.1\text{mm}$ and $f = 100\text{Hz}$ . Simulation interval is 25% of the motion cycle from zero to full positive (+ $h$ ) relative separation between the coil and magnet (with the complete cycle comprised of 4 parts in this order: 0 to + $h$ , + $h$ to 0, 0 to $-h$ and $-h$ to 0.). This operating point corresponds to the 2 <sup>nd</sup> row in Table 4.4. . . . .	42
4.3	Effect of doubling the coil's travel on the various quantities. . . . .	43
4.4	Effect of doubling the coil's travel on heat dissipation. . . . .	44
4.5	Integrating transmission into the actuator to directly output biomimetic kinematics. . . . .	45
4.6	Fatigue in spring materials. Choosing spring material based on fatigue limit. . . . .	46
4.7	Spring energy density for different modes of beam bending. . . . .	46
4.8	(a) A single cantilever beam in constant-curvature bending. (b) N cantilever beams in series, with 2 such groups arranged to act in parallel, making total number of beams=2N. (c) Dominant resonant mode of operation of the spring + resonant mass system, with the resonant mass modeling the magnet placed at 4mm from the rotation axis. Color coding represents displacement. (d) Torsional rotation of $\theta_{\text{rot}} = 60^\circ$ as seen in the fabricated $\mu\text{bot}$ . (e) Progressively increasing rotation of the spring as one moves towards the center. The small rotations of the individual beams add up. . . . .	47
4.9	Constant surface stresses. . . . .	48
4.10	Desired and parasitic resonant modes of the spring-mass system. . . . .	48
4.11	Spring stress concentrations and filleting. (b) Higher stresses seen near a sharp corner. (b) Lower stresses seen near a more rounded corner. . . . .	50
4.12	Spring non-idealities. (a) Stress gradient across the length of the beams caused due to the (b) dynamic shifts in the rotation axis. . . . .	51
4.13	Wing fabrication assembly. The layup consists of (a) $0^\circ$ - $60^\circ$ - $0^\circ$ aligned $30\mu\text{m}$ -thick CF prepreg layers laser-cut to act as $60\mu\text{m}$ wide veins, (b) A wider CF leading edge creating a gap of $300\mu\text{m}$ for the flexure, (c) Three $12.7\mu\text{m}$ thick Kapton beams on the leading edge gap acting as a flexure hinge, (d) $2.5\mu\text{m}$ Mylar acting as wing membrane. . . . .	51
4.14	Different parts of the $\mu\text{bot}$ . . . . .	52
4.15	Different views of the fabricated $\mu\text{bot}$ . (a) Front view comparison with a ruler showing wing-span of 3cm. (b) Side view showing clearance between the coil and the magnet. (c) Top view showing semi-circular magnet frame. (d) Top view at an extreme stroke position. (e) Perspective view. (f) Perspective view at an extreme stroke position. . . . .	52
4.16	Effective circuit diagram of the EM actuator and the set-up for measuring $V_{\text{emf}}$ . . . . .	54
4.17	(a)-(g) 25% of cycle with $\theta_{\text{rot}}(t)$ from mid-stroke to mid-stroke showing wing pitch reversal (top view). (i) Stroke amplitude measurement between 2 extreme wing positions. . . . .	55
4.18	25% of cycle between highest angle-of-attack positions showing wing pitch reversal (perspective view). . . . .	56

4.19	Most negative and most positive wing angle-of-attack seen during mid-stroke (side view).	56
4.20	Setup for the measurement of average lift.	57
4.21	Intended route of the coil through the double magnet assembly.	58
4.22	Worst case clearance between the coil and the magnet.	58
4.23	Steps in precision assembly of the 2 magnets.	59
4.24	Low out-of-plane spring stiffness skewing the coil's trajectory.	60
4.25	Diametrically opposite counter-mass to balance the coil.	61
4.26	Electronics acting as the counter-mass in the assembled device.	61
4.27	Plot of $V_{\text{emf}}(t)$ in the actuator, and the structure of the sensing system acting on the actuator.	62
4.28	Conceptual circuit diagram of the proposed electronics.	62
4.29	Fabricated 9mg circuit, compared to an index finger.	63
4.30	Stability of mechanical + actuator + electronics joint system.	63
4.31	Assembled device.	65
4.32	Snapshots of the device without wings in motion.	66
4.33	Snapshots of the device with wings in motion.	67
5.1	Magnet motion. The desired circular arc the magnet should move in. The motion is simple harmonic in the magnet's rotation angle with $\pm 45^\circ$ amplitude.	69
5.2	Spring motion. The designed torsion spring in its extreme top, neutral, and extreme bottom positions. This shows the intended circular trajectory of the magnet.	69
5.3	Steps of wing fabrication. (a) CF veins are laser cut from a unidirectional single layer $30\mu\text{m}$ -thick CF sheet. The fibers are oriented vertically. (b) Laser cut veins are aligned and adhered to a polyester film using $18\mu\text{m}$ -thick adhesive layer. (c) The resulting sandwich is laser cut to remove the excess CF and to form the flexures. (d) Released wing.	71
5.4	Assembled device, animation. Axes defined with respect to the assembled body. The shadow shows the concentricity of the coil and the magnet, and the clearance between them.	71
5.5	Assembled device. (Top) Comparison with a quarter dollar coin. (Middle) Front, side and top views of the device. Front viewed is pictured with a millimeter ruler. (Bottom) Perspective view of the device, and comparison with an index finger.	72
5.6	Magnet motion snapshots, top view. Extreme right, neutral, and extreme left positions of the moving magnet plus spring system. (Top) An animation of magnet and spring positions. (Bottom) Snapshots of the fabricated device in motion, with Copper coil being stationary.	74
5.7	Wing pitch, top view. (Top) Positive wing pitch (that is, positive angle of attack) while moving to the right. A maximum pitch of $30^\circ$ is observed. Zero pitch observed at extreme stroke angle. (Bottom) Wing pitch reversed while moving to the left. Maximum pitch of $50^\circ$ observed. Zero pitch at extreme stroke angle.	75

5.8	Wing pitch, side view. Wing pitch reversal at the end of a stroke cycle (that is, near an extreme stroke angle). The X-shaped CF frame stops the wing from pitching further after reaching a certain angle of attack. This limiting can be seen more clearly in Fig. 5.9. . . . . .	76
5.9	Wing pitch, front view. Wing pitch amplitude increases as the mechanism's stroke speed increases. The X-shaped CF frame hard-limits the pitch magnitude. . . .	76

# List of Tables

1.1	Summary of flying $\mu$ bots. . . . .	7
2.1	Mass distribution of the rolling $\mu$ bot. . . . .	23
3.1	Mass distribution of the jumping $\mu$ bot. . . . .	32
4.1	Steel vs Titanium as the spring material. . . . .	45
4.2	Spring Specs. . . . .	49
4.3	Mass distribution. . . . .	53
4.4	Predicted (/simulated) and measured heat loss and efficiency values. . . . .	54
4.5	Summary of $\mu$ bot Specs. . . . .	55
4.6	Mass distribution of the laser-powered flying $\mu$ bot. . . . .	65
5.1	Spring specifications. . . . .	70
5.2	Mass distribution. . . . .	73

## Acknowledgments

I would foremost like to thank my advisor Claire for all the freedom and support she gave me in exploring this vast field of robotics. My thesis topic would have been different (worse kind of different) and less entertaining if not for her. I would like to thank Ron and Kris for inspiring me to work in the field of microrobots, for their generosity in sharing their lab space, and their students Ethan and Dan for training me on their lab equipments. Some of the robots in this work wouldn't have been possible without the endless discussions I had with my parents explaining them the manufacturing challenges I was currently facing and hearing their dozens of ideas on how to solve them. My sister and my friends have been the sources to recharge my battery and start afresh - I feel lucky to have made many memorable trips with them. My sister also helped me write this introduction. Lastly I would like to thank my car for providing me endless thrills when no one else could.

# Chapter 1

## Introduction

Microrobots have a myriad of potential applications including, but not limited to, active remote sensor nodes, agents for robotic surgery, cooperative swarms to search for earthquake and other disaster survivors, reconnaissance, and exploration of new planets. This range of applications is due to their expected insect-like maneuverability, navigation over tough terrains, and potential for swarm behavior, all of it owing to their small size and the promise for mass production. The idea is if 1000 small 100mg robots are used in place of one big 100g robot, this multiplicity would expectedly more than compensate for any deterioration in sensor quality and locomotion per unit, while exponentially increasing the swarm's operational range and robustness to failure.

There is lot of ongoing effort to manufacture cheap sensors on the scale of trillions to collect information on a spatiotemporal scale never seen before. These sensors mainly act passively. One of the applications of cm-scale microrobots is then in being deployed as active sensor-actuator nodes, on a scale of billions, that can interact with their environment in much diverse ways, along with the ability of long distance locomotion and indefinite maintenance-free operation. Such an active sensor-actuator network can be imagined to be dispersed via a fractal approach with larger flight systems releasing 100x smaller systems (unmanned fixed-wing aircrafts distributing meter-scale quadcopters – which in turn disperses cm-scale microrobots), and could operate in this tree-like or hub-and-spoke-like communication model as well. Although the passive and active nodes will be used in conjunction, an active node will be orders of magnitude more powerful than its passive counterpart in its information collecting and processing capabilities, thus requiring fewer numbers. The active property opens endless possibilities for such a large network, with applications like artificial pollination, tackling forest fires, and, assessing and responding to scenarios where timing is crucial, over and above active sensor data collection. The swarm behavior potentially provides a way to manipulate the environment at a variable scale way larger than the local scale thus causing the small scale to not be a limiting factor when it comes to the actuation aspects of the network.

The film industry and media have done their fair share in hyping the abilities of these small robots and make their abilities look surprisingly natural. None of the application ideas

mentioned above, however, have currently been realized and look distant. So instead of expanding our list on these potential applications, we focus our attention on the challenges faced by microrobots today and on how to design the next generation of microrobots. Just like the internet, we hope that the applications will become more clear after we have a working platform.

## 1.1 What Are Microrobots?

Before going any further, we would first like to properly define microrobots and their subsystems, and classify them based on their complexity. This will help us better understand previous works in the field, the challenges faced in making them, and our contributions. The term *microrobots* is generally used for insect-sized robots in the centimeter-scale and approximately 100mg in mass, and that is how we will be using this term here. The term, however, is often misused (perhaps we are the ones misusing it) which is fine since the size becomes clear from the context in the research works. Robots that are  $100\mu\text{m}$  or smaller in size are called nanobots and are outside the scope of this work. Here we will use the terms microrobots, microbots,  $\mu$ bots and bots interchangeably.

### Subsystems in a $\mu$ bot

$\mu$ Bots, just like any other robotics system, are composed of some basic building blocks (see Fig. 1.1). There is a power source (like a Lithium battery) that drives the actuator (like an induction motor) through some power electronics (like an inverter). This power electronics accomplishes what is called *electrical impedance matching* between the power source and the actuator. The actuator motion (like motor shaft rotation) is then converted via a transmission (like gears and pulleys) to the end effector motion (like the motion of wheels). The transmission achieves what is called *mechanical impedance matching* between the actuator and the end effector. The end effector then acts on the environment (like a dirt road) to accomplish certain tasks (like achieving fast accelerations). Some useful sensors (like LIDARs) and controllers (like GPU-powered AI) also help the  $\mu$ bot operate autonomously. In this work we won't talk about the brain or sensors onboard our  $\mu$ bots, but instead only deal with the mechanical and electrical components design. An example subsystem decomposition for an insect is shown in Fig. 1.2 with all the subsystems we would be interested in.

### $\mu$ Bot classification

Depending on which blocks are present in the  $\mu$ bots in question, they would fall into one of these sets (see Fig. 1.3). The set of all  $\mu$ bots includes those that need tethers like external electrical wires to operate. Next, the locally untethered kind need a well constructed environment very different from outdoors to operate, like a changing external magnetic field

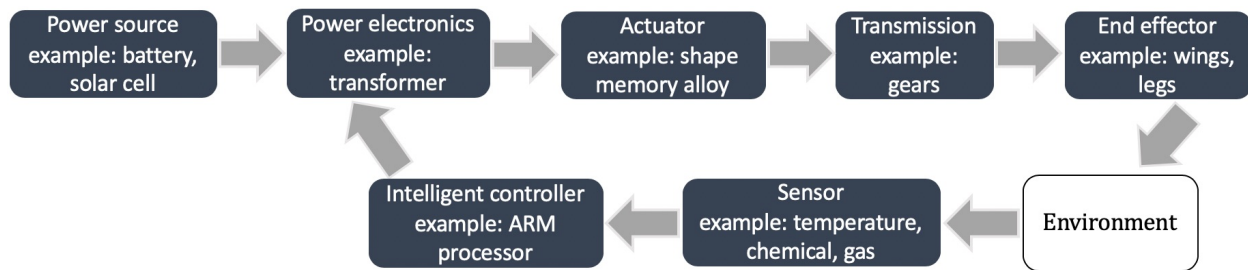
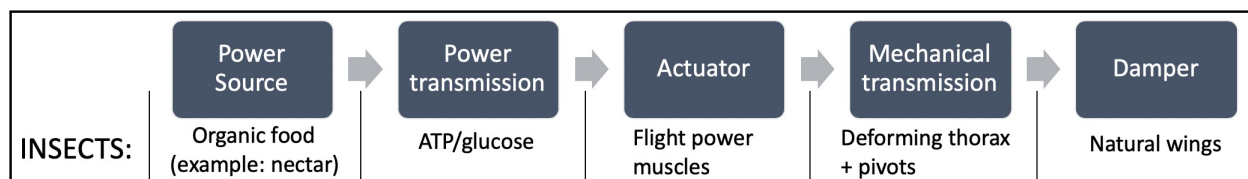
Figure 1.1: Basic building blocks for  $\mu$ bots.

Figure 1.2: Relevant (to this work) subsystems for a real insect.

or a hot plate to provide heat energy. We are only interested in the globally untethered set whose architecture is such that it **permits the eventual addition of future micro-batteries or solar cells**. Significant research needs to be done on such onboard power sources that can power these bots for hours to make them self-sufficient. Research on making autonomous controllers (or, brains) for these  $\mu$ bots is ongoing in order to make these think for themselves just like insects do. The deepest anyone has reached in this set is barely touching the self-sufficient bots class. Through this work we will land well within the self-sufficient set.

## 1.2 Previous Work and Challenges

$\mu$ Bots can utilize a variety of locomotion strategies to navigate around the world, including crawling, rolling, walking, jumping and flying. Among these  $\mu$ bots, the flying kind are well heard of due to their visually appealing nature and flapping wing kinematics, together with the inherent difficulty in making these owing to the high power demand of flight [31, 48, 6, 5]. Thus insect-scale flying  $\mu$ bots are all tethered with the exceptions of [26, 25] but even those take off just for a split second on photovoltaic power before falling to the ground.

The design requirements for ground-based  $\mu$ bots however are much relaxed compared to those of flying ones [27], in part due to the fact that they are not required to lift their own weight. Yet there have been very few 100mg-scale robots that are self-sufficient [23]. Most of the electrical-powered designs are tethered [14, 36], due to the high-voltage, high-current,

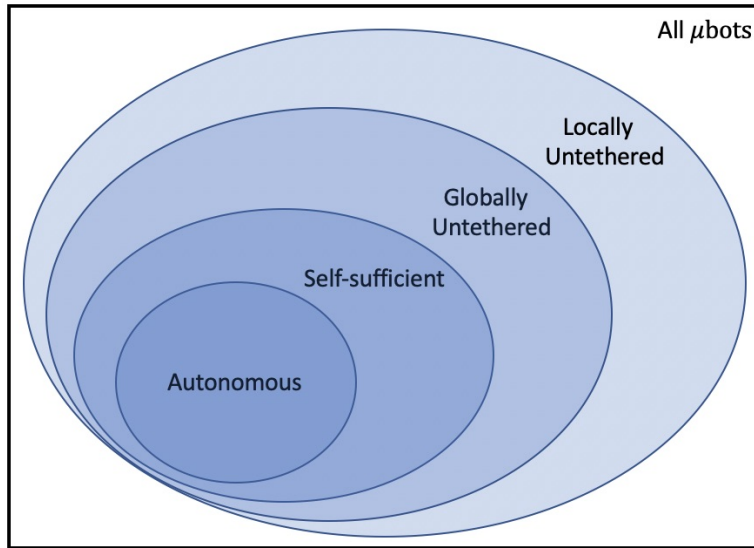


Figure 1.3: Classification of  $\mu$ bots with increasing capability and complexity.

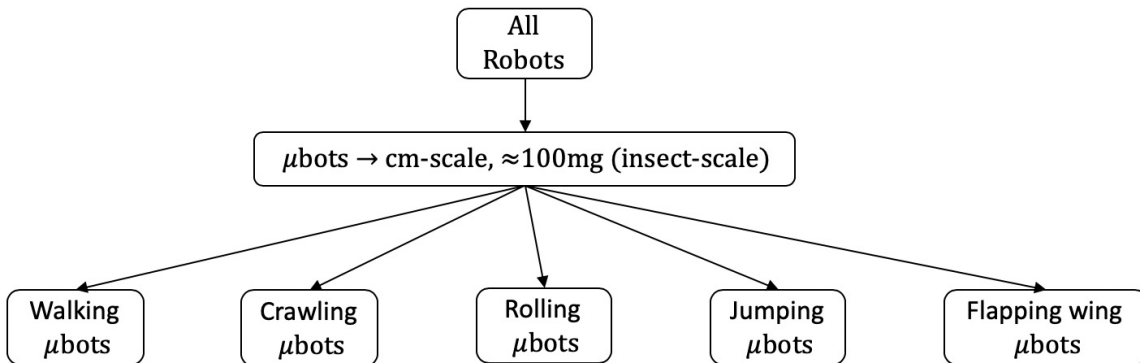


Figure 1.4:  $\mu$ Bot classification based on locomotion strategy.

and/or, high-power demands on the drive electronics and the power source.

There have been prior crawlers that are untethered but these mostly require a controlled environment, like a changing external field [34] or an electrical grid surface [16] to function, restricting their global operation. Recently a self-sufficient bot was reported [35] weighing 200mg with a supercapacitor as its power source. It crawls for 10 seconds at 2mm/s just like a bristlebot, that is, using an anisotropic forward versus backward friction coefficient between its legs and the ground. But this makes the bot's motion very sensitive to the surface properties, with rougher surfaces potentially rendering it useless.

Crawlers are less robust to the ever changing environment compared to rollers and walkers, followed by jumpers [3], with flyers being the most robust among these. Robustness generally increases the less the bot interacts with the environment especially with its mul-

titude of surfaces. Jumpers and flyers minimize this interaction by jumping/flying over the obstacles and to their next destination.

Untethered jumping has been demonstrated before using mechanical and chemical approaches. [12] reports an 8mg spring-mass device that can jump up by 32cm by rapidly releasing mechanical energy stored in a spring, but the device was loaded and released manually and has no actuators. [13] reports a 300mg bot that can jump up by 8cm using explosive chemical energy, but the capacitors in the igniting circuit needs to be charged manually for each jump. Another 34mg jumper reported in [29] jumps up by 30cm but it requires a controlled environment, namely a hot plate, to transfer energy to its SMA (shape memory alloy) actuators in order to jump. Moreover, high current consumption of SMA actuators will be a hinderance in making this design globally untethered. Apart from the needed manual intervention and/or a controlled environment, the downside is that all these bots can jump only once. Note that even if the chemical jumper had multiple independent chemical packets to release the explosive energy multiple times, the jumps it would do won't be repeatable indefinitely since the onboard fuel sources will get used up after some time.

Speaking about repeatability, [21] reports a silicon jumping  $\mu$ bot which being electrically powered can in principle jump indefinitely as long as it has power (say, using solar cells). It weighs around 43mg, is monolithic, and can jump up by a millimeter while being driven by an external power supply. However, it uses electrostatic actuators that demand nearly 100V to operate. The lack of good voltage step-up  $\mu$ -circuits, along with the need to use complex control signals to control their multiple actuators in sync, has prevented its tetherless operation as of now.

Conventional motors used at larger macro-scale aerial vehicles suffer from scaling disadvantages in power efficiency and friction, which led to the use of simpler piezoelectric [24] and electrostatic [33, 45] actuators at the smaller scales. Though these score well on driving the wings/legs/springs with appropriate power using a transmission mechanism (that is, mechanical impedance matching), they fall short on the electrical side requiring inputs on the order of 200-5000V, with no lightweight electrical transformer known to efficiently accomplish this step up [28]. This has led to recent works on low-voltage electromagnetic (EM) actuators [48, 30, 46] particularly for flying  $\mu$ bots, but these devices consume unreasonable amounts of power in excess of 1W, most of which is lost to heat. The reason is that mechanical power increases linearly with current but heat loss increases quadratically, so simply increasing current by  $10\times$  to power the end effector will lead to impractical power consumption numbers. The severe mass budget demands low-voltage and power-efficient actuators that would use practical amounts of on-board power.

Locomotion energetics generally follows an inverse trend from above with flight, and especially hovering, being the most demanding [27], followed by jumping. It is then no surprise that only a few flying  $\mu$ bot designs are known to be capable of lifting their own weight [31, 45, 48] using external power tethers, and only two have been reported yet that can lift-off without tethers [26, 25] (see Table 1.1). Robofly [26] weighs 190mg and consumes 300mW, most of which is to power its 100mg power electronics circuit that drives its 200V piezoelectric actuator. The newer RoboBee X-wing [25] weighs 260mg and consumes 150mW

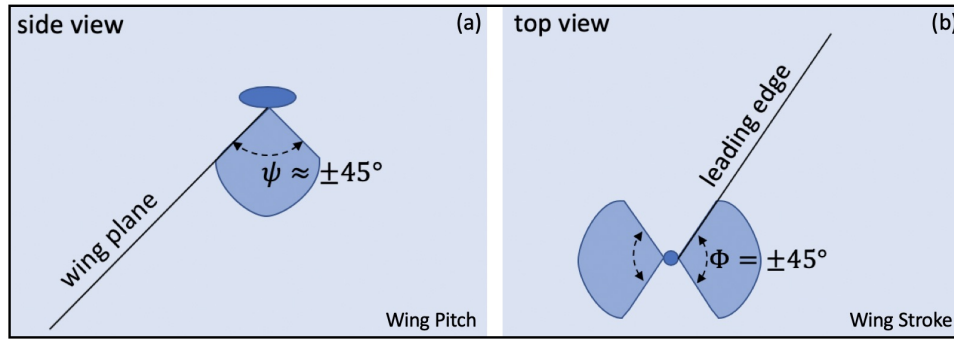


Figure 1.5: Biomimetic wing trajectory for use in flapping wing  $\mu$ bots.

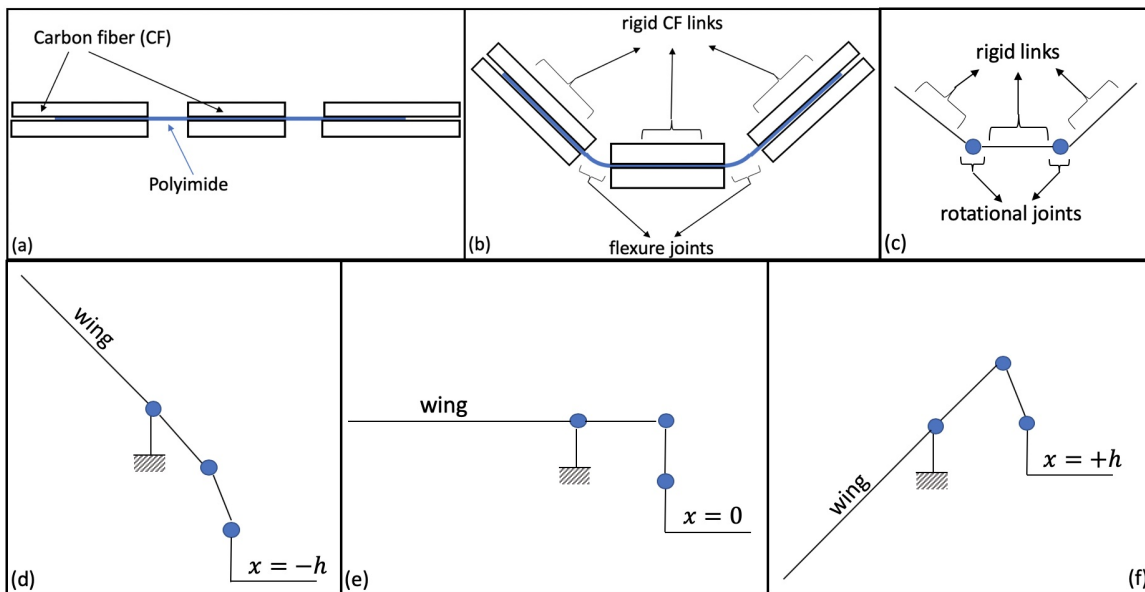


Figure 1.6: Composite 4-bar-type mechanical transmission used in prior flapping wing bots.

again mostly to power its 90mg power circuit instead of its 200V piezoelectric actuator. The problems, as can be seen, are that they consume a lot of power and need heavy power electronics. Practically we would need something consuming less than 40mW for them to be powered by future on-board batteries, plus the electronics shouldn't take up more than 10% of the total mass ( $\Rightarrow \approx 10\text{mg}$ ) to leave more space for useful payloads and probably more battery mass. Since flight is energetically demanding, one of the main challenges in making these tetherless would be to make very efficient actuators (rather than only relying on future high-energy + high-power-density batteries), orders of magnitude better than those used in the literature and than those in rolling, jumping and other ground-based  $\mu$ bots.

Most of the flying  $\mu$ bot research mimicks dipteran-like wing trajectories to generate lift (see Fig. 1.5), and the insects of interest have their wing motion around a nominal trajectory

Table 1.1: Summary of flying  $\mu$ bots.

	Mass (mg)	Lift (mg)	Power (mW)	Power Electronics	Electrical Actuator	Mechanical Transmission
Robofly [26]	190	190	300	100mg, 270mW	200V Piezo	Composite 4-bar
RoboBee X-wing [25]	260	260	150	90mg, 120mW	200V Piezo	Composite 4-bar
Zou et al EM flier [48]	80	80	1200	None.	5V EM	Composite 4-bar
Liu et al EM flier [30]	90	11	>1000	None.	5V EM	Composite 4-bar
This work (tethered) [6]	70	60	253	None.	5.5V EM	Compliant resonance
This work v2 [ongoing]	105	100 (estimate)	37	9mg, 8mW	9V EM	Compliant resonance
This work (fruit fly bot) [5]	0.7	0.3 (estimate)	3.3	None.	0.07V EM	Compliant resonance

characterized by 2 degrees of freedom, namely,  $\pm 45 - 75^\circ$  wing stroke and  $\pm 45 - 65^\circ$  wing pitch [18, 19, 17, 37, 15]. This trajectory is qualitatively different from the 0.1-1mm periodic linear motions produced by actuators at the mm-scale and therefore all designs use a separate transmission to transform this linear displacement to large wing strokes. Wing pitch is then achieved passively [42] in order to not add any extra actuators for simplicity. In order to amplify small motions to large rotations, contemporary research works [31, 48, 30] use the lever principle, like in 4-bar mechanisms, wherein laser cut carbon fiber (CF) and polyimide sheets are aligned and cured in a sandwiched fashion (see Fig. 1.6) with CF segments acting as the rigid links and the polyimide gaps acting as rotational joints, with required feature sizes going down to  $70\mu\text{m}$ . These complex multi-material-based transmission mechanisms require difficult 3D assembly, though there have been some recent trends on automating this assembly via pop-up MEMS type fabrication [43, 1]. Manual assembly, which is the approach taken in this dissertation, and mass production of MAVs at this size scale demand easy-to-construct high feature size mechanisms along with simple assembly.

The common challenges faced by the  $\mu$ bots can be summarized as shown in Fig. 1.7.

### 1.3 Solutions to Common Challenges

#### Rolling $\mu$ bots

Rolling and walking locomotions are more robust than bristlebots to changes in the environment's surface, but producing these motions requires generating a continuously rotating

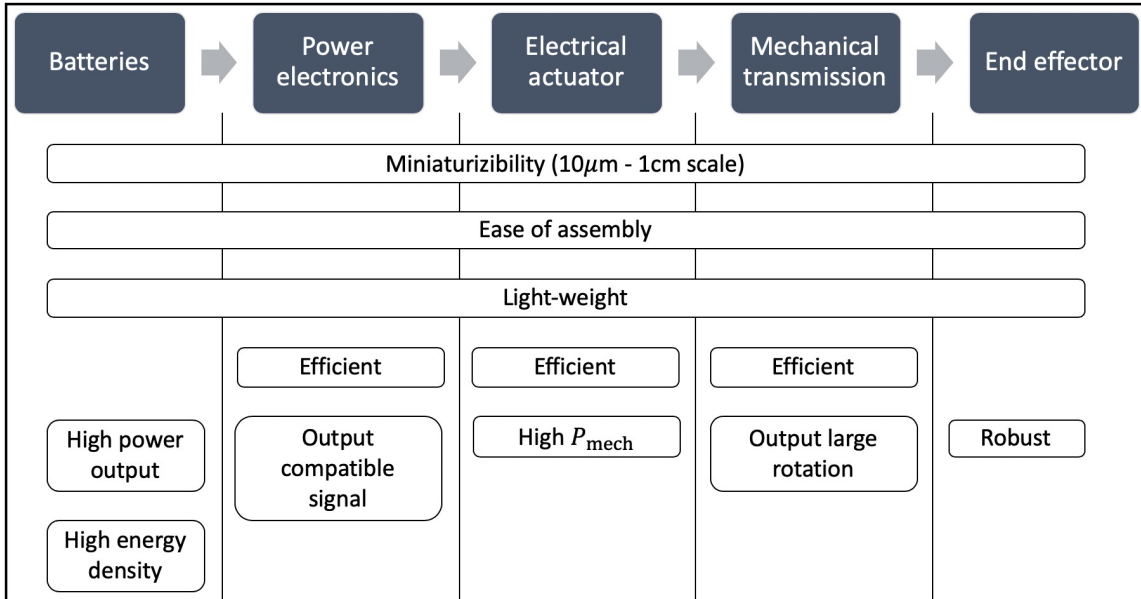


Figure 1.7: Challenges and performance metrics for the different building blocks of  $\mu$ bots.

motion in contrast to the small-displacement oscillatory actuators available at milligram scales. In this dissertation, we design a new mechanical transmission that converts small periodic motions to large continuous rotations by anisotropically adding up the small motions. The underlying principle is similar to some other designs like the inchworm motor [47, 33] which converts tiny motions of an actuator to large motions of a shuttle. Note that we still use anisotropy in the mechanism, but it has been shifted from the environment to inside the mechanism which we can fully control. The transmission constructed in this work turns only on clockwise inputs.

In order to simplify the drive electronics, we take a low-voltage actuation route by using electromagnetic (EM) actuation, that is, a magnet plus coil system. Low-voltage approach has previously been taken with flying  $\mu$ bots [48, 6, 5] but not with ground based ones. Here, the proposed transmission works with low-displacement actuators and thus keeps the magnet displacements low ensuring higher average magnetic fields seen by the coil, since the magnet pole face always stays within the coil. Use of the mechanical advantage principle inside the transmission keeps the actuation forces low ensuring low currents in the coil. Both these strategies further simplify the power electronics by lowering the current and power demands.

## Jumping $\mu$ bots

Again, EM actuation is used due to its low-voltage and ease of fabrication. We choose the coil impedance in order to power it directly using 1mg photovoltaic (PV) cells eliminating the need for any voltage conversion circuitry. In order to simplify fabrication and control/power

electronics, we make the design operate using a single actuator by making other functions occur passively. The single actuator uses the same mechanical transmission from the rolling  $\mu$ bot [4] to obtain continuous rotation motion. This rotation motion is then used to load a spring in an energy storage mechanism which can release the stored energy rapidly and passively after the energy reaches a given threshold, causing the  $\mu$ bot to jump.

## Flying $\mu$ bots

In order to make simple-to-assemble and easy-to-construct high feature size designs the strategy we adopt is the use of distributed compliant mechanisms [40, 39] to generate the desired motion as resonant shapes, and a few larger scale MAVs are known to exploit this idea [11, 22, 9, 8, 7, 2]. However, none of these compliant mechanism designs are easily manufacturable at desired small scales using standard fabrication procedures. Here we present a  $\mu$ bot design such that most of it is planar and laser-cut from a single material sheet, thus requiring very little assembly. All parts except the wing veins have feature sizes above  $250\mu\text{m}$  making it easy to manufacture.

Piezoelectric actuators themselves are very efficient in terms of electrical power consumed to mechanical power produced. One of the reasons then that piezoelectric powered devices are inefficient and heavy is because of the high drive voltages involved in the electronics that power them. Thus, we need to think about the co-design of electronics + actuation right from the start. We use EM actuators because they are logic level and there are many options to select logic level off-the-shelf electronic components. However if we are not careful while designing them they can still consume a lot of power like the EM flyers we mentioned before [48, 30, 46] – these actuators are low-voltage but they consume more than a watt to operate. One power reduction strategy we utilize is the use of multiple magnets in the design. This reduces the required coil current, and hence the resistive heat loss, to generate the same amount of mechanical power. Another strategy adopted is to decrease the amount of time the coil takes to pass the magnets. This may appear non-trivial at first glance but will become clear in the coming chapters.

## 1.4 Common Design Framework

Having fixed our choices for the robust end effector (namely, wheels, or, spring, or, wings), we restrict our choices for the remaining 4 blocks in the system as well (see Fig. 1.8). As is famously said, putting in the right constraints promotes innovation.

We have a rough idea on the specifications of commercial light-weight ( $\leq 20\text{mg}$ ) on-board power sources that will become available in the future. An estimated  $40\text{mg}$  battery providing  $\approx 20\text{mW}$  of power at  $3.5\text{V}$  is even possible today under lab settings [32, 10]. We start with off-the-shelf electronics that will be consistent with these, so as to not design our own custom chips and thus have a faster design iteration time. For now we test using laser-powered photovoltaic cells or supercapacitors but they are just place holders for the eventual

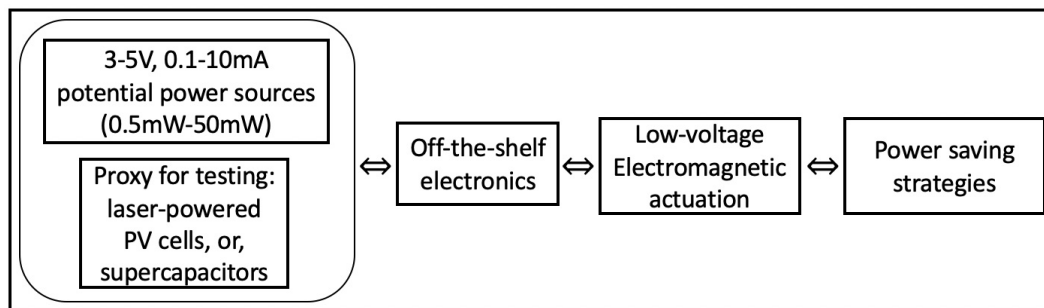


Figure 1.8: Common framework for all  $\mu$ bots in this work.

power source. We don't make custom electronics on Silicon, and off-the-shelf electronics can only be made efficient for low voltage operations, and thus we only use electromagnetic actuators in all of our  $\mu$ bots. Three of our  $\mu$ bots, in fact, use similar sized magnets and coils in their actuators. But using electromagnetic actuators isn't straightforward either because they can be low-voltage and still consume huge power. So to minimize resistive heat loss, which will still be the major source ( $> 50\%$ ) of power consumed in our devices, we use power saving strategies specific to the mechanical transmission.

## 1.5 This Work

Chapter 2 discusses the design of a self-sufficient rolling  $\mu$ bot that can be operated both using photovoltaic cells and supercapacitors. Chapter 3 discusses a globally untethered jumping  $\mu$ bot. Though not done in this work, but it can be made self-sufficient as well by simply using the same power electronics and supercapacitors that was used on the rolling  $\mu$ bot. Chapter 4 discusses a globally untethered flapping wing  $\mu$ bot with special emphasis on the making the actuator  $10\times$  more efficient, and the power electronics  $10\times$  lighter and  $100\times$  more efficient than all previously reported flapping wing  $\mu$ bots. Chapter 5 discusses the design of a fruit fly scale flapping wing robot which is able to mimic insect wing kinematics. Even though this isn't untethered, and any effort to make it so will require working with custom Silicon chip design folks, we talk about this work since this is the smallest flapping wing robot anyone has ever made and by 2 orders of magnitude. That is excluding nature of course.

# Chapter 2

## Rolling $\mu$ bot

Here we will see how a small-displacement actuator can be used to generate a continuous rotation motion to drive the wheels. We will also see how existing power sources and off-the-shelf electronics can drive this actuator correctly.

### 2.1 Micro-ratchet

The basic building block of the proposed mechanism is a ratchet with its cross-section portrayed in Figure 2.1. The inner shaft is free to rotate relative to the outer ring when it is rotated in a clockwise direction relative to the ring. Under this operating condition, the elastic protrusions emanating from the shaft slide over the zig-zag patterns on the inner perimeter of the ring. These elastic beams are bent by  $25\mu\text{m}$  more (in addition to any pre-deflection) when encountering the peaks in the pattern. When rotated anti-clockwise, the shaft locks relative to the ring. In this reverse operation, the elastic beams push the falling edge of the pattern head-on, and motion can only be achieved if the beams buckle. This buckling requires orders of magnitude higher torque compared to the simple sliding motion from before and this configuration can be considered as locked for the purposes of this paper.

Figure 2.2 shows the construction of the inner shaft. 12 tabs are laser-cut on a  $12.7\mu\text{m}$ -thick Kapton sheet. This laser-cut sheet is then rolled on to a 2mm-diameter Kapton tube and glued in place. The rest of the sheet adheres to the curved surface of the tube due to the glue, but the unglued tabs retain their planar shape thus acting as the desired elastic protrusions. The fabricated shaft can be seen in Figure 2.5. Rectangular slots cut into each of the 12 tabs will help in keeping the outer ring in place as will be seen next.

Rings with patterned holes are laser cut using  $25\mu\text{m}$ -thick stainless steel. These rings slide into the slots previously cut in each of the tabs as seen in Figure 2.3. The slots prohibit any sideways motion of the rings, but there is still a slight ‘give’ due to the clearances between the slot and ring, that is, due to the ring being thinner than the slot width. This play can cause the rings to not be perpendicular to the shaft. Thus, in each ratchet a set of 2 rings is used in conjunction to reduce the play and avoid any parasitic motion. The rings are joined

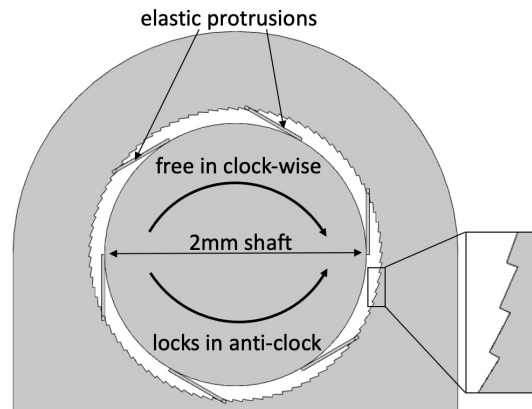


Figure 2.1: Cross-section of a micro-ratchet mechanism made using flexible beams on a shaft and a patterned hole. The peaks in the pattern are  $25\mu\text{m}$  high and are spaced  $4^\circ$ , or, approximately  $70\mu\text{m}$  apart.

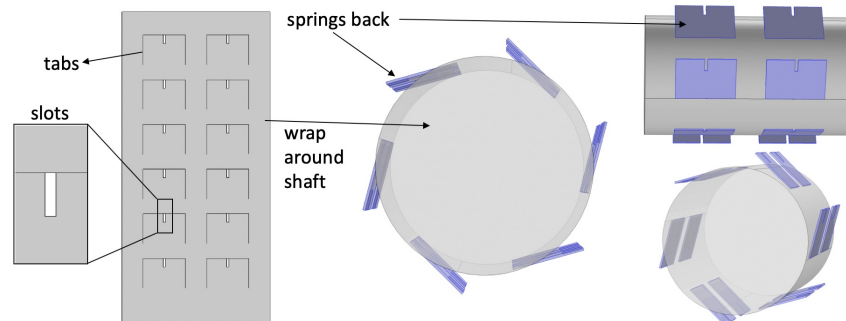


Figure 2.2: Fabrication of the shaft for the micro-ratchet mechanism.  $60^\circ$  spaced flexible beams are obtained by wrapping a laser cut Kapton sheet with tabs on to a Kapton tube.

using 3 carbon fibre (CF) rods placed  $120^\circ$  apart as seen in Figure 2.4(a).

## Backlash

Backlash is the maximum amount the shaft can rotate in the anti-clockwise direction before locking to the ring. From Figure 2.1 one can notice that the elastic beams would only need to slide a maximum amount equal to the peak separation in the patterned hole before hitting a falling edge. In reality, this number is even smaller. The elastic beams are not spaced apart at exactly  $60^\circ$  relative to each other due to assembly imperfections, and hence the contact points of the 6 beams are uniformly distributed over the peak separation. Thus, the backlash is estimated to be  $1/6^{\text{th}}$  of the peak separation, that is,  $4^\circ/6 \approx 0.67^\circ$ .

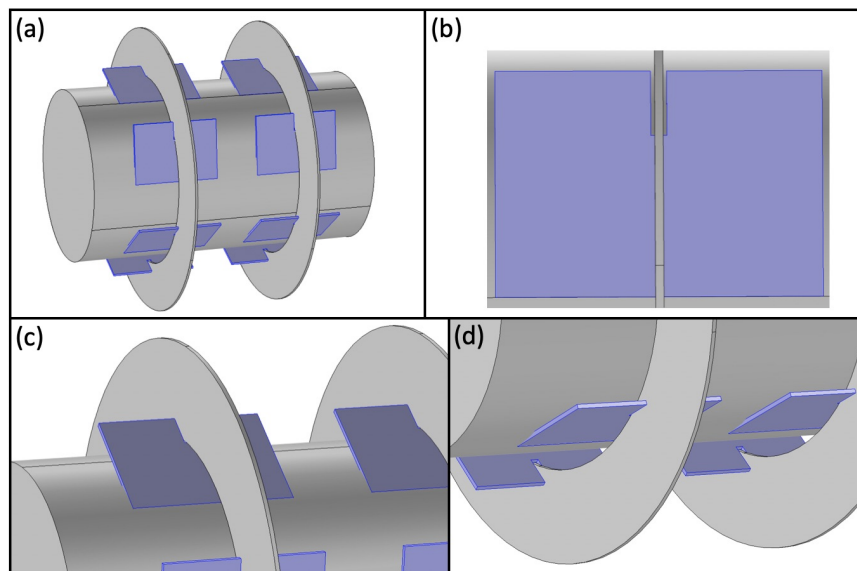


Figure 2.3: (a) Laser-cut patterned steel rings are slid in to the shaft such that (b) the ring passes through the slots in each of the tabs/elastic beams. (c) & (d) show a better view of the rings passing through the slots.

## 2.2 Double-ratchet

Now we seek a mechanism whose output rectifies and adds up the provided input motions. Two ratchets are connected together via a common shaft as shown in Figure 2.4. The front ratchet's rings are grounded. Input is provided at the back ratchet's rings, and the common shaft acts as the output. When the input is rotated clockwise, the back ratchet locks to the shaft but the front ratchet is free to rotate relative to the shaft. Thus, the shaft rotates clockwise. When the input is rotated anti-clockwise, the back ratchet is free to rotate relative to the shaft but the front ratchet locks to the shaft and prohibits it from rotating anti-clockwise. Thus, the shaft remains stationary. Providing periodic clockwise plus anti-clockwise motion at the input results in the shaft adding up all the clockwise motions and neglecting any anti-clockwise motions. The fabricated double-ratchet assembly can be seen in Figure 2.5.

### Experiment

We verify the functioning of the double-ratchet by providing it a periodic input manually as shown in Figure 2.6. The shaft is engaged to the back ratchet when the input is driven clockwise. This can be seen by noticing the motion of the black indicator attached to the shaft. The second row shows the shaft being grounded, with no motion of the indicator, when the input is driven anti-clockwise.

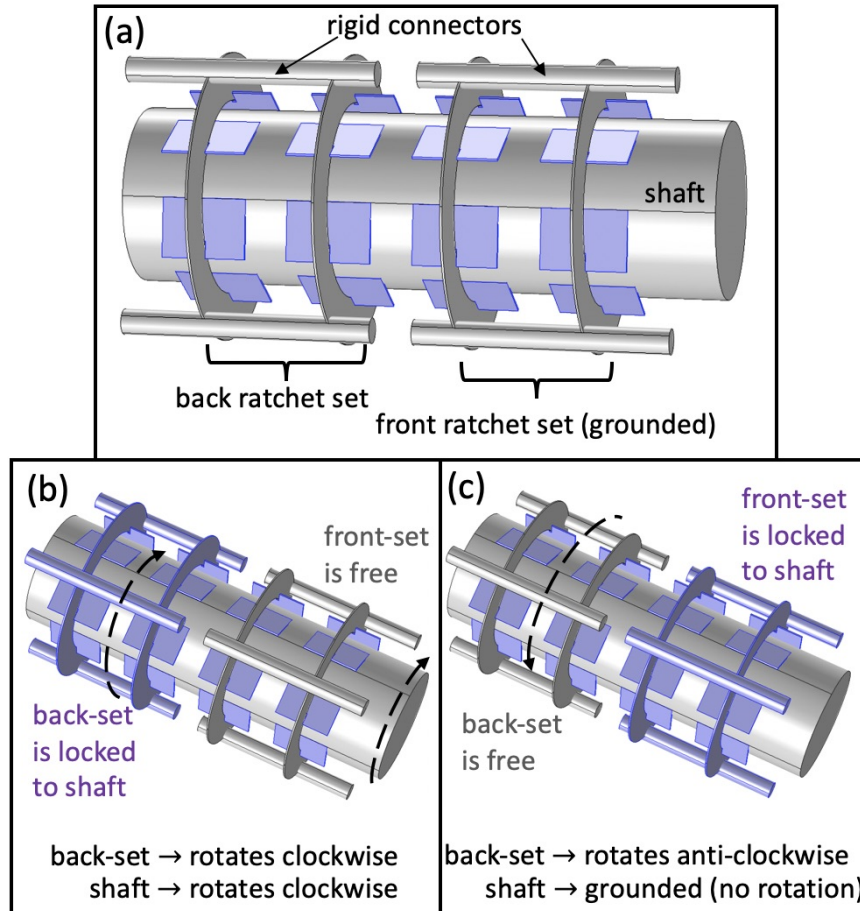


Figure 2.4: Operation principle of the double ratchet.

## 2.3 Electromagnetic Actuator

Here, instead of using a set of 2 rings for each of the front and back ratchets, we now use a single ring for both (see Figure 2.7). This is done to reduce the footprint of the device. We ensure the perpendicularity of the rings and the shaft, which is now lost due to the singular use of the rings, by adding new constraints. Perpendicularity of the grounded ring to the shaft is maintained by balancing the shaft using a third non-patterned ring. Perpendicularity of the input ring to the shaft is maintained by restricting the motion plane of the input.

The off-the-shelf electronics components used in this work don't function below 1V. We will later see that the coil burns around 1mW to generate the required driving torque  $\Rightarrow$  a coil current of around 1mA  $\Rightarrow$  we need a coil resistance of around 1000 $\Omega$ . Thus the coil is custom made from a very thin (in fact, thinnest available) 12 $\mu$ m-thick Copper wire which is array wound  $n_{\text{turns}} = 96 \times 16$  number of times. It has an inner diameter of 1.9mm, an outer diameter of 2.45mm, and a height of 1.6mm, with resistance  $\approx$  1500 $\Omega$ . The NdFeB magnet is

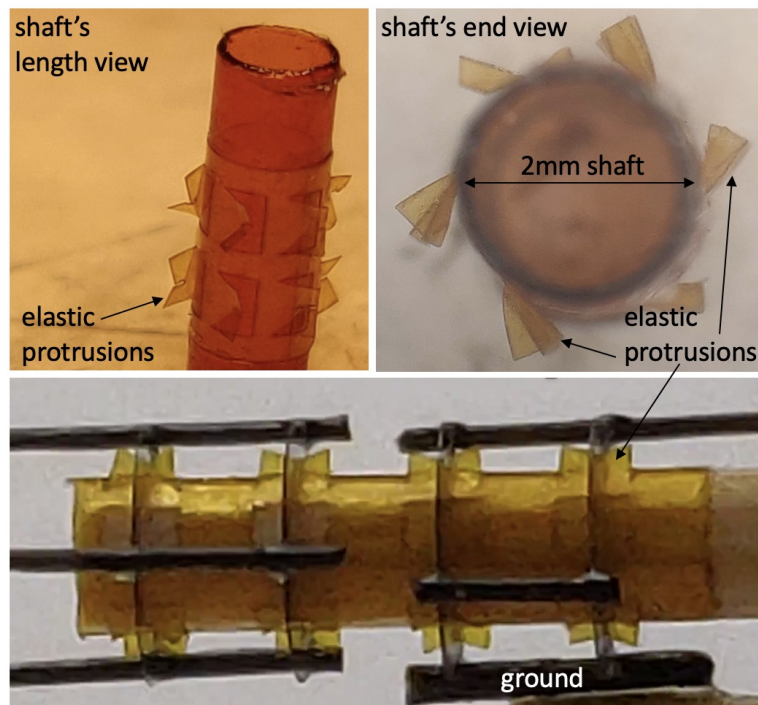


Figure 2.5: Fabricated double ratchet corresponding to Fig. 2.4. Seen in black are the 0.3mm CF rods that join the pairs of rings.

of grade N52 with 1.6mm diameter and height. The magnet is attached to the input arm of the double-ratchet mechanism. The grounded ring is attached to the rectangular base plate made from  $50\mu\text{m}$ -thick Aluminum sheet. The shaft is further supported by a non-patterned ring to ensure its perpendicularity. The input ring is attached via a long moment arm to the magnet which is concentric to the coil in its rest state. The fully deflected position of the magnet is chosen such that one of its pole faces is still almost inside the coil.

A  $50\mu\text{m}$ -thick Al alignment plate, shown in Figure 2.8, is used to ensure that the moment arm (and hence the input ring) always moves in a plane perpendicular to the shaft. This is accomplished by constraining the moment arm to only move through a narrow slot ( $100\mu\text{m}$ -wide) in the alignment plate. This slot also limits the magnet from moving completely out of the coil.

## 2.4 Starting Torque & Mechanical Losses

Three types of torques need to be overcome in each ratchet to produce motion. One is the friction torque arising from the contact between the elastic beams and the ring. Another is due to the energy dissipated in the deflected elastic beams when they are released after crossing over the peak (in the patterned hole) into the falling edge. And lastly to lift the

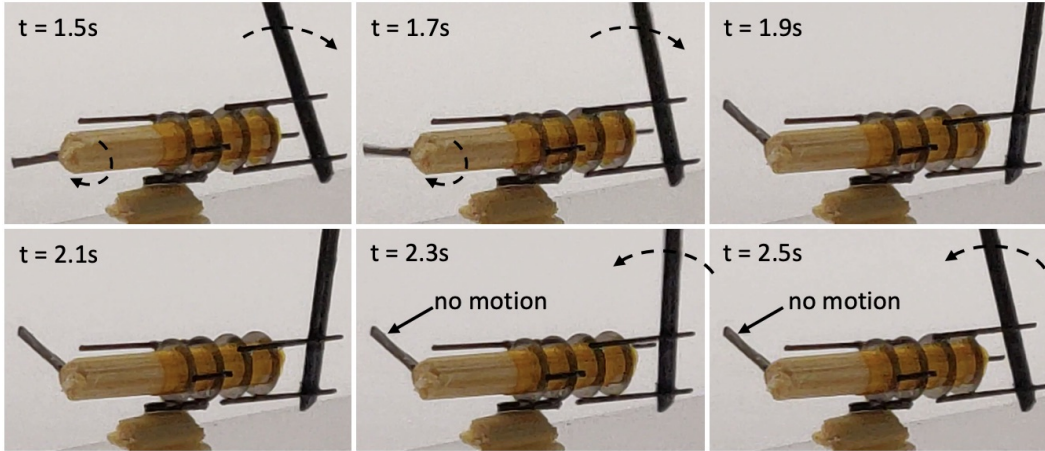


Figure 2.6: Double-ratchet mechanism operated manually, and thus time stamps are just indicative. Input is provided at the back ratchet, and output is observed using the black CF indicator rod attached perpendicularly to the shaft. Asymmetry in clockwise vs anti-clockwise operation can be observed.

weight of the magnet against gravity.

## Friction

Each of the elastic beams is  $l = 0.5\text{mm}$  long and  $w = 1\text{mm}$  wide, hence their bending stiffness is  $k = \frac{2.5\text{GPa}}{4} \frac{t^3 w}{l^3} \approx 10\text{N/m}$ . When inside the patterned hole, they are pre-deflected (pre-tensioned) by an amount no larger than  $\Delta y = 0.2\text{mm}$  (estimate), corresponding to a contact force of  $F_{\text{contact}} = 2\text{mN}$  per beam. Assuming a friction coefficient of  $\mu_s = 0.1$ , this corresponds to a starting torque of  $6 \cdot \mu_s \cdot F_{\text{contact}} \cdot r_{\text{shaft}} = 1.2\mu\text{Nm}$  per ratchet.

## Elastic dissipation

At any given time only one of the 6 beams is released from the peak into the valley due to the beams not being perfectly  $60^\circ$  apart from each other. Thus in a rotation of  $4^\circ \approx 0.07\text{rad}$ , an energy of  $\frac{1}{2}k\Delta y^2 - \frac{1}{2}k(\Delta y - 25\mu\text{m})^2 = 0.05\mu\text{J}$  is dissipated. By energy equivalence, this corresponds to a starting torque of  $\frac{0.05\mu\text{J}}{0.07\text{rad}} = 0.7\mu\text{Nm}$ .

## Potential energy

The  $25\text{mg}$  magnet at the end of the  $8\text{mm}$  long moment arm, which always remains almost horizontal, exerts a torque of  $0.25\text{mN} \cdot 8\text{mm} = 2\mu\text{Nm}$ .

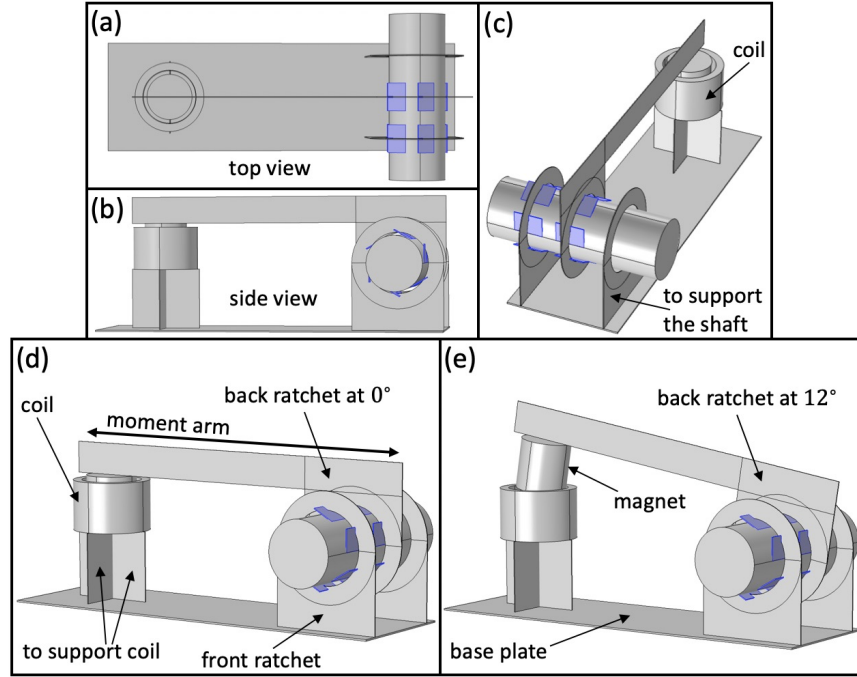


Figure 2.7: An electromagnetic actuator (magnet + coil) driving the input ratchet via a long moment arm. Rings and coil supports are attached to a common base plate that acts as a mechanical ground.

## Starting current

The total estimated starting torque is the sum of the above three and thus =  $3.9\mu\text{Nm}$ . Experimentally it is found that an applied torque of  $4.4\mu\text{Nm}$  is sufficient to produce motion. This minimum starting torque needed determines the minimum coil current needed to produce motion.

Using finite element simulations we find the average magnetic field seen by the coil to be  $B_{\text{avg}} \approx 0.1\text{T}$ . This average is not low because the magnet undergoes only small displacements never being very distant from the coil. The 8mm long moment arm greatly reduces the force the coil needs to generate to produce  $4.4\mu\text{Nm}$  of torque.  $F_{\text{coil}}(\text{needed}) = 4.4\mu\text{Nm}/8\text{mm} = 0.55\text{mN} = n_{\text{turns}} \cdot B_{\text{avg}} \cdot I_{\text{coil}} \cdot 2\pi r_{\text{coil}} \Rightarrow I_{\text{coil}} = 0.5\text{mA}$ . The heat loss in the coil at this current value will be  $I_{\text{coil}}^2 R_{\text{coil}} = 0.38\text{mW}$ , and the voltage across the coil will be  $V_{\text{coil}} = 0.75\text{V}$ . However, the off-the-shelf electronics components used in this paper can't operate below 1V and thus the voltage across the coil would be  $V_{\text{coil}}(\text{actual}) = 1\text{V} \Rightarrow I_{\text{coil}}(\text{actual}) \approx 0.6\text{mA}$  which is more than the current required to guarantee function.

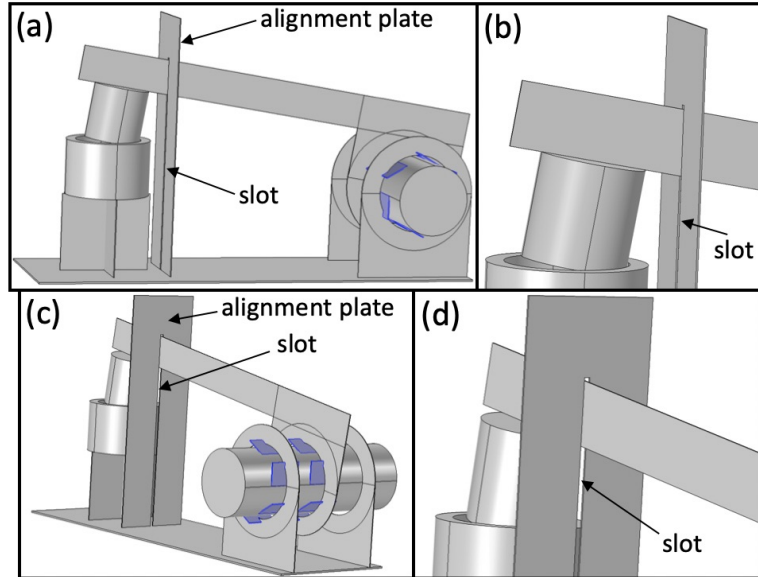


Figure 2.8: A long narrow slot in the alignment plate keeps the moment arm in a single plane. This slot also restricts the moment arm from rotating more than  $\approx 12^\circ$ .

## 2.5 Power Electronics

Figure 2.9 shows the schematic of the 3 constituent components of the driving electronics. An 11mF supercapacitor from Seiko (CPH3225A) is used as a power source for this device. It has an internal resistance of  $160\Omega$  and can be charged up to 3.3V. A resistive divider with  $R_s = 5.6\text{k}\Omega$  is used to provide a virtual ground. An opamp based oscillator circuit is used to generate a 20Hz oscillating waveform. Time period of oscillations is given by  $T = 2RC \ln\left(\frac{1+\beta}{1-\beta}\right)$ , where  $\beta = \frac{R_2}{R_1+R_2}$ . Choosing  $R_1 = R_2 = 56\text{k}\Omega$  sets  $\beta = 0.5$  and  $T \approx 2RC$ . Choosing  $R = 10\text{k}\Omega$  and  $C = 2.2\mu\text{F}$  sets  $f = \frac{1}{T}$  near 20Hz.

This periodic waveform is then fed to an H-bridge made out of 2 opamps which alternates the connection polarity of the coil to the supercapacitor at 20Hz. The supercapacitor discharges through the coil and the opamps stop functioning below a supply voltage of 1V at which point the coil stops receiving alternating supply voltage and the device stops functioning.

A  $12.7\mu\text{m}$ -thick Kapton sheet with an  $18\mu\text{m}$ -thick double-sided adhesive film attached to it acts as the substrate of the circuit. The copper traces acting as wiring are laser cut from a  $25\mu\text{m}$  thick Copper sheet and then bonded to the substrate using heat and pressure, as seen in Figure 2.10. The surface mount opamps, 0402 resistors, 0603 capacitor and 0402 zero resistance jumpers are glued to the substrate and then soldered to the Copper wiring using solder paste and a hot air gun. Jumpers are used to make electrical connection paths that otherwise intersect with existing copper traces. The double opamp (TLV342 RUG) and the single opamp (TLV341 DRL) units each weight around 2mg and are the heaviest parts

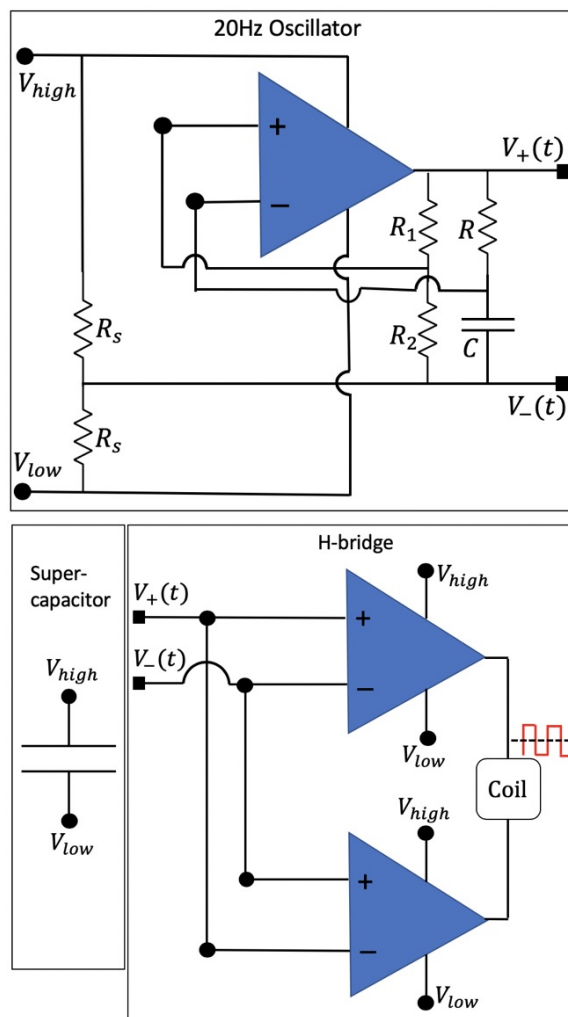


Figure 2.9: Conceptual circuit diagram. Supercapacitor acts as the supply for the coil, oscillator and the H-bridge. The standard opamp based oscillator circuit functions by charging and discharging the capacitor  $C$ , whose time constant is tuned using  $R$ .

in the circuit.

## 2.6 Assembly

The completed electronics unit is glued on to the Al base plate in the space below the moment arm as seen in Figure 2.11. Spiked wheels 8mm in diameter, laser cut from  $50\mu\text{m}$ -thick Al, are attached to the double-ratchet's shaft. Smaller 3mm diameter wheels, with CF rod as axle and free to rotate inside a Kapton tube, are added to the front to balance the robot. This makes this robot a rear-wheel-drive. The fully assembled bot can be seen in Fig. 2.12.

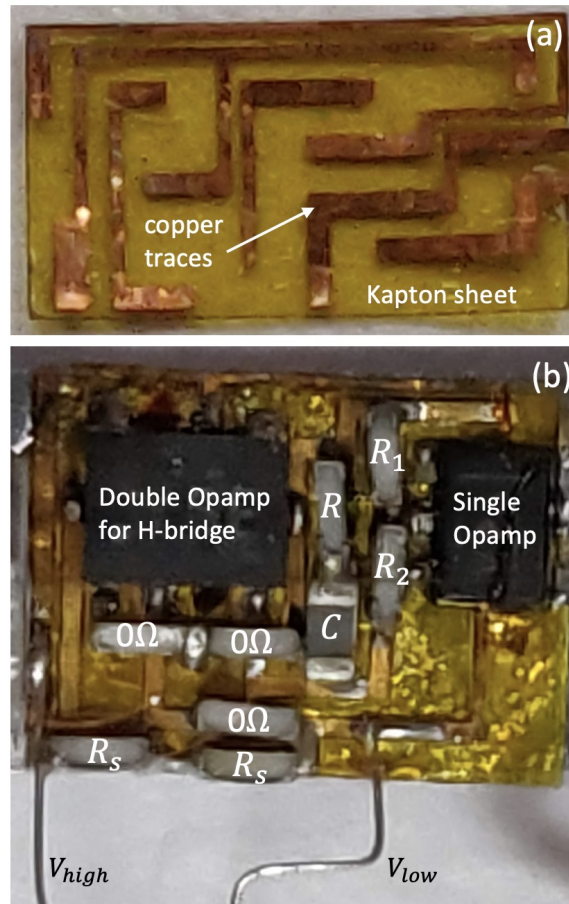


Figure 2.10: Actual circuit. (a) To avoid any manual alignment copper traces are laser-cut in place, and then the Kapton + adhesive laminate is hot pressed on to it. (b) The surface mount electrical components are glued and soldered in place manually.

It measures  $18\text{mm} \times 8\text{mm} \times 8\text{mm}$ . The masses of all the constituents after the assembly can be seen in Table 2.1.

## 2.7 Rolling Using Photovoltaics

Before trying the supercapacitor powered version of the bot we tried an alternate power source which is a  $1\text{mm} \times 1\text{mm}$  infrared PV cell (MH GoPower 5S0101.4-W) that produces current when a  $976\text{nm}$  wavelength laser light (MH GoPower LSM-010) is shone on it. The laser intensity is increased until the PV cell outputs  $\approx 1.5\text{V}$  while driving a  $1.5\text{k}\Omega$  load. The robot's operation was intermittent since the onboard PV cell moves out of the laser spot (seen as the green spot on the infrared indicator card in Figure 2.13) as soon as the robot rolls forward, and then needs to be repositioned which is done manually. So to test the operation

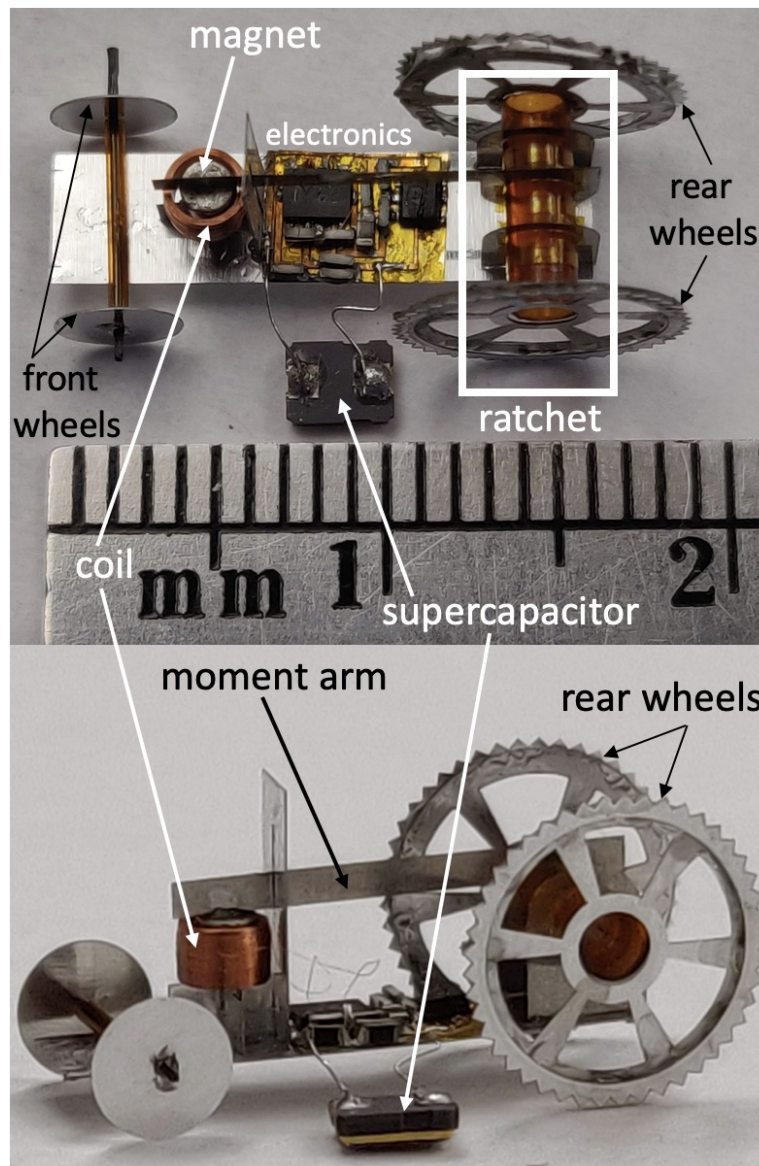


Figure 2.11: Fully assembled device. The supercapacitor is kept close to the ground so that it can be charged using probes from a function generator and then released quickly.

we allow the smoothed out rear wheels of the robot to slip in a gap/valley between two cards so that its wheels rotate but the robot doesn't move forward and its PV cell remains in the laser spot. Because of the absence of the spikes on the rear wheels and the heavy supercapacitor, this version of the robot weights 96mg. Note that even while in motion if the laser is somehow shone continuously on the PV cell then a continuous forward motion would be expected.

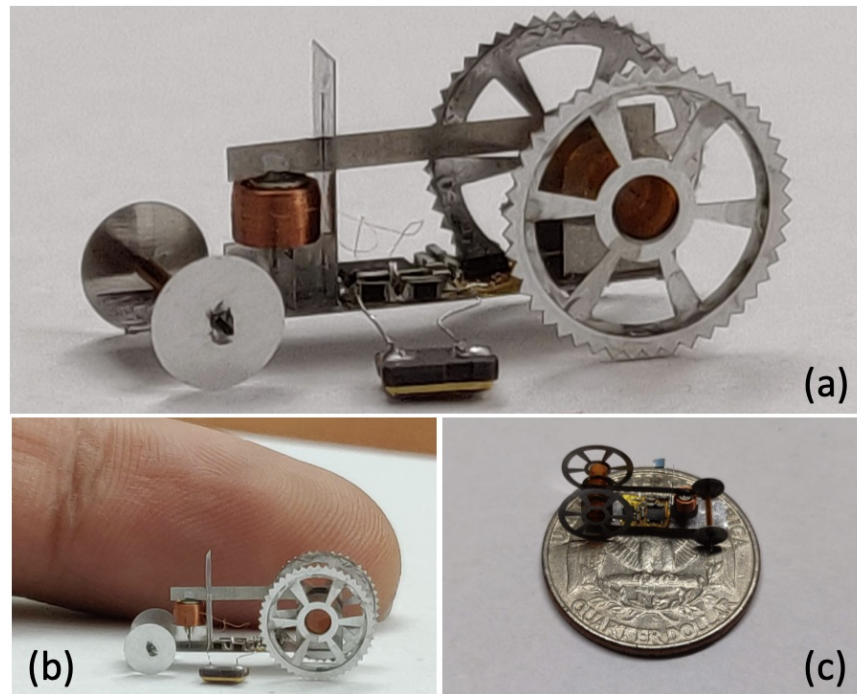


Figure 2.12: (a) Supercapacitor powered rolling microbot. Compared to (b) an index finger, and, (c) a quarter dollar.

## 2.8 Rolling Using Supercapacitor

The supercapacitor is charged up to 3V (in 1 minute) using an external function generator. After this charge, the voltage across the supercapacitor drops from 3V to 1V in 8s due to it getting discharged via the coil. During this phase, the magnet drives the input of the ratchet at 20Hz resulting in the rear wheels rotating at  $300^\circ/\text{s}$  and the robot rolling forwards at 27mm/s as seen in Figure 2.14. If we had a constant 1V battery, then the robot can be kept operating while consuming 0.6mW of power. But since we don't have a constant voltage battery, the average power consumed in the 8s is greater at 2.5mW since the capacitor starts with a higher voltage.

## 2.9 Summary

In this chapter we designed an insect-sized rolling  $\mu$ bot driven by continuously rotating wheels. It measured 18mm  $\times$  8mm  $\times$  8mm. There were 2 versions of the robot - a 96mg laser-powered one and a 130mg supercapacitor powered one. The robot was able to move at 27mm/s (1.5 body lengths per second) with wheels rotating at  $300^\circ/\text{s}$ , while consuming an average power of 2.5mW. Neither version had any electrical wires coming out of it, with the supercapacitor powered robot also being self-sufficient and was able to roll freely for 8

Table 2.1: Mass distribution of the rolling  $\mu$ bot.

Sub-component	Mass
Electrical parts	
Power electronics	17mg
Coil	13mg
Magnet + moment arm	27.3mg
Supercapacitor	24.1mg
Structural parts	
Base plate + Perpendicular supports	16.2mg
Front wheel assembly	4.8mg
Rear wheels	18.7mg
Ratchet tube	8.6mg
<b>Total</b>	<b>130mg</b>

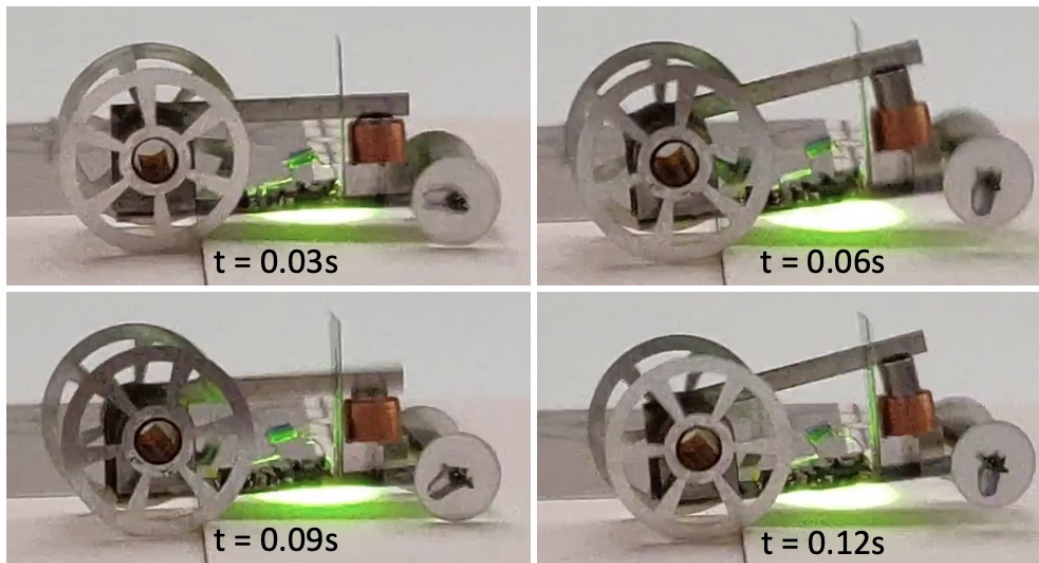


Figure 2.13: Stationary laser-powered bot with continuously rotating but slipping wheels. The wheels are made to slip by smoothing it out (eliminating the spikes) and then placing them at a bump that they cannot climb due to low traction.

seconds after a single charge. Low-voltage electromagnetic actuators (1V-3V) along with a novel double-ratcheting mechanism enabled the operation of this device. It is the lightest and fastest self-sufficient rolling  $\mu$ bot reported yet, to the best of our knowledge.

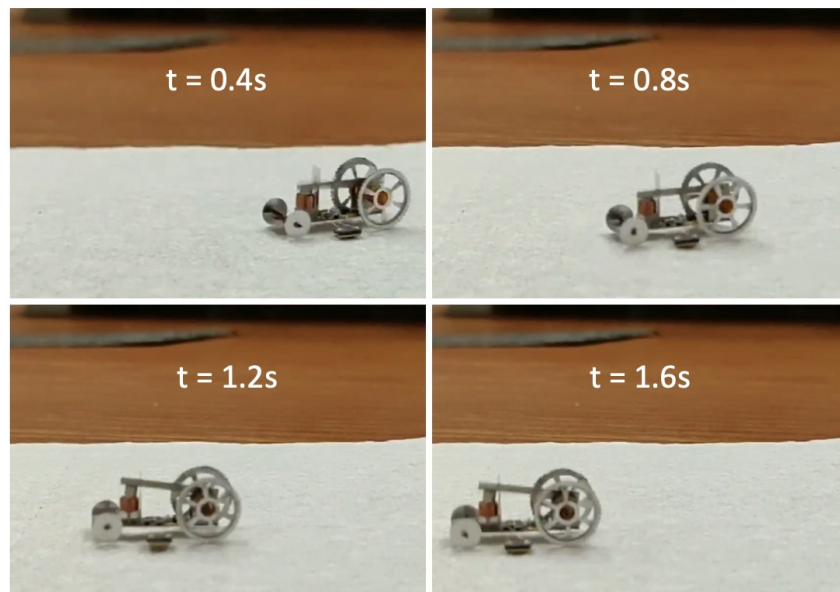


Figure 2.14: Microrobot rolling forwards in real time. The bot is operated over a piece of paper for better traction and to avoid any slipping between the spiked wheels and the level surface.

## Chapter 3

### Jumping $\mu$ bot

The same ratcheting and actuation mechanism from before is reused here to generate a continuous rotation motion. We could have used the same power electronics too but we decide on doing something much simpler to power the coil. Here we will see how a continuous rotation motion can be used to repeatedly load a spring and then passively release it to perform jumps.

#### 3.1 Underlying Principle

The principle behind is a spring that stores potential energy by getting pulled by the onboard motors (see Fig. 3.1). Rapidly releasing the spring releases the stored energy which then causes the  $\mu$ bot to jump up to a certain height. Neglecting air resistance and using energy conservation we have  $\frac{1}{2}k\Delta l^2 = mgh$ , where  $m$  is the net mass of the  $\mu$ bot,  $\Delta l$  is the maximum spring deflection, and  $h$  is the jump height measured from the maximum deflected state. As a reference, a 1cm jump of a 100mg  $\mu$ bot should require  $\approx 10\mu\text{J}$  of spring energy.

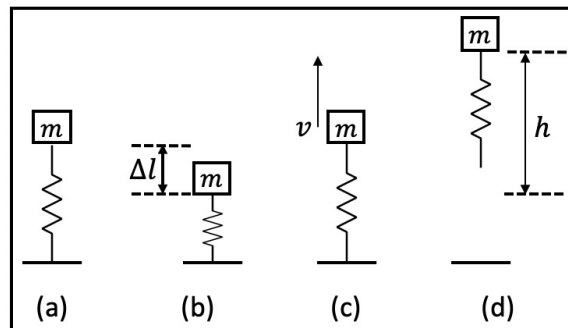


Figure 3.1: Underlying principle of the jumping bot. (a) Neutral state of the spring. (b) Spring deflected by the maximum amount storing potential energy. (c) Released spring just before losing ground contact. (d) Bot at the maximum jump height.

## 3.2 Spring Design

The planar spring design shown in Fig. 4.8(a) is laser cut from a  $25.4\mu\text{m}$ -thick Stainless Steel sheet. The individual beam length  $l$  and width  $w$  are tuned using finite element analysis (FEA) to achieve a desired stiffness  $k$  while allowing for the maximum out-of-plane deflection  $\Delta l$  (that is, keeping maximum strains below the Yield strain). A T-shaped stand is glued perpendicularly to the spring plane, and then two feet are glued on to the stand (see Fig. 4.8(b)). Both the stand and the feet are laser cut from a  $50\mu\text{m}$ -thick Aluminum sheet. The spring can be seen in its fully deflected state in Fig. 3.3 which is computed via FEA simulations.

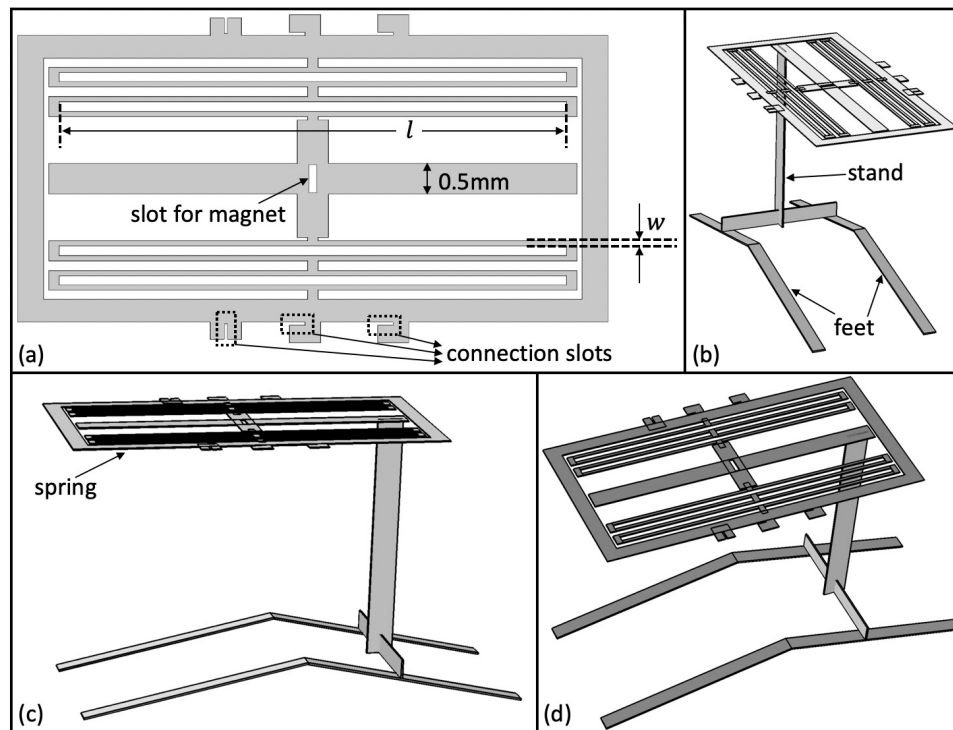


Figure 3.2: (a) Planar spring design showing connection slots later used to attach parts perpendicularly to the spring. (b), (c) & (d) Different views of the stand and feet glued to the spring.

## 3.3 Spring Loading Mechanism

The spring is pulled up, or loaded, via a  $12.7\mu\text{m}$ -thick 0.5mm-wide Kapton string attached to the center of the spring. This pull is obtained by winding the string around a clockwise rotating cylindrical shaft as seen in Fig. 3.4.

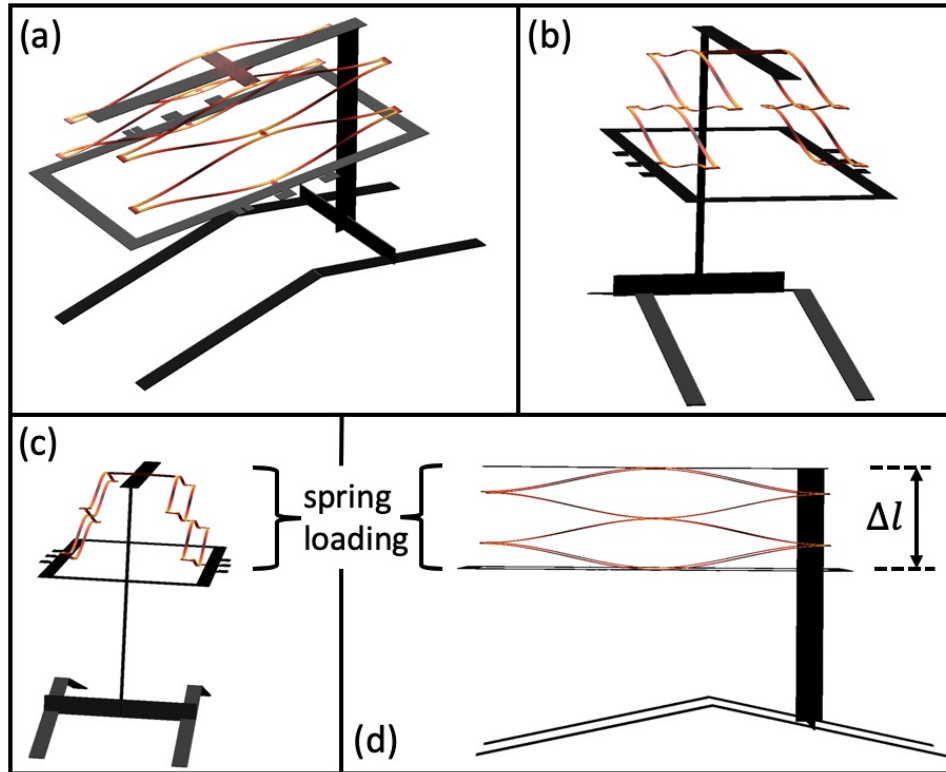


Figure 3.3: Different views of the spring at full deflection (FEA).

### 3.4 Spring Release Mechanism

We want this jumping  $\mu$ bot to operate using a single motor. That motor will be used to rotate the shaft, so the desired spring release mechanism should not be controlled by a separate motor but instead happen passively. We use magnets to create an automatic release mechanism (see Fig. 3.5(a)). Two anti-parallel magnets placed side by side are attracted by a certain amount of force  $F$ . If opposing forces acting on the magnet exceed even a little beyond this attractive force, this leads to an instability and the magnets are released rapidly. The magnets used are Neodymium grade N52 of diameter = 0.3mm and height = 0.5mm, and their release force is measured at  $F_{\text{release}} = 7.5\text{mN}$  (see Fig. 3.5(b)).

Again, the spring is loaded by winding the string but this time the string connects to the spring via these magnets. One magnet is glued to the center of the spring in the slot shown in Fig. 4.8(a), and another is glued to the end of the string. The opposing forces on the magnets increase with increasing spring deflection and at the correct threshold the magnets snap (see Fig. 3.6). The release force informs the spring stiffness and deflection choice so that it is storing around  $10\mu\text{J}$  at the time of release. Choosing  $k = 2.5\text{N/m} \Rightarrow \Delta l = \frac{7.5\text{mN}}{2.5\text{N/m}} = 3\text{mm}$  at the time of release  $\Rightarrow$  a stored energy of  $\frac{1}{2} \cdot 2.5\text{N/m} \cdot (3\text{mm})^2 = 11.25\mu\text{J}$  at the time of release.

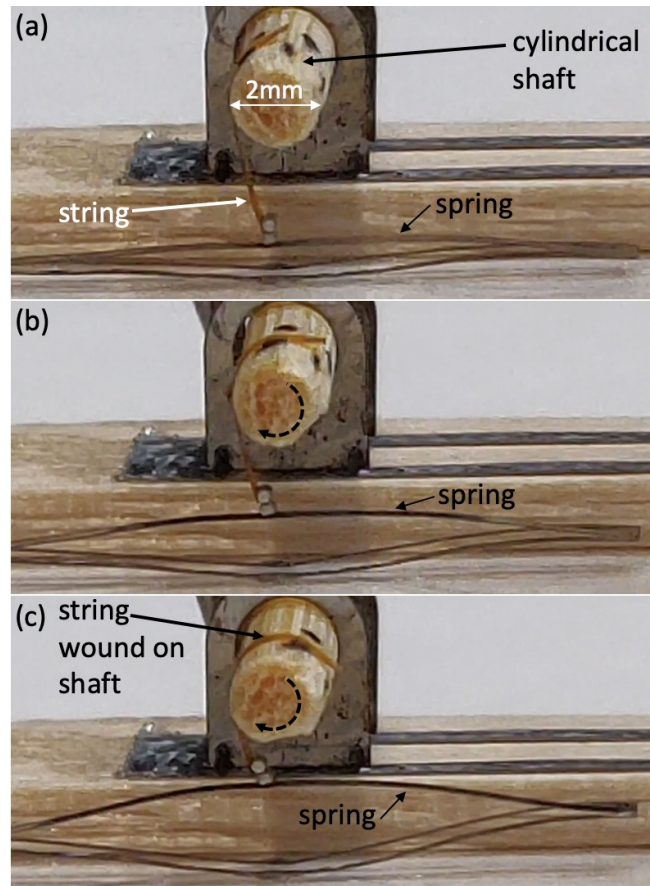


Figure 3.4: Spring loading mechanism tested on a simple leaf spring.

### 3.5 Shaft Rotation Mechanism

In order to wind the Kapton string to generate the pull, the shaft should be made to rotate in a clockwise direction. We do so using the same ratcheting technique described in the previous chapter.

#### Double-ratchet

All planar parts in Fig. 3.7 are laser cut from a  $50\mu\text{m}$ -thick Aluminum sheet. Four rings are used in this mechanism, with rings 1 & 4 supporting the shaft, and rings 2 & 3 acting as ratchets. Rings 1, 2 & 3 are rigidly connected to each other using two rectangular beams, called ring connectors. The two ring connectors can be seen rotated  $90^\circ$  relative to one another. Two T-shaped connectors connect rings 1 & 4 to the U-shaped base-plate. Two rectangular beams, called coil supports, are glued perpendicularly to the base-plate and then a coil is glued above them. A rectangular magnet limiter, with a narrow  $100\mu\text{m}$  slot in it, is

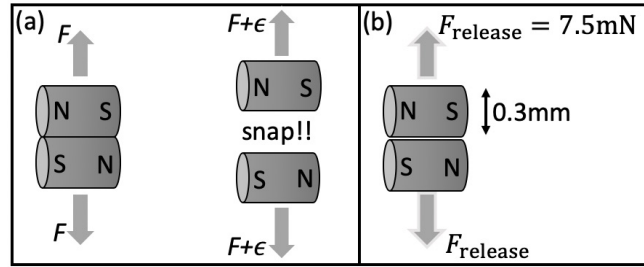


Figure 3.5: Passive spring release concept using magnets.

also glued perpendicularly to the base-plate and touching the coil. The magnet is concentric to the coil in its neutral position and is glued to a rectangular magnet guide (see Fig. 3.7 & Fig. 3.8(c)). A long moment arm emanating from ring 3 connects to the magnet guide via a small orthogonal rectangular beam (see Fig. 3.8(c)).

Input motion is provided at the moment arm using the magnet-coil actuator, and the shaft acts as the output. When the input is rotated clockwise, ring 3 locks to the shaft and the shaft is free to rotate clockwise relative to ring 2. Thus, the shaft rotates clockwise. When the input is rotated anti-clockwise, ring 3 is free to rotate relative to the shaft but ring 2 locks to the shaft and prohibits it from rotating anti-clockwise. Thus, the shaft remains stationary. Providing periodic clockwise plus anti-clockwise motion at the input (for example, in Fig. 3.8(a), (b)) results in the shaft adding up all the clockwise motions and neglecting any anti-clockwise motions thus resulting in a continuous clockwise rotation motion as desired.

The magnet guide passes through the narrow slot in the magnet limiter (see Fig. 3.8(c), (d)). This serves two purposes. It ensures that the moment arm and the magnet always move in a plane perpendicular to the shaft and the base-plate. The slot also prohibits the bottom pole face of the magnet from coming out of the coil as seen in Fig. 3.8(d).

## Electromagnetic Actuator

The coil is custom made from a  $25\mu\text{m}$ -thin Copper wire which is array wound  $n_{\text{turns}} = 48 \times 8$  number of times. It has an inner diameter of  $1.9\text{mm}$ , an outer diameter of  $2.45\text{mm}$ , and a height of  $1.6\text{mm}$ , with resistance  $\approx 100\Omega$ . A thicker Copper wire is used compared to the rolling  $\mu$ bot to reduce the risk of breaking the wire during the assembly process. The NdFeB magnet used is the same as before (grade N52, with  $1.6\text{mm}$  diameter and height).

## 3.6 Assembly

The double-ratchet mechanism is glued perpendicularly to the spring designed before (see Fig. 3.9). The fully assembled bot weights  $75\text{mg}$  and measures  $17\text{mm} \times 6\text{mm} \times 14\text{mm}$  (see Fig. 3.10) with mass distribution outlined in Table 3.1. Note that the stand and legs are

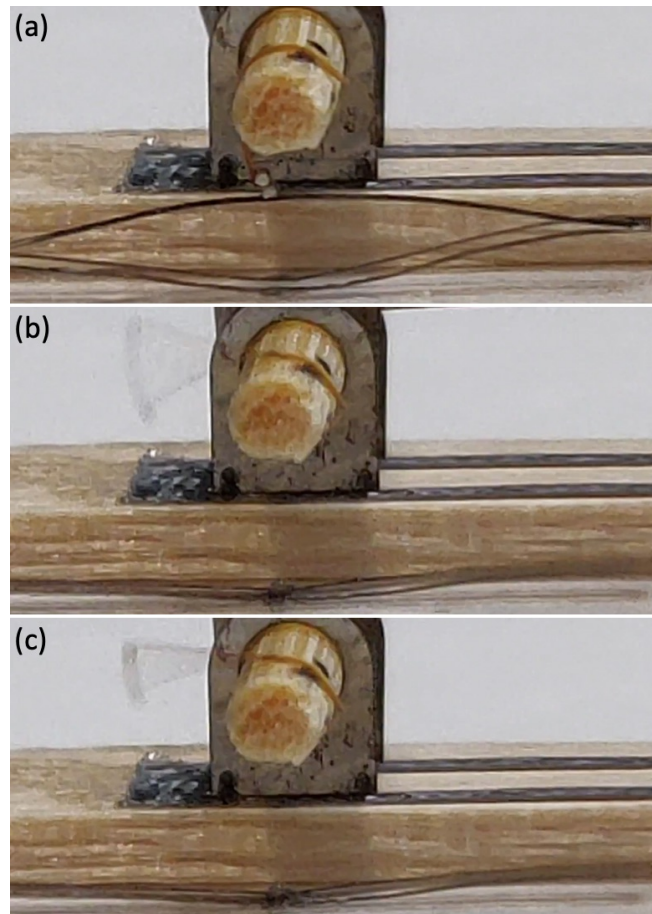


Figure 3.6: Passive spring release in action. (a) Spring at maximum deflection just before the magnets snap. (b) String vibrating just after the release. (c) String vibrations dampening over time.

big but the rest of the bot is just a centimeter long. Fig. 3.11 shows the 2 extreme positions the magnet moves about. This corresponds to the ratchet rotating by increments of  $\approx 2^\circ$  in each cycle. The string is attached and wound on the center of the shaft as shown in Fig. 3.12.

### 3.7 Starting Torque

Two types of torques need to be overcome to produce motion. One is the friction torque arising from the contact between the shaft and the ring. Another is to counteract the spring force.

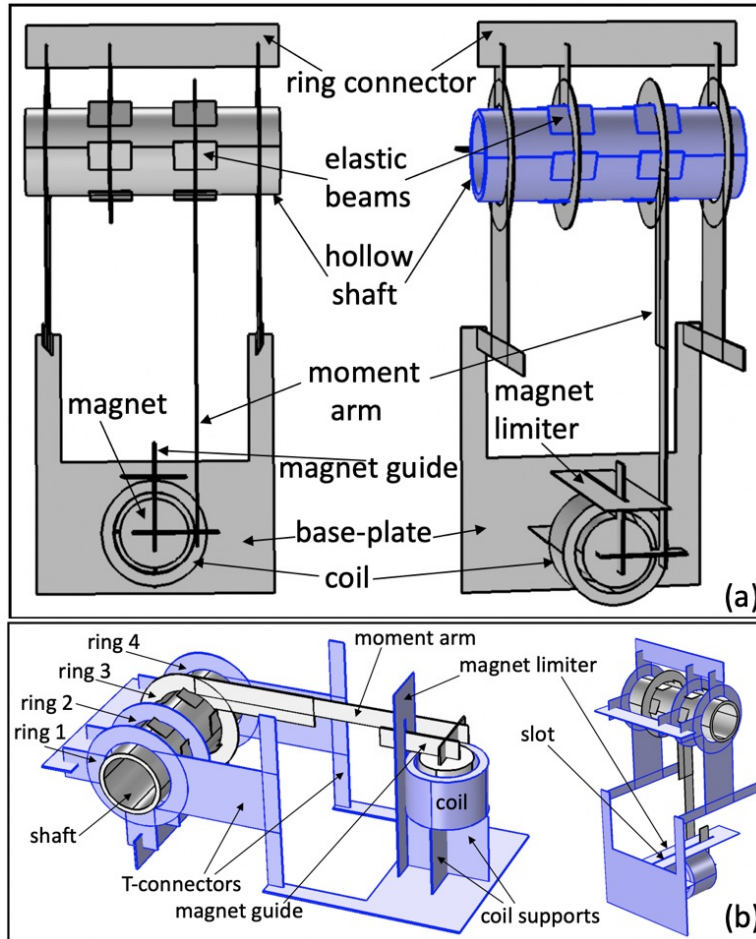


Figure 3.7: The double ratchet mechanism used to produce continuous rotation motion. (a) Shaft colored in blue. (b) All parts acting as one rigid part colored in blue.

### To overcome friction

The spring pulls on the shaft which then pushes against rings 1 & 4 (see Fig. 3.7). The maximum combined contact force occurs when the spring is fully deflected and thus equals  $F_{\text{release}} \Rightarrow F_{\text{contact}} = 7.5\text{mN}$ . Assuming a friction coefficient of  $\mu_s = 1$ , this corresponds to a starting torque of  $\mu_s \cdot F_{\text{contact}} \cdot r_{\text{shaft}} = 7.5\mu\text{Nm}$ . A large friction coefficient is assumed since the hollow shaft is flexible and will deform under the load thus increasing its contact area with the inner perimeter of the rings.

### To counteract spring force

Work needs to be done in order to deflect the spring and store potential energy into it. At the maximum spring deflection a string tension force of  $F_{\text{release}}$  acts at a distance of  $r_{\text{shaft}}$

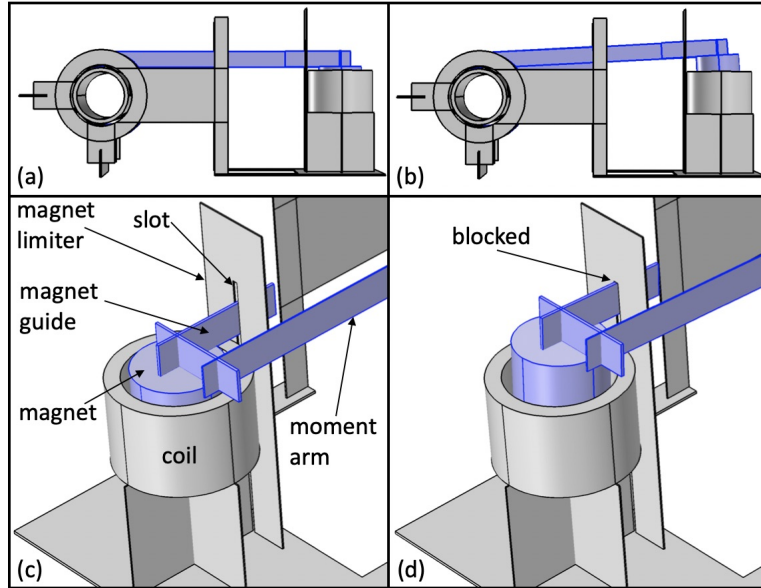


Figure 3.8: (a) & (b) Two extreme positions of the moment arm separated by  $\approx 2^\circ$  rotation. (c) & (d) Magnet limiter in action.

Table 3.1: Mass distribution of the jumping  $\mu$ bot.

Sub-component	Mass
Electrical parts	
Coil	13mg
Magnet + moment arm	27mg
PV cells	$2 \times 1\text{mg}$
Structural parts	
Base-plate + supports	9mg
Ratchet tube	9mg
Steel spring	2mg
Rings + connectors	11mg
Stand + feet	2mg
<b>Total</b>	<b>75mg</b>

from the center of the shaft  $\Rightarrow$  a starting torque of  $F_{\text{release}} \cdot r_{\text{shaft}} = 7.5\mu\text{Nm}$ .

### Starting current

The total estimated starting torque is the sum of the above two and thus  $= 15\mu\text{Nm}$ . Experimentally it is found that an applied torque of  $17\mu\text{Nm}$  is sufficient to produce motion,

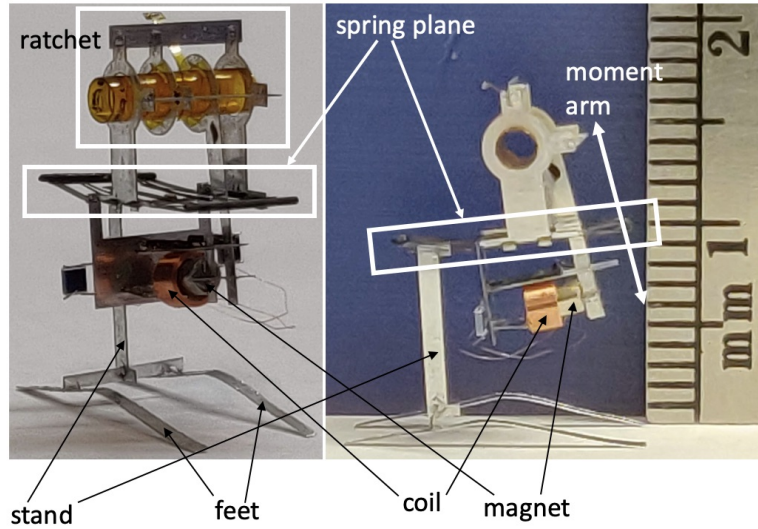


Figure 3.9: Fully assembled bot compared with a millimeter ruler.

which will now determine the minimum coil current needed to produce motion. Using FEA simulations we find the average magnetic field seen by the coil to be  $B_{\text{avg}} \approx 0.1\text{T}$ . The 8mm long moment arm greatly reduces the force the coil needs to generate to produce  $17\mu\text{Nm}$  of torque.  $F_{\text{coil}}(\text{needed}) = 17\mu\text{Nm}/8\text{mm} \approx 2.1\text{mN} = n_{\text{turns}} \cdot B_{\text{avg}} \cdot I_{\text{coil}} \cdot 2\pi r_{\text{coil}} \Rightarrow I_{\text{coil}} \approx 8\text{mA}$ . Heat loss in the coil at this current value will be  $I_{\text{coil}}^2 R_{\text{coil}} = 6.4\text{mW}$ , and the voltage across the coil will be  $V_{\text{coil}} = 0.8\text{V}$ .

### 3.8 Jumping Using External Power

The coil is powered using an external function generator and a simple square-wave voltage waveform. We noted that when using  $V_{\text{coil}} = \pm 0.7\text{V}$  the spring could be deflected almost completely but this voltage wasn't enough to release the magnets. A voltage of  $V_{\text{coil}} = \pm 0.8\text{V}$  was needed to passively release the magnets and cause the bot to jump. For a 75mg bot, a stored spring energy of  $11.25\mu\text{J}$  should cause the bot to jump up by 15mm. In practice, however, this jump height is close to 8mm (see Fig. 3.13(c)) possibly due to wind resistance, inefficient spring to kinetic energy conversion [12], and other device non-idealities.

The jumping rate or the number of jumps the bot can do in a minute is determined by how fast we can load the spring. Here we operated the actuator at 20Hz which then cause the bot to jump once every 10seconds while consuming 6.4mW of power. This power is mostly the Joule heat loss in the coil, as the mechanical power required to overcome friction and load the spring is in  $\mu\text{Watts}$ . Thus in theory the jumping rate could be increased by an order of magnitude while still consuming the same amount of power. The bot can do multiple successive jumps at this rate of 6 jumps/min without tipping over. We think the elasticity of the 2 external wires powering the coil provides this stability which prevents the

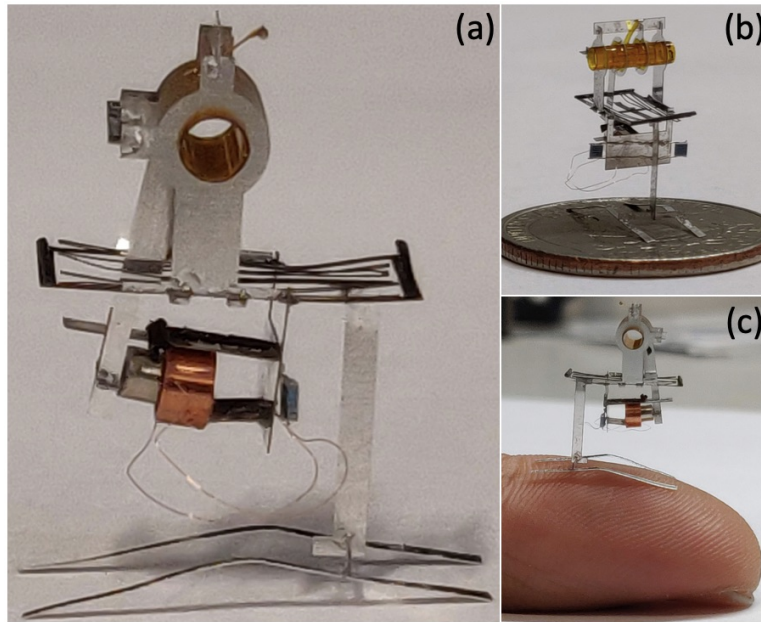


Figure 3.10: (a) Jumping  $\mu$ bot, with (b) a quarter dollar, and, (c) an index finger.

bot from falling over.

### 3.9 Jumping Using Photovoltaics

Here the power source we use is a  $1\text{mm} \times 1\text{mm}$  infrared PV cell (MH GoPower 5S0101.4-W) that produces current when a  $976\text{nm}$  wavelength laser light (MH GoPower LSM-010) is shone on it. The laser intensity is increased till the PV cell outputs  $\approx 0.8\text{V}$  while driving a  $100\Omega$  load.

We connect 2 PV cells to the coil in opposite polarity as shown in Fig. 4.28. Shining the laser on one PV cell makes the current go one way (see Fig. 4.28(b)), while shining on the other makes it go the other way (see Fig. 4.28(c)). This alternate shining of the laser is done manually to drive the actuator which then loads the spring. The laser used is an infrared laser which is invisible to the naked eye. The white card seen in Fig. 3.15 is an indicator card that emits green light when struck by the IR laser so that we know where the laser is pointing.

The bot jumps the same amount as before since the extra mass of the 2 PV cells is  $< 3\text{mg}$  and thus negligible compared to the bot's mass. After launching up from the ground, the bot develops an anti-clockwise angular spin (see Fig. 3.15). This results in the bot tipping over in this direction after landing on the tip of its feet. This falling over could be avoided, say, by further lowering the center-of-mass of the bot and supporting the spring more symmetrically using two stands (at the front and back) instead of one to enable a more

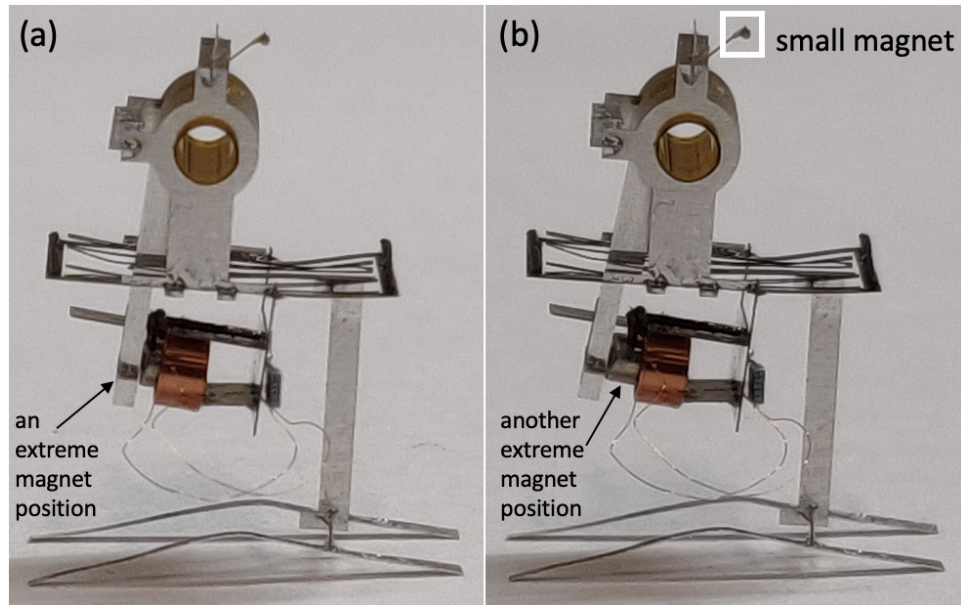


Figure 3.11: The 2 extreme ratchet positions, separated by  $\approx 2^\circ$ . Also seen is the small magnet from the release mechanism.

spin-less take-off.

### 3.10 Summary

In this chapter we designed an insect-sized jumping  $\mu$ bot weighing 75 milligrams and measuring  $17\text{mm} \times 6\text{mm} \times 14\text{mm}$ . The  $\mu$ bot consumed 6.4 mW of power to jump up by 8 mm in height. The tethered version of the robot could jump up 6 times per minute each time landing perfectly on its feet. The untethered version of the robot was powered using onboard photovoltaic cells illuminated by an external infrared laser source. It is the lightest untethered jumping microrobot with onboard power source that has been reported yet.

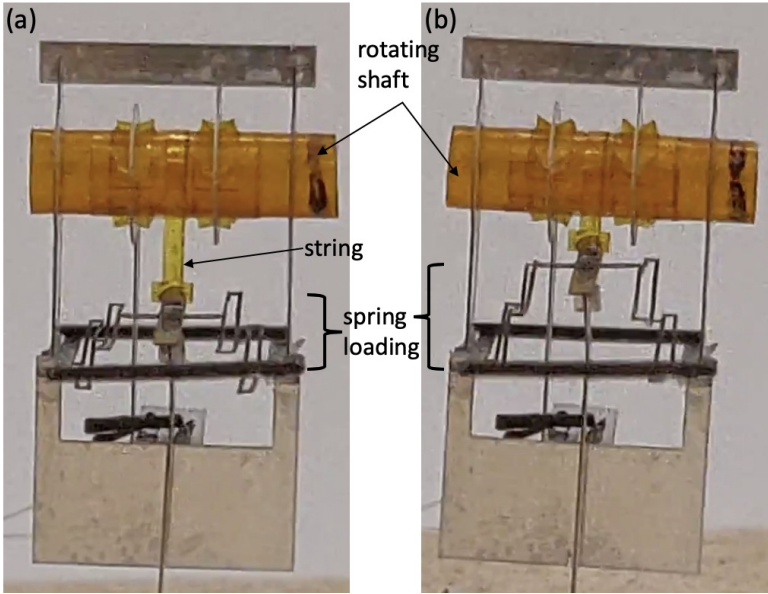


Figure 3.12: Spring loading in conjunction with the double-ratchet.

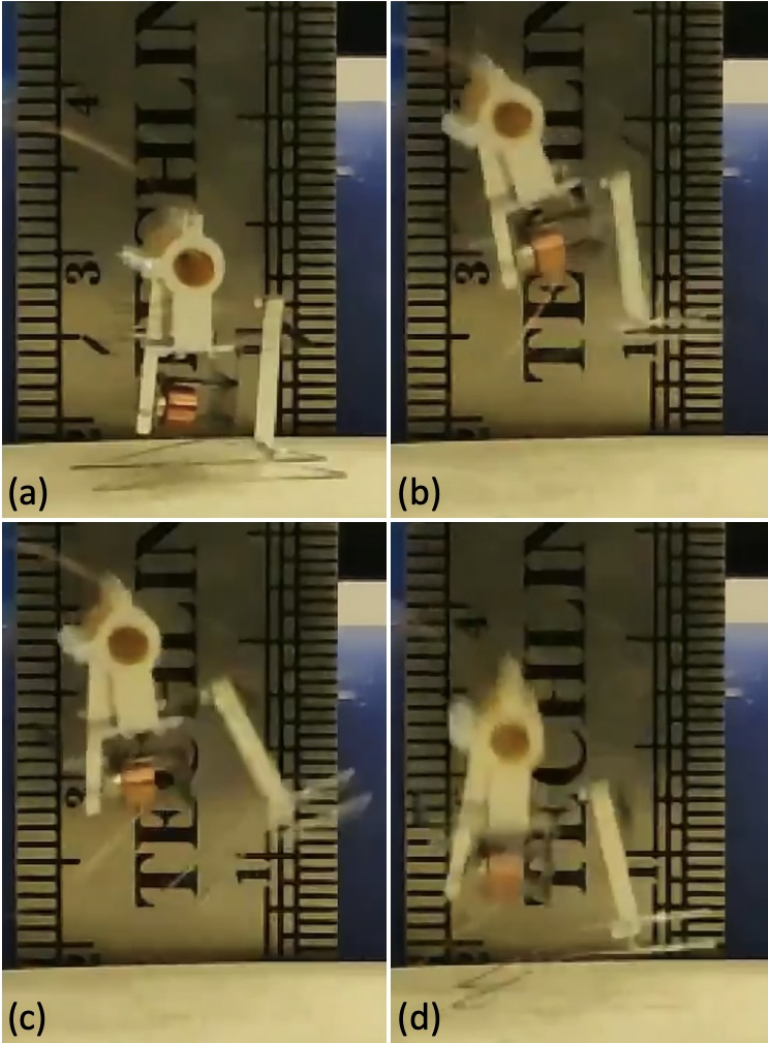


Figure 3.13: Tethered jump of the bot using external power supply.

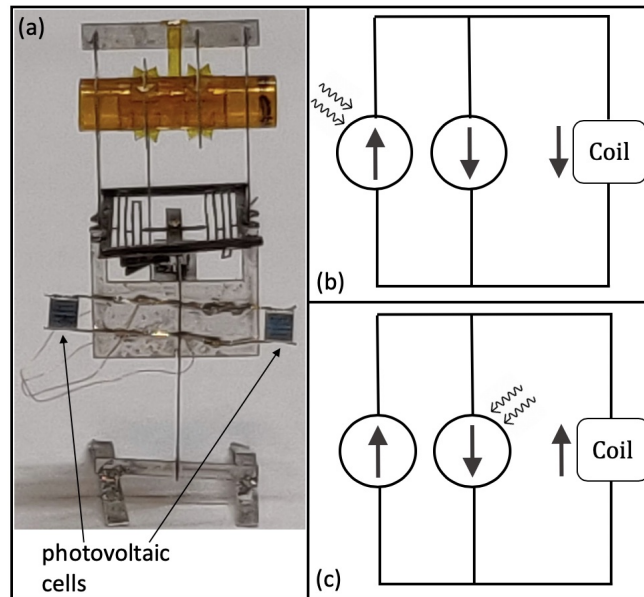


Figure 3.14: Circuit with 2 PV cells for tetherless  $\mu$ bot operation.

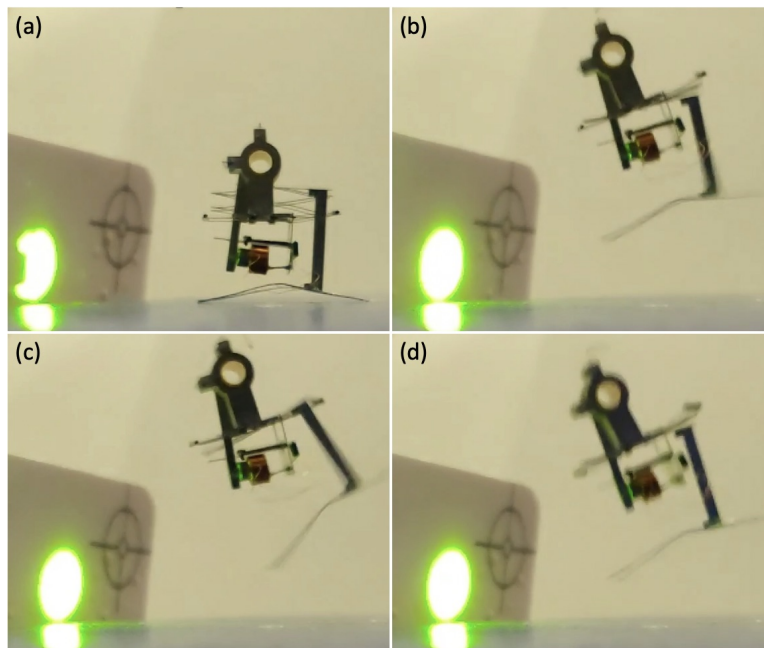


Figure 3.15: Tetherless jump of the  $\mu$ bot using laser power.

# Chapter 4

## Flapping Wing $\mu$ bot

In the previous chapters, the rolling and jumping  $\mu$ bots produced and required mechanical power in the tens of  $\mu$ Watts. Flight energetics being a completely different beast demands mechanical power in the mWatts [20, 27]. Recall that mechanical power increases linearly with current but heat loss increases quadratically. So even if our jumping bot was only burning up 6mW, simply increasing current by  $10\times$  to power flight will lead to impractical power consumption numbers. In short, we need a radical re-design of our actuator.

### 4.1 Design Choices

**Goal:** The goal is to mass-produce  $\approx 100$ mg self-sufficient flying  $\mu$ bots using existing technologies. This goal is inspired from the fact that  $\mu$ bots need to be cheaply produced in large numbers to accomplish some of the applications previously mentioned.

#### Existing technologies

**Current miniature batteries:** An estimated 40mg battery providing  $\approx 20$ mW of power at 3.5V is possible today under lab settings [32, 10]. We design around this specification since we don't fabricate batteries in this work and are thus restricted by what is available.

**Current power electronics:** Existing power electronics used to drive the actuator are (a) an order of magnitude heavier than the actuator, and, (b) use an order of magnitude more power than the actuator [26, 25]. This is mainly due to the high voltages required to drive piezoelectric actuators. Fulfilling this power demand (120-270mW) would require impractical amounts of battery weight. Thus, lighter and more efficient power electronics are required. We use  $\approx 5$ V low-voltage EM actuators since they are cheap and require no specialized high-voltage power electronics.

**Required actuator efficiency:** To generate 100mg lift, 5mW of mechanical power is expected to be adequate [20, 27]. Thus, in order to use the above battery, a desired actuator + electronics efficiency of  $\geq 25\%$  is needed.

## Mass production

**Use of planar compliant mechanisms:** Note that the composite fabrication method used in prior works (and outlined in the introduction) is planar, but it needs subsequent 3D assembly mostly done manually which delays the whole process. Rob Wood’s group has recently demonstrated an automated procedure for doing the 3D assembly [43, 1] but it requires 6-7 layers of multi-material composites undergoing many processing steps which only their lab does as of now. Thus, this process is not as well suited to mass production as a single material substrate undergoing a single laser cutting or etching process that is widely available to everyone. Therefore on the manufacturing side we resort to planar, mostly single material, fabrication processes. One of the implications of choosing single-material planar mechanisms is the need to rely on the structure’s distributed compliance to produce motion.

In the previous  $\mu$ bots in this dissertation, the actuation frequency was low ( $\leq 20$ Hz) and mechanism friction was not an issue. However, flight demands we operate at higher frequencies [20, 27] and if we try to scale the previous designs to operate at  $> 100$ Hz friction could potentially become an issue. The use of single-material non-contact-based compliant mechanisms also helps by eliminating friction by design.

## Weight budget

We target for 40mg of battery mass, 40mg of actuator mass, 10mg of mechanical transmission mass, and 10mg of sensor & control/power electronics. We will update this target distribution if it later appears to be infeasible. In order to reduce weight and simplify fabrication, we use a single actuator in our design as is done in many of the prior works. This means we actuate only one degree of freedom, which is the wing stroke, and rely on achieving wing pitch passively. This is done by constructing a flexure joint near the wing’s leading edge which then causes the wing to pitch on the action of aerodynamic forces. To ensure the correct phase lag of  $90^\circ$  between the wing stroke and wing pitch (to always generate positive lift), the wing + flexure-hinge system should be made to operate quasi-statically [42]. This requirement of passive wing pitch, however, imposes limitations on the operating frequency. Peak aerodynamic torque seen by the wing =  $\tau_{\max} = (1.2\text{mN per wing}) \cdot (\text{with centre-of-pressure } 2\text{mm below the flexure hinge}) \approx 2.4\mu\text{Nm}$ . This determine its flexure hinge’s stiffness  $k_{\text{wrot}}$ , that is,  $k_{\text{wrot}} = \frac{\tau_{\max}}{45^\circ} \approx 3\mu\text{Nm}$ . State-of-the-art wings have a rotational inertia  $I_{\text{wrot}} \geq 1.2\text{mg}\cdot\text{mm}^2$  [42], and these are already the lightest wings that can be made since they are made using sparing amounts of CF veins plus  $1.5\mu\text{m}$ -thick polyester membrane. Both the above facts imply a maximum resonant frequency for the wing + flexure-hinge system, that is,  $f_{\text{res}} = \frac{1}{2\pi} \cdot \sqrt{\frac{k_{\text{wrot}}}{I_{\text{wrot}}}} \leq 250\text{Hz}$ . Thus, unless we operate at half this resonant frequency, that is,  $f \leq \frac{f_{\text{res}}}{2} = 125\text{Hz}$ , inertial effects will dominate preventing the desired quasi-static operation of the wing pitch.

## 4.2 Electromagnetic Actuator

Just like in the previous chapters, the Lorentz force experienced by a current carrying conductor in a magnetic field is used here to generate mechanical power from electrical power input. The magnetic field is generated using the same off-the-shelf Neodymium grade N52 magnet with a height and diameter of 1.6mm. We give the coil a radial clearance of  $400\mu\text{m}$  ( $\Rightarrow$  coil inner radius =  $0.8\text{mm} + 0.4\text{mm} = 1.2\text{mm}$ ) to avoid any collisions with the magnet during motion, and we make the coil no thicker than  $250\mu\text{m}$  due to the rapid magnetic field strength drop along the radial direction. Copper is chosen as the coil material due to its low resistivity. With these requirements we select the coil height to be 1.6mm so that the coil weighs =  $15\text{mg} \Rightarrow [m_{\text{magnet}} = 23\text{mg}] + m_{\text{coil}} = 38\text{mg}$ , and thus the actuator weighs no more than  $40\text{mg}$ , as was its mass budget. The coil is custom made from  $25\mu\text{m}$ -thick Copper wire using  $n_{\text{turns}} = 8 \times 48$  number of turns, since at the time of fabrication this wire thickness was the thinnest wire available for custom manufacturing from our vendor. The force experienced by the coil (or equivalently, the magnet) is given by (see Fig. 4.1)

$$F_{\text{Lorentz}}(t) = B_{\text{radial}}(x(t))I_{\text{coil}}(t)l_{\text{coil}} \quad (4.1)$$

where  $B_{\text{radial}}(x)$  is the effective radial field seen by the coil at a separation of  $x$  from the center of the magnet, and is calculated using the finite element method on the coil+magnet system. The instantaneous mechanical power produced by the system is

$$P_{\text{mech}}(t) = F_{\text{Lorentz}}(t)v(t) \quad (4.2)$$

where  $v(t) = \dot{x}(t) = h\omega \cos(\omega t)$  is the velocity of the moving coil (or of the moving magnet in case of a stationary coil). Reformulating the above equation in terms of current we get

$$P_{\text{mech}}(t) = B_{\text{radial}}(x(t))I_{\text{coil}}(t)l_{\text{coil}}v(t) = V_{\text{emf}}(t)I_{\text{coil}}(t) \quad (4.3)$$

where

$$V_{\text{emf}}(t) \triangleq B_{\text{radial}}(x(t))l_{\text{coil}}v(t) \quad (4.4)$$

is the back-emf generated in the coil from the relative motion. For a system periodically driven as  $x(t) = h \cdot \sin(\omega t)$  by a square wave current  $I_{\text{coil}}(t) = \pm I_{\text{step}}$ , the average mechanical power generated can be written as

$$P_{\text{mech,avg}} = V_{\text{emf,avg}}I_{\text{step}} \quad (4.5)$$

where  $V_{\text{emf,avg}}$  is the  $1/4^{\text{th}}$ -cycle average of the periodic back-emf as shown in Fig. 4.2. Note that we are making the assumption that all of the mechanical power generated electrically can be used to drive the wings. The basis for this assumption lies in the fact that the transmission doesn't have any internal damping by design (as we will see in a later section) and thus transmits the generated power perfectly to the wings.

For our application we design around  $P_{\text{mech,avg}} = 5\text{mW}$  as this much power is expected to be adequate to generate  $1\text{mN} = 100\text{mg}$  lift [20, 27]. For insects, their actuator mass (that is, muscle mass) is approximately 50% of their body mass giving their muscle power density at or below  $100\text{W}/\text{kg}$ .

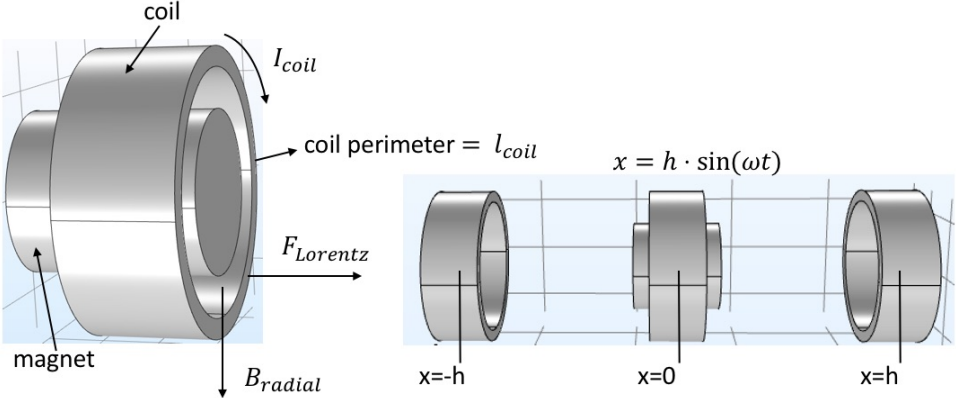


Figure 4.1: Lorentz force and the relative motion between the coil and magnet.

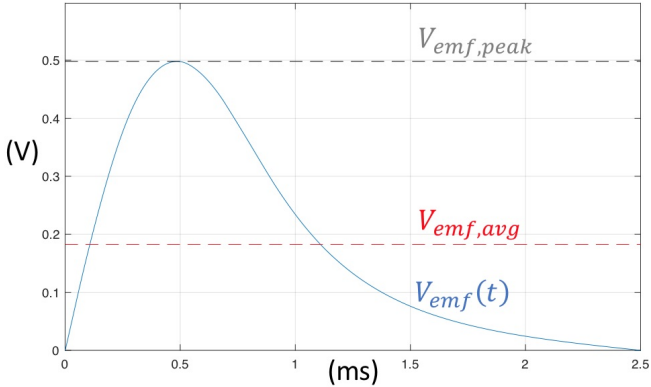


Figure 4.2: Simulation of generated back emf using equation 4.4 for  $h = 3.1\text{mm}$  and  $f = 100\text{Hz}$ . Simulation interval is 25% of the motion cycle from zero to full positive ( $+h$ ) relative separation between the coil and magnet (with the complete cycle comprised of 4 parts in this order: 0 to  $+h$ ,  $+h$  to 0, 0 to  $-h$  and  $-h$  to 0.). This operating point corresponds to the 2<sup>nd</sup> row in Table 4.4.

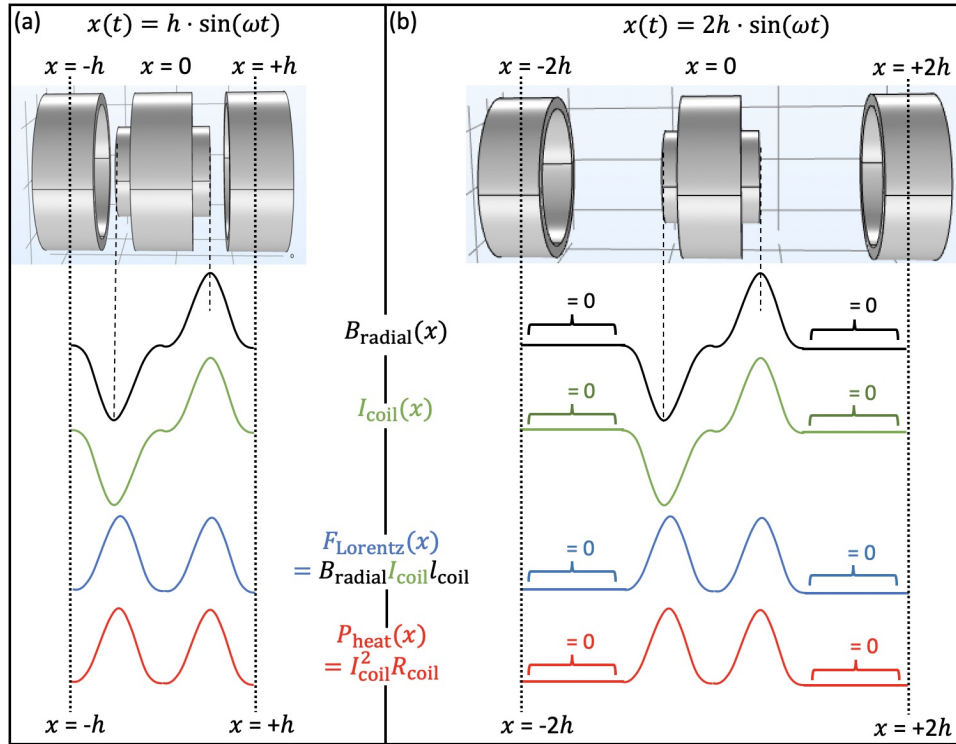


Figure 4.3: Effect of doubling the coil's travel on the various quantities.

### 4.3 Increasing Coil's Travel

Now we describe a power saving strategy employed which involves increasing the travel of the coil while keeping everything else the same. The coil undergoes simple harmonic motion (SHM) with the magnet as the center (see Fig. 4.3(a)). During half a cycle it goes from the extreme left (that is,  $x = -h$ ) to the extreme right ((that is,  $x = +h$ )), and always has a positive velocity  $\dot{x}(t)$ . The coil traverses both the pole faces of the magnet once and sees a certain effective radial magnetic field distribution  $B_{\text{radial}}(x)$ , simplified here for illustration. We assume that beyond a certain distance  $h$  away from the magnet's center the field drops to zero and stays at zero beyond this distance (in contrast to gradually decaying off to zero). A coil current  $I_{\text{coil}}(x)$  is maintained such that its sign matches the radial field's sign at each position  $x$  in this half cycle. This ensures that the coil always experiences a positive force  $F_{\text{Lorentz}}(x) = B_{\text{radial}}(x) \cdot I_{\text{coil}}(x) \cdot l_{\text{coil}}$  and thus only positive work is done on the coil at each position. During this period a positive parasitic power  $P_{\text{heat}}(x) = I_{\text{coil}}^2(x) \cdot R_{\text{coil}}$  is always lost through Joule heating.

If we now, say, double the travel amplitude of the coil to  $\pm 2h$  (see Fig. 4.3(b)), the radial field strength will be zero for the extra distance added because it is too far from the magnet. We keep the current as the same function of  $x$  as before for  $|x| \leq h$ , and  $= 0$  for the new region  $h < |x| \leq 2h$  added. Thus, the same force  $F_{\text{Lorentz}}(x)$  and the same heat loss

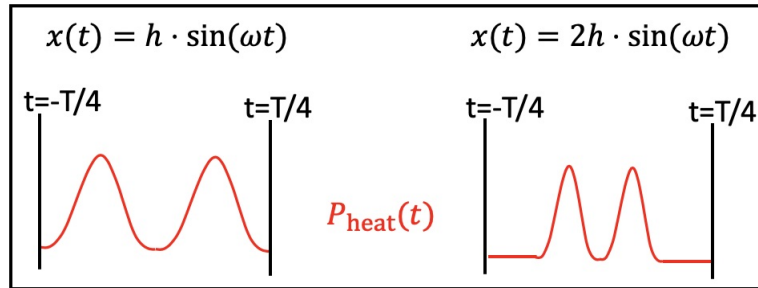


Figure 4.4: Effect of doubling the coil's travel on heat dissipation.

profile  $P_{\text{heat}}(x)$  is produced, which is again  $= 0$  in the new region added. The same work  $W_{\text{mech}} = \int_{-2h}^{2h} F_{\text{Lorentz}}(x)dx$  is done on the coil as the area under the  $F_{\text{Lorentz}}(x)$ -vs- $x$  graph remains the same as before.

The average heat loss in this half cycle is given by  $P_{\text{heat, avg}} = \frac{2}{T} \int_{-\frac{T}{4}}^{\frac{T}{4}} I_{\text{coil}}^2(x(t))R_{\text{coil}}dt$ , where  $\frac{T}{2}$  is the length of this half cycle. Let us look at the Joule heating  $P_{\text{heat}}(x(t))$  as a function of time  $t$  instead of displacement  $x(t)$  (see Fig. 4.4). The first case has the current ON for the entire cycle, but the second case has the current OFF from  $t = \frac{T}{2\pi} \sin^{-1}(\frac{h}{2h}) = \frac{T}{12}$  to  $t = \frac{T}{2\pi} \sin^{-1}(\frac{2h}{2h}) = \frac{T}{4}$ , that is, the current is OFF for two-thirds of the time. Hence only 1/3rd heat is lost compared to the first case as area under the  $P_{\text{heat}}(t)$ -vs- $t$  graph has reduced. This might appear non-intuitive at a first glance since the extra distance traveled by the coil is in a weak/zero field region, but the advantage arises from the current being OFF for two-thirds of the time, while still doing the same mechanical work. In practice, due to the gradual decay of the field, heat loss is only reduced by  $2\times$  instead of  $3\times$ , and the corresponding power saving current should only be turned OFF for the latter half of the cycle instead of the latter two-thirds of the cycle.

## 4.4 Mechanical Transmission

A widely used strategy across contemporary works is to convert the linear motions of a given actuator to desired biomimetic rotary  $\pm 60^\circ$  wing stroke motions using a mechanical transmission stage driven by the actuator. Here instead of moving the actuator linearly along  $\pm h$  we move it along a circular  $\pm \theta_{\text{rot, max}} \approx \pm 60^\circ$  trajectory, thus eliminating the need for a separate transmission (see Fig. 4.5). Simulated values for  $f = 100\text{Hz}$  using equations 4.4, 4.10 and 4.11 are reported in the 1<sup>st</sup> row of Table 4.4.

The actuator inertia is driven along the shown path periodically using a torsional spring of spring constant  $k_{\text{rot}}$ . The radius of the circular path is set at  $l = 4\text{mm}$  henceforth, and the magnet is set to be the moving component for now. For resonant operation around  $f_{\text{res}} = 100\text{Hz}$  a spring constant of  $m_{\text{magnet}}l^2(2\pi f_{\text{res}})^2 = 145\mu\text{Nm}$  is needed. We select  $k_{\text{rot}} = 290\mu\text{Nm}$  to provide a safety margin of  $2\times$  to compensate for parasitic inertia of frames and glue, and

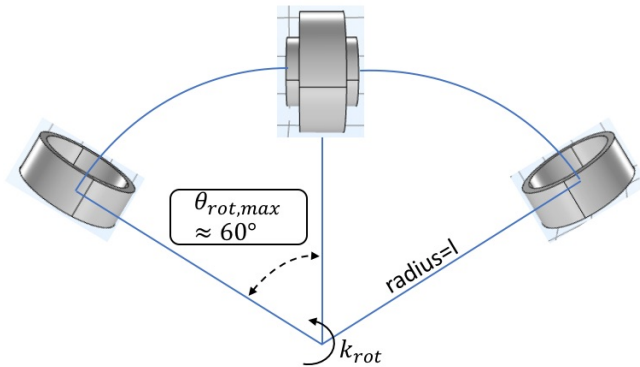


Figure 4.5: Integrating transmission into the actuator to directly output biomimetic kinematics.

Table 4.1: Steel vs Titanium as the spring material.

	Steel (301 Stainless)	Ti-6Al-4V (Grade 5)
Y	200 GPa	114 GPa
$\rho$	8000 kg/m <sup>3</sup>	4400 kg/m <sup>3</sup>
$\epsilon_{max}$ (fatigue limit)	0.25%	0.43%
Energy density	26 $\mu$ J/mg	69 $\mu$ J/mg
	cheap, many thicknesses	expensive, limited thicknesses

also assembly and operational deviations. Note that peak aerodynamic torque  $\tau_{aero,max} \approx (1\text{mN}) \cdot (\text{at } 5\text{mm radius}) = 5\mu\text{Nm} \ll \tau_{elastic,max} = k_{rot} \cdot (\theta_{rot,max} \approx 1) = 290\mu\text{Nm}$ , which means aerodynamic forces are expected to have negligible influence on actuator motion.

## 4.5 Spring Material Choice

The desired torsion spring will store elastic energy during its periodic motion, and elastic energy is quadratically related to stress. Thus the first important thing to check is the maximum stress tolerable by the spring material in order for it to withstand multiple cycles of operation (see Fig. 4.6). Note that as the number of cycles of operation increases, the material needs lesser stresses to fail. However, for some alloys of Iron and Titanium there exists a threshold value of stress (or, strain) below which the material can withstand infinite cycles of operation. It is this fatigue limit  $\epsilon_{max}$  that we would like our strains to be around (see Table 4.1).

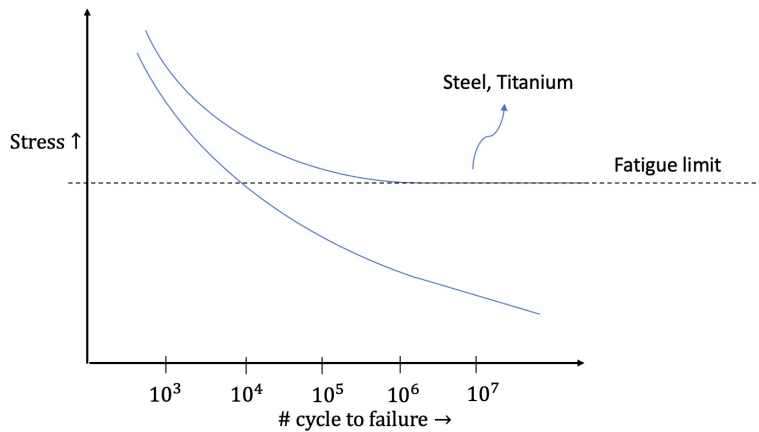


Figure 4.6: Fatigue in spring materials. Choosing spring material based on fatigue limit.

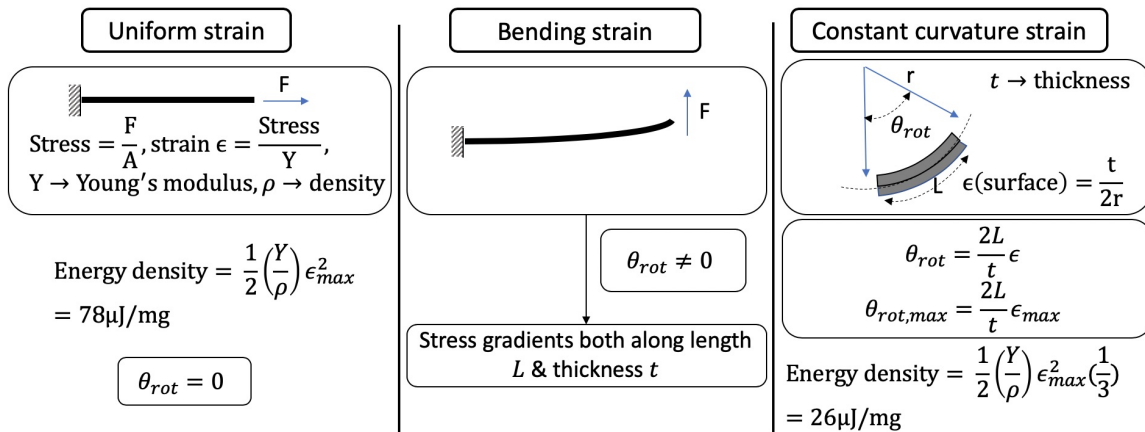


Figure 4.7: Spring energy density for different modes of beam bending.

## 4.6 Spring Energy Density

Stresses are the material's way of bending and storing energy (see Fig. 4.7). The most efficient way of storing energy is using uniform strains, but the issue is there are no sought-after rotations ( $\theta_{rot} = 0$ ) in this mode. Bending cantilevers do produce rotations, but due to stress gradients across both the surface and thickness only a little volume of the material experiences maximum stress. We can do better by at least eliminating surface stress gradients by bending the beam at a constant radius of curvature. This results in more rotation and more stored energy for the same amount of spring material. The spring energy density values shown in Fig. 4.7 are for 301 stainless steel.

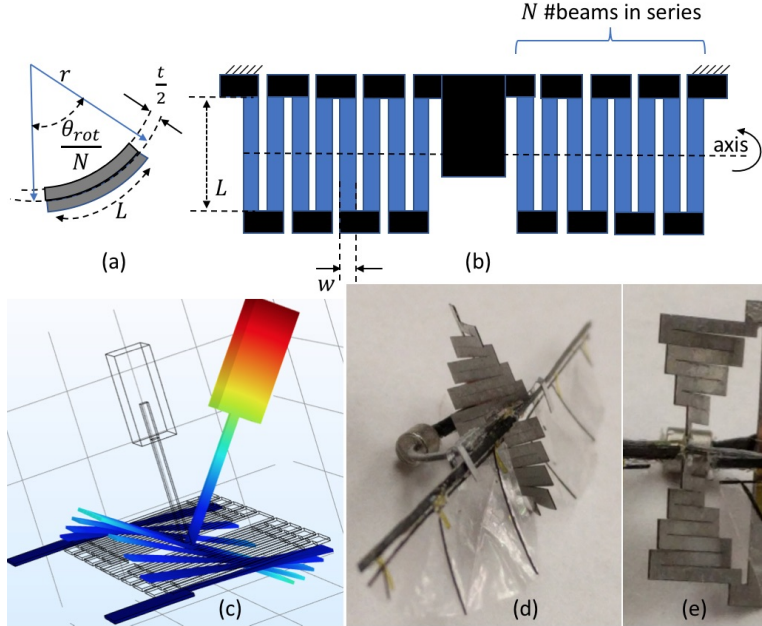


Figure 4.8: (a) A single cantilever beam in constant-curvature bending. (b)  $N$  cantilever beams in series, with 2 such groups arranged to act in parallel, making total number of beams= $2N$ . (c) Dominant resonant mode of operation of the spring + resonant mass system, with the resonant mass modeling the magnet placed at 4mm from the rotation axis. Color coding represents displacement. (d) Torsional rotation of  $\theta_{rot} = 60^\circ$  as seen in the fabricated  $\mu$ bot. (e) Progressively increasing rotation of the spring as one moves towards the center. The small rotations of the individual beams add up.

## 4.7 Spring Design

The challenge now is the design of a light-weight compliant torsion spring of constant  $k_{rot}$  with large rotations ( $\pm 60^\circ$ ) possible. The problem with beams of reasonable thicknesses and stiffnesses is they are only able to rotate a little before plastically deforming. To solve this problem, we take multiple beams and add up their individual rotations to produce a large net rotation. This is done by connecting the individual beams in series using rigid connectors (see Fig. 4.8 (b)). We test its behavior using finite element simulation on the application of a pure torque about the central axis (see Fig. 4.9). We observe constant surface stresses thus confirming constant curvature operation.

The surface strain on the individual beams is (see Fig. 4.8(a))

$$\epsilon = \frac{t}{2r}, \text{ with } r = \frac{L}{\theta_{rot}/N}. \quad (4.6)$$

The elastic energy density in a constant-curvature beam is  $1/3^{\text{rd}}$  that in a uniform strain

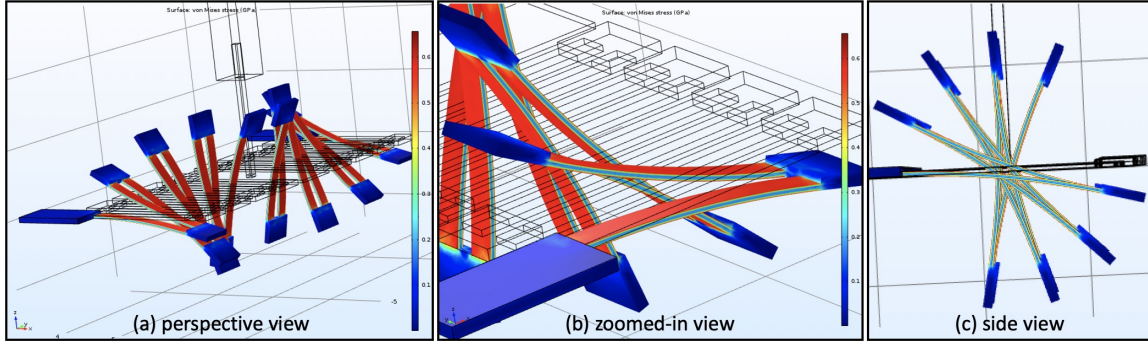


Figure 4.9: Constant surface stresses.

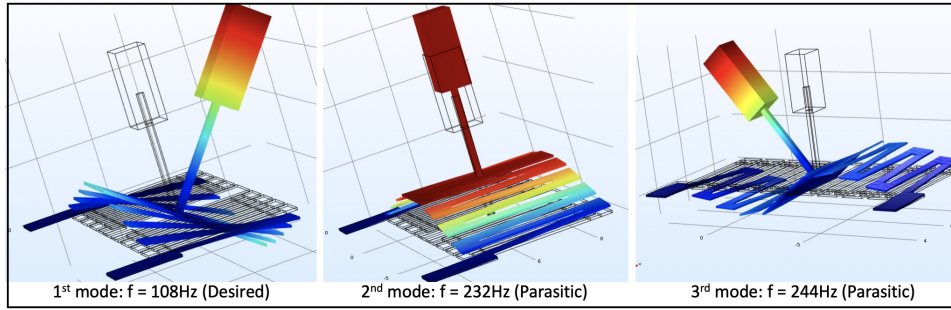


Figure 4.10: Desired and parasitic resonant modes of the spring-mass system.

beam, giving the total spring energy as (see Fig. 4.8(b))

$$\left( \frac{1}{3} \times \frac{Y}{2\rho} \epsilon^2 \right) \cdot (\text{net mass} = 2N\rho Lwt) = \frac{1}{2} k_{\text{rot}} \theta_{\text{rot}}^2 \quad (4.7)$$

where  $Y$  is the Young's modulus and  $\rho$  is the density of the material. We select full-hard 301 stainless steel (see Table 4.1) as our spring material for now because of its ease of availability at different thicknesses and cheap cost, and assume its fatigue strength to be half that of its yield strength.  $\theta_{\text{rot,max}}$  is set at  $90^\circ > 60^\circ$  to provide a margin of safety during operation. The following is the procedure we follow to calculate the spring dimensions.

- We fix a certain number of segments that make up the spring, say,  $N = 8$ .
- Stainless steel sheets are only available in certain thicknesses  $t$ , which are integral multiples of  $25.4\mu\text{m}/2$ , that is,  $t = k \times 25.4\mu\text{m}/2$ , where  $k = 1, 2, 3, \dots$  is an integer. We do a parameter sweep on  $k$ .
- Having fixed  $N$  and  $k$ , the remaining 2 free parameter ( $L$  and  $w$ ) get determined by equations 4.6 & 4.7.

Table 4.2: Spring Specs.

$Y$	190 GPa	$t$	$76\mu\text{m}$
$\epsilon_{\text{max}}$	0.25%	$w$	0.5mm
$k_{\text{rot}}$	$290\mu\text{Nm}$	$N$	8
$\theta_{\text{rot,max}}$	$\pi/2 = 90^\circ$	$L$	3mm

- We compute the resonant modes of the spring-mass system using finite element simulation. If the resonant modes are satisfactory (see Fig. 4.10), that is, if the higher resonant modes are far away from the dominant mode, then we freeze the spring dimensions.
- If the resonant modes are not satisfactory, we move on to the next thickness  $k$  and repeat the above steps.

The final spring parameters obtained using this procedure are shown in Table 4.2.

## 4.8 Spring Non-idealities

In practice, the connectors and the beams develop stress concentrations near their connection points even with practical amounts of filleting (/rounding the corners) as shown in Fig. 4.11. These stress concentrations reduce device life. Further, the loading on the spring is not a pure torque but mixed with centripetal forces due to the rotating mass thus causing a stress gradient across the length of the beams due to dynamic shifts in the rotation axis (see Fig. 4.12). One of the strategies to reduce the peak stresses, say by half, is to increase the spring volume by 4 times. One of the many possible ways of doing this, without changing the spring's torsional or off-axis stiffnesses is shown in equation 4.8.

$$\epsilon \propto \frac{t}{NL}, \quad N \uparrow 3\times, t \uparrow 1.5\times \Rightarrow \epsilon \downarrow 2\times \quad (4.8)$$

$$k_{\text{rot}} \propto \frac{1}{N} \frac{t^3 w}{L} \approx \text{constant}, \quad k_{\text{off-axis}} \propto \frac{1}{N} \frac{t^3 w}{L^3} \approx \text{constant}$$

While we note the above non-idealities, currently we do not tackle the problem of increasing the working life of our prototypes and ignore any sharp corners and increased stresses in the spring.

## 4.9 Wing Fabrication

The wing fabrication procedure used here is similar to that outlined in [30] but instead of using an integrated flexure along the leading edge formed by the same material as the wing membrane, we use thicker Kapton film beams along the leading edge since that results in

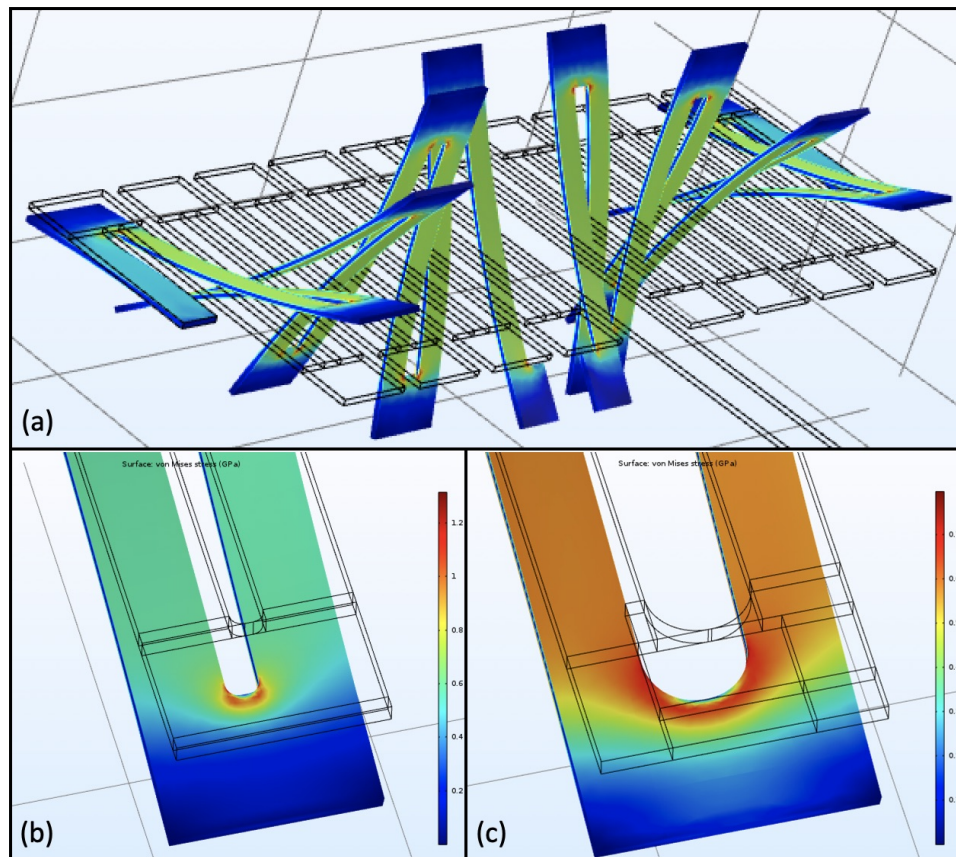


Figure 4.11: Spring stress concentrations and filleting. (b) Higher stresses seen near a sharp corner. (c) Lower stresses seen near a more rounded corner.

higher feature sizes and thus ease in assembly and fabrication. The layup is cured and then manually cut as shown in Fig. 4.13 to release the hinges. The fatigue life of the manufactured wings is  $\approx 30$ mins with Kapton flexure being the point of failure.

## 4.10 Assembly

The different device components are described in Fig. 4.14. Magnet frames constructed from Aluminum (Al) are fitted perpendicularly to the center of the spring using slots and then glued together. The coil is tension-fit into the coil frame, and with the coil in place the magnet is tension-fitted in the circular magnet frame's gap, aligned manually, and then glued to it. The thicker leading edge on the wing is glued to the straight portion of the Al magnet frame, and small Al rotation-stops are glued to this straight portion as well to restrict wing pitch to  $< 50^\circ$ . Table 4.3 shows the mass distribution of the assembled  $\mu$ bot, and Fig. 4.15 shows different views of the assembled device.

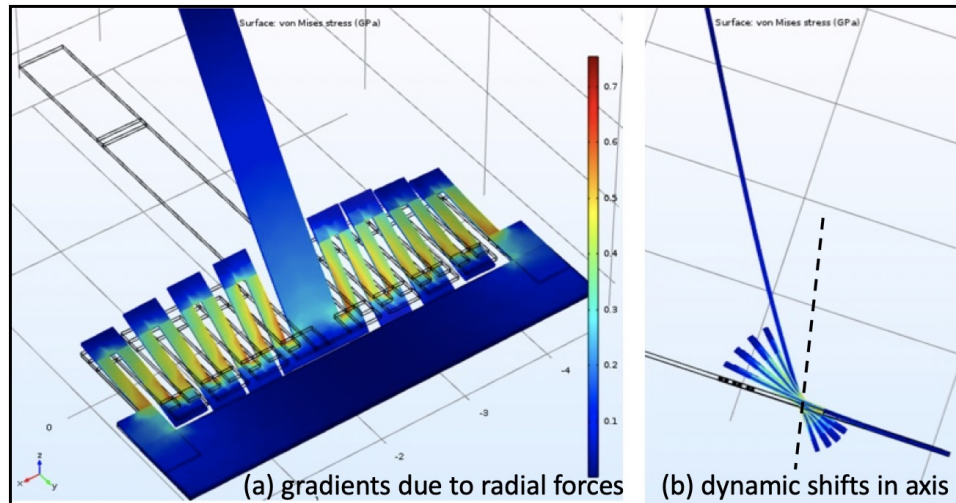


Figure 4.12: Spring non-idealities. (a) Stress gradient across the length of the beams caused due to the (b) dynamic shifts in the rotation axis.

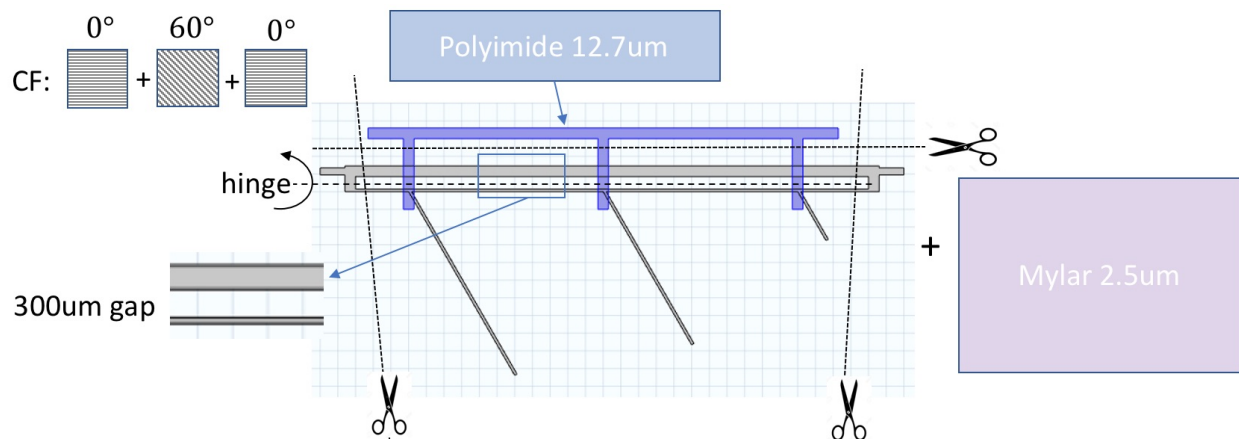


Figure 4.13: Wing fabrication assembly. The layup consists of (a)  $0^\circ$ - $60^\circ$ - $0^\circ$  aligned  $30\mu\text{m}$ -thick CF prepreg layers laser-cut to act as  $60\mu\text{m}$  wide veins, (b) A wider CF leading edge creating a gap of  $300\mu\text{m}$  for the flexure, (c) Three  $12.7\mu\text{m}$  thick Kapton beams on the leading edge gap acting as a flexure hinge, (d)  $2.5\mu\text{m}$  Mylar acting as wing membrane.

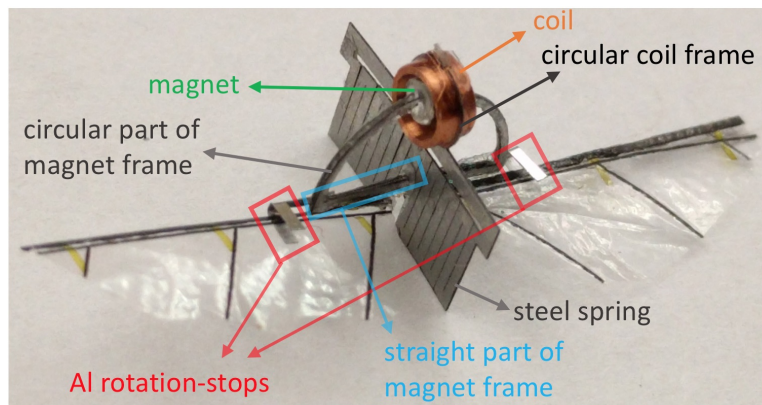
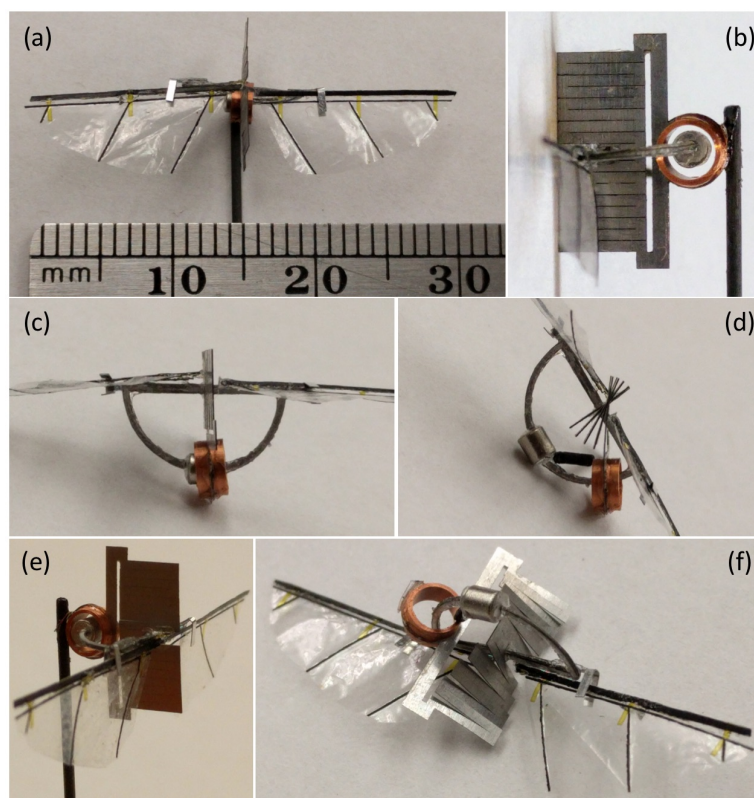
Figure 4.14: Different parts of the  $\mu$ bot.

Figure 4.15: Different views of the fabricated  $\mu$ bot. (a) Front view comparison with a ruler showing wing-span of 3cm. (b) Side view showing clearance between the coil and the magnet. (c) Top view showing semi-circular magnet frame. (d) Top view at an extreme stroke position. (e) Perspective view. (f) Perspective view at an extreme stroke position.

Table 4.3: Mass distribution.

Components	Mass (mg)
coil	15
spring + coil frame	22
magnet	23
magnet frame	2
wings	$2 \times 0.4$
glue	5
Total	$\approx 70$

## 4.11 Power Efficiency

Here we calculate the expected Joule heating in the coil for a desired mechanical power output of the actuator. This is done by measuring the coil resistance, the back-emf produced (see Fig. 4.28 and equation 4.9), and the spring's rotation amplitude when the system is driven at resonance using a small voltage ( $V_{in} = \pm 1V$  square wave) without any wings, that is, without any significant damping.

$$\frac{V_{out}}{R_s} = \frac{V_{in} - V_{emf}}{R_{fx} + R_{coil} + R_s} \Rightarrow V_{emf}(t) = V_{in}(t) - 18.5V_{out}(t) \quad (4.9)$$

Using 4.5, the required current magnitude for a desired mechanical power output is given by

$$I_{step} = \frac{P_{mech,avg}(\text{desired}) = 5\text{mW}}{V_{emf,avg}} \quad (4.10)$$

and thus the predicted power loss in heat can be given by

$$P_{heat,avg} = I_{step}^2 R_{coil}. \quad (4.11)$$

Measurements along with predicted heat loss and power efficiency are reported in the 3<sup>rd</sup> row of Table 4.4. It is important to note that this factors out the inefficiencies in the design caused by unoptimized wing shape and wing pitch amplitude. As a result the observed lift will be lower than that predicted using the available mechanical power and modeled kinematics. However, with the tuning of the design it is possible to achieve the modeled lift numbers.

## 4.12 Flapping Motion Using External Power

Wing kinematics are recorded at  $V_{in} = \pm 8V$  square wave input. An  $f_{res}$  of 98Hz with wing stroke and wing pitch of  $\pm 45^\circ$  is observed (see Figs. 4.17, 4.18 & 4.19). Since  $V_{in} \gg V_{emf,peak}$ , the current is almost a square wave with amplitude  $I_{step} \approx \frac{8}{R_{fx} + R_{coil} + R_s}$ . The

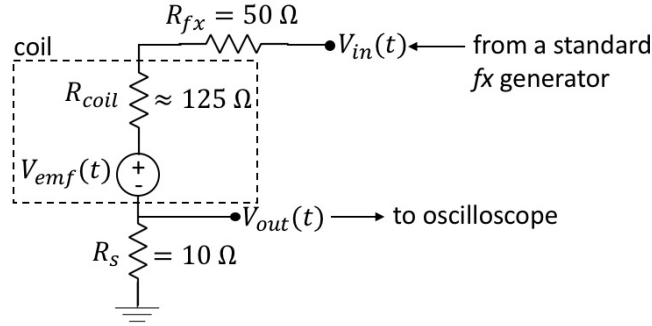
Figure 4.16: Effective circuit diagram of the EM actuator and the set-up for measuring  $V_{emf}$ .

Table 4.4: Predicted (/simulated) and measured heat loss and efficiency values.

	$f_{res}$	$\theta_{rot}$	$V_{emf, peak}$	$V_{emf, avg}$	$P_{mech}$	$I_{step}$	$R_{coil}$	$P_{heat}$	eff.
Sim. #1	100Hz	60°	0.69 V	0.19 V	5mW	26mA	116 $\Omega$	79mW	6%
Sim. #2	100Hz	45°	0.50 V	0.18 V	5mW	27.5mA	116 $\Omega$	88mW	5.4%
Meas. #1 (no wings)	98Hz	45°	0.55 V	0.18 V	5mW	27.5mA	125 $\Omega$	95mW	5%
Meas. #2 (2 wings)	98Hz	45°	0.55 V	0.18 V	8.1mW	45mA	125 $\Omega$	253mW	3%

measured resonance frequency, stroke amplitude,  $V_{emf}(t)$ ,  $I_{step}$  and  $R_{coil}$  are used to compute the mechanical power output  $P_{mech}$  and heat loss  $P_{heat}$  and these values are reported in the 4<sup>th</sup> row of Table 4.4.

Lift is measured using a simple setup shown in Fig. 4.20 wherein the  $\mu$ bot is mounted onto a clamp placed on a 0.2mg resolution weighing scale. Lift values  $> 60$ mg are observed during this operation. As expected, the lift generated is lower than that predicted for the available mechanical power. A summary of the fabricated  $\mu$ bot is provided in Table 4.5.

As can be seen, our actuator generates a lift of  $60\text{mg} = 0.6\text{mN}$  using  $8.1\text{mW}$  of estimated mechanical power output. The power density of this actuator is thus  $115\text{ W/kg}$  which is close to the  $100\text{W/kg}$  figure for the power density of insect muscles [27]. Even though we initially designed our actuator to run at  $5\text{mW}$  power output, the transduction from power to lift is imperfect and  $60\%$  more power was needed, implying  $2.5\times$  heat power loss. The reason behind this, as mentioned earlier, is tuning the degree of wing pitch and wing length, aspect ratio and shape to the operational frequency and stroke amplitude of the driving actuator.

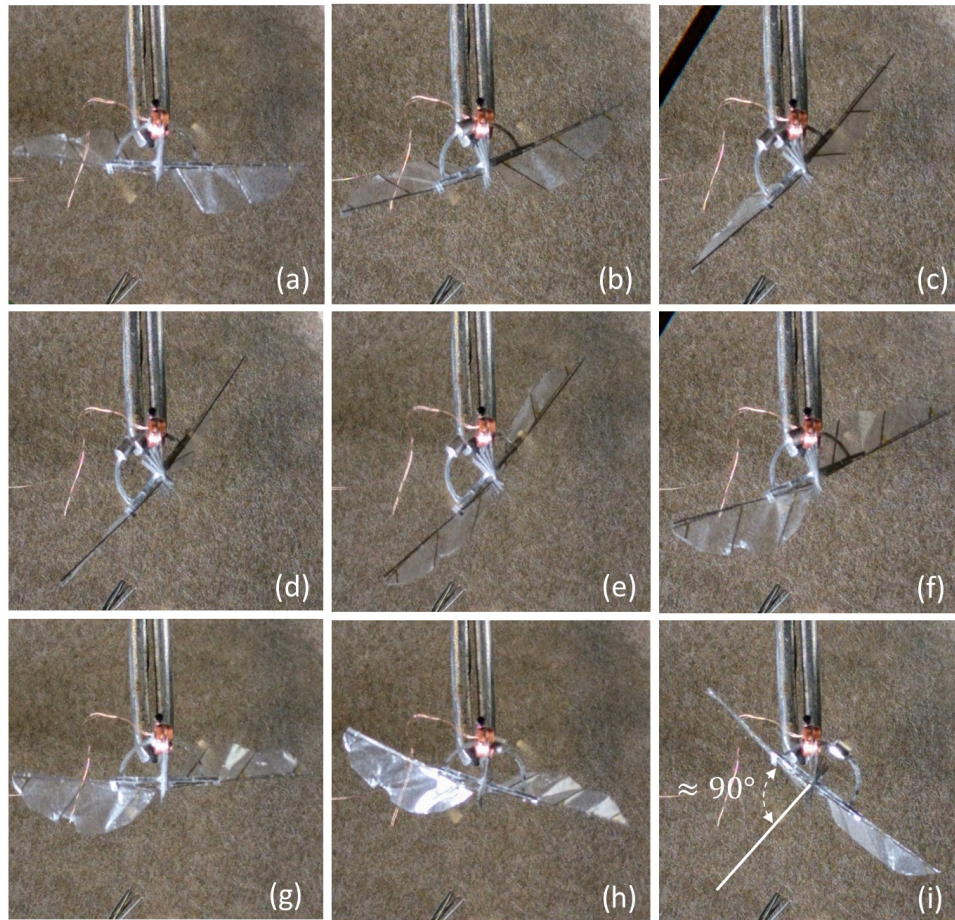


Figure 4.17: (a)-(g) 25% of cycle with  $\theta_{\text{rot}}(t)$  from mid-stroke to mid-stroke showing wing pitch reversal (top view). (i) Stroke amplitude measurement between 2 extreme wing positions.

Table 4.5: Summary of  $\mu$ bot Specs.

$\mu$ bot mass	70 mg
$f_{\text{res}}$	98 Hz
EM actuator power density	115 W/kg
Operating Voltage	5.5 V
$P_{\text{heat}}$	253 mW
Efficiency	3%
Wing stroke	$\pm 45^\circ$
Wing pitch	$\pm 45^\circ$
Lift	$> 60$ mg

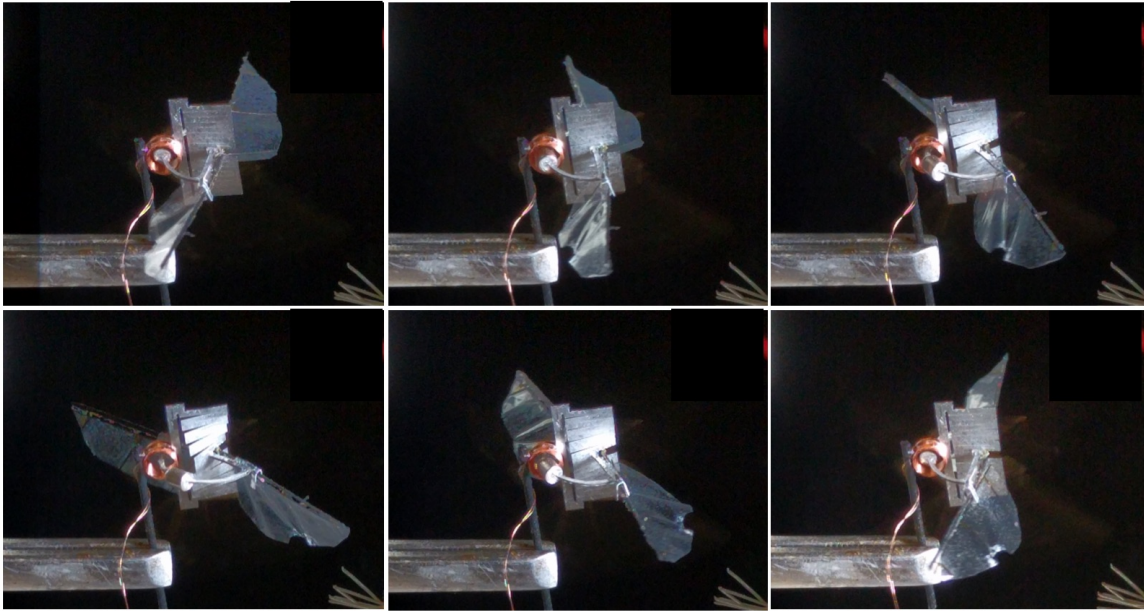


Figure 4.18: 25% of cycle between highest angle-of-attack positions showing wing pitch reversal (perspective view).

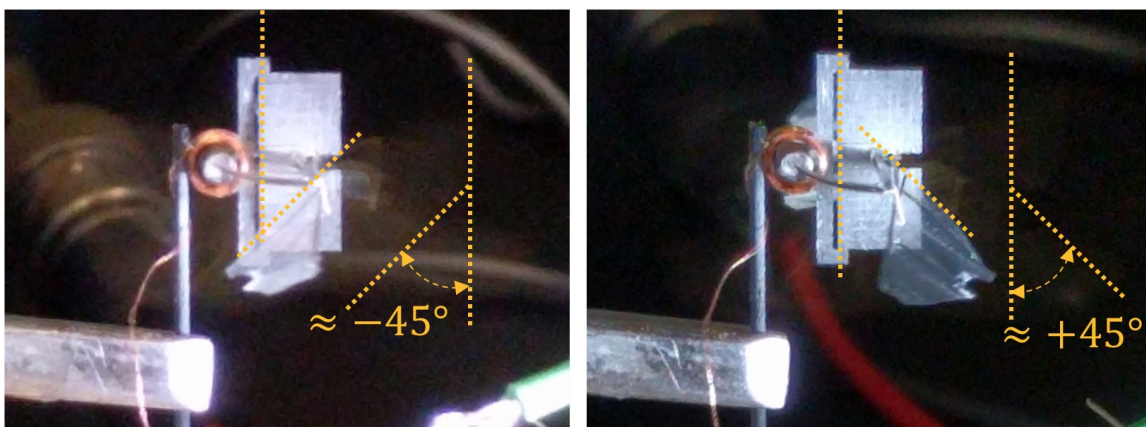


Figure 4.19: Most negative and most positive wing angle-of-attack seen during mid-stroke (side view).



Figure 4.20: Setup for the measurement of average lift.

### 4.13 Further Increasing Actuator Efficiency

Note that we drove our actuator using a simple square wave voltage. This means the coil current was ON during the entire cycle, but as discussed before we could have switched it OFF for the latter half of the cycle while keeping the generated mechanical power almost the same. Had we done that our heat loss would have been close to half of its current value of  $253\text{mW} \Rightarrow \approx 126\text{mW}$  instead. However, even this much consumed power would have been too high. In order to drive our actuator using practical power sources, we need to make sure that our low-voltage actuator requires low-power as well, ideally  $< 40\text{mW}$ .

So another thing we do to further reduce the power loss is use 2 magnets instead of one. The benefit is mathematically straightforward here since with the extra field the coil can do the same amount of mechanical work using a lower current, thus reducing resistive heat loss. Carrying out this step however isn't as trivial. We now move our single coil and keep the magnets stationary as opposed to moving the heavier set of 2 magnets that would result in a bulkier spring. Fig. 4.21 shows how we want our single coil to move through the two magnets, with the two magnets placed  $\pm 30^\circ$  relative to the coil's neutral position. The magnet used is the same as before with diameter = 1.6mm, but the coil we use now is the one used on the jumping  $\mu$ bot which has an inner diameter of 1.9mm. This is a reduction of 0.6mm in diameter from the previous coil version and is done so that the coil gets closer to the magnet and sees higher magnetic fields thus needing lower currents to produce the same mechanical power, further reducing power loss.

With the above two changes, the value of  $V_{\text{emf,avg}}$  increases. Using 2 magnets changes  $V_{\text{emf,avg}}$  from the previous value of 0.18V to 0.32V. Shrinking the coil diameter further increases this to 0.4V, while also reducing the  $116\Omega$  coil resistance by 20% to  $91\Omega$ . Using equation 4.10, producing 8.1mW of mechanical power would now only need  $\frac{8.1\text{mW}}{0.4\text{V}} \approx 20\text{mA}$  of current, and burn only 37mW of power (using equation 4.11).

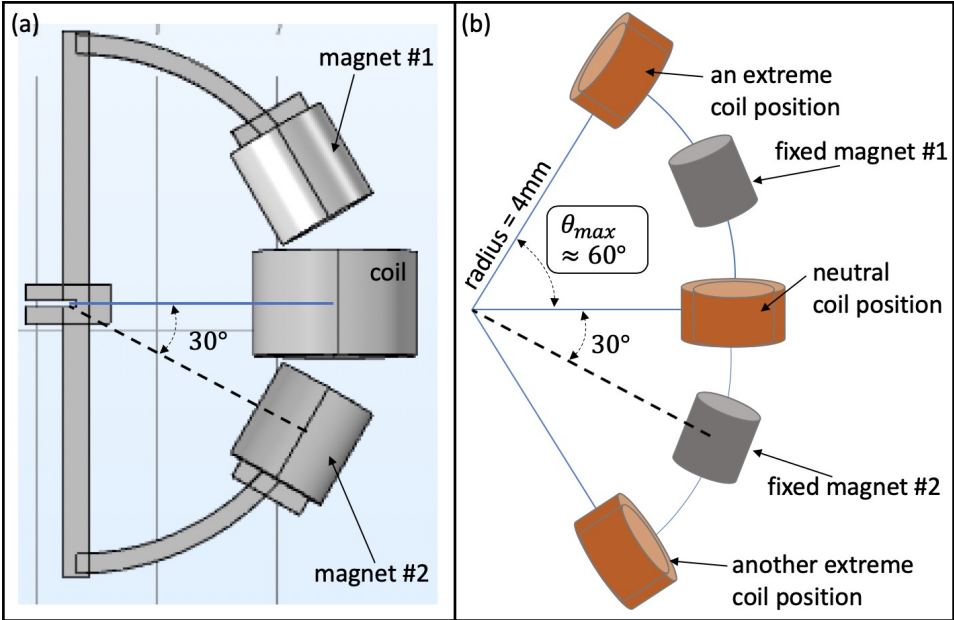


Figure 4.21: Intended route of the coil through the double magnet assembly.

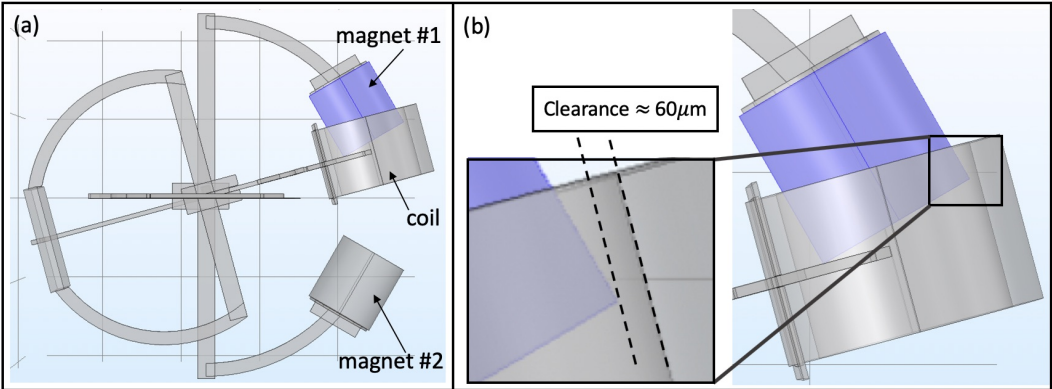


Figure 4.22: Worst case clearance between the coil and the magnet.

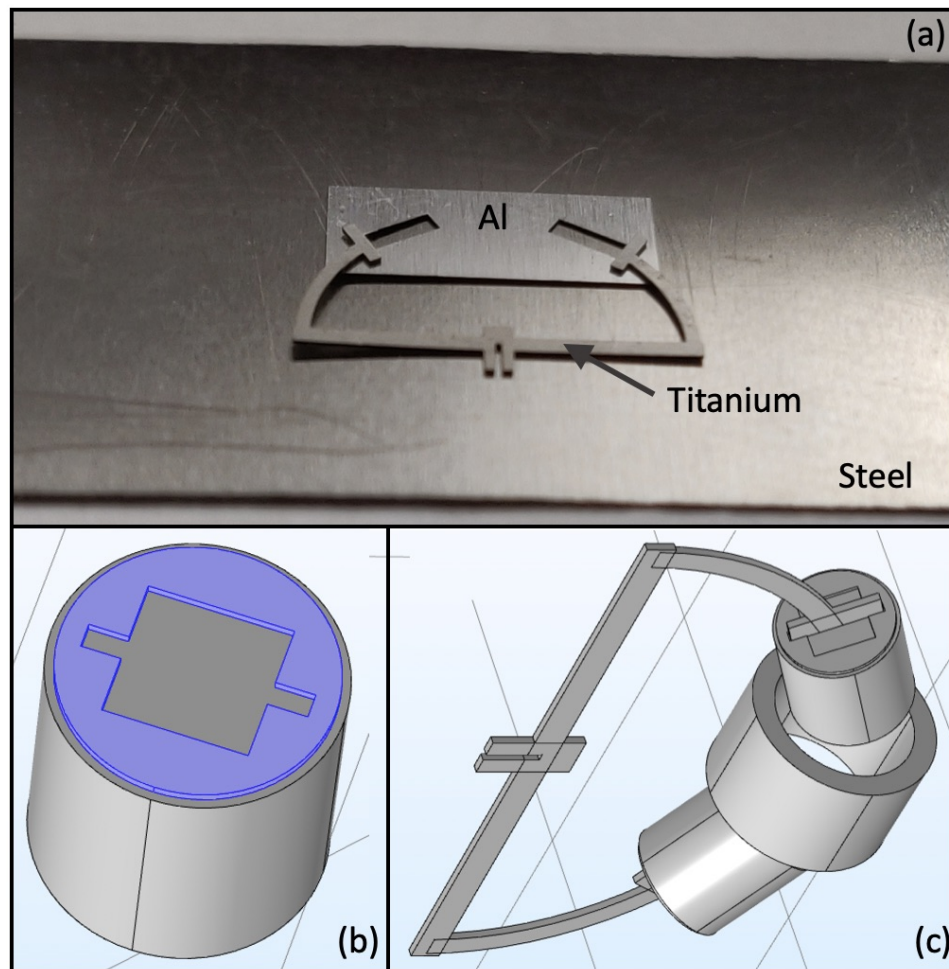


Figure 4.23: Steps in precision assembly of the 2 magnets.

### Precision assembly

If the coil moved along a straight path concentric to the magnet, the clearance between the coil and the magnets would have been  $150\mu\text{m}$ . But due to the curved path the coil takes the clearance is closer to  $60\mu\text{m}$  (see Fig. 4.22). This means the coil should follow the desired circular trajectory very precisely to avoid colliding with the magnets. Also, the magnets should be positioned very precisely along the circular trajectory on the stationary D-shaped frame to begin with. The latter is accomplished as follows (see Fig. 4.23). Two 1.6mm-long slots are laser-cut on a  $50\mu\text{m}$ -thick aluminum sheet such that these slots are positioned at  $60^\circ$  relative to each other, and this Al sheet is placed over a mildly magnetic steel steel (see Fig. 4.23(a)). An Al disc with slots cut as shown in Fig. 4.23(b) is glued to a pole face of each of the 2 magnets. The 2 magnets are then placed in the 2 slots from the previous step (using their curved side), and they are held in place due to their attraction to the mildly

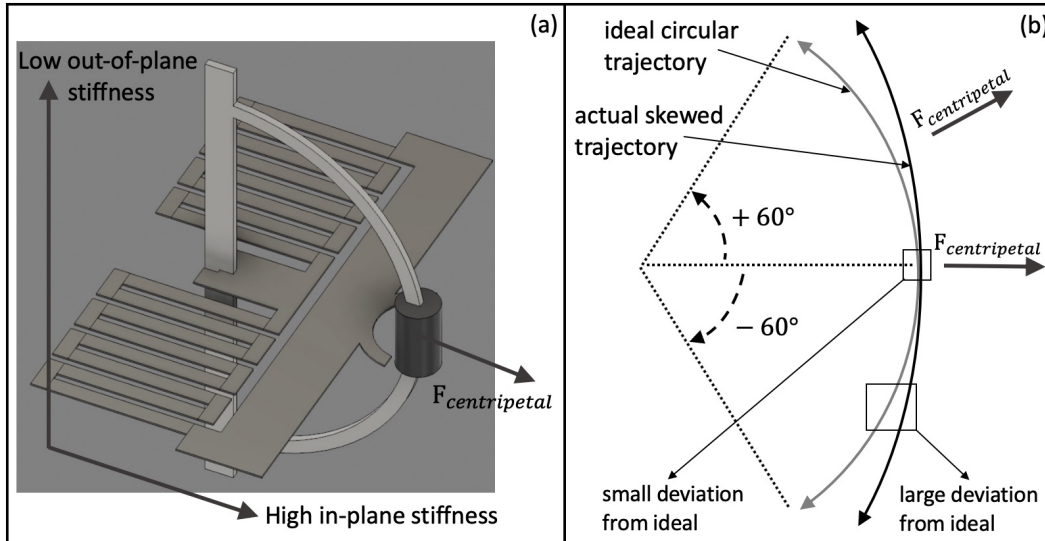


Figure 4.24: Low out-of-plane spring stiffness skewing the coil's trajectory.

magnetic steel. In this configuration, the laser cut Titanium D-frame is slid and glued into the narrow slots on the Al discs previously attached to the magnets' faces, and the resulting assembly is shown in Fig. 4.23(c).

## Precision kinematics

After precisely positioning the magnets along the desired circular path, another problem is to make the resonant kinematics of the coil be perfectly circular in order for it to avoid colliding with the magnet. But why wouldn't its trajectory be circular to begin with? There is a centripetal force  $F_{\text{centripetal}}$  always acting radially on the resonant mass (see Fig. 4.24(a)). The torsional spring previously designed is very stiff in the spring-plane but has a low stiffness in the orthogonal direction out of the plane. This is due to the spring beams having a higher width than their thickness. Thus the mass's path will be more eccentric than circular as is shown in Fig. 4.24(b) thus making it collide with the magnet. This problem was indeed observed during the operation of an intermediate double-magnet design. Note that collision is not a problem in the case of a single magnet placed at  $0^\circ$  because this eccentric trajectory well approximates the circular trajectory around this region (see Fig. 4.24(b)). The problem only arises when the magnets are placed away from  $0^\circ$  which is indeed the case when using multiple magnets.

The solution to the above problem is simple which is to add a counter-mass diametrically opposite to the coil, and weighing the same as the coil (see Fig. 4.25). This would ensure that the spring sees only pure torques and no net off-axis forces. This certainly solves the problem, but would add a useless mass of 12mg to our seriously mass-constrained device. So instead we design our power electronics unit to weigh around 12mg so we can use that

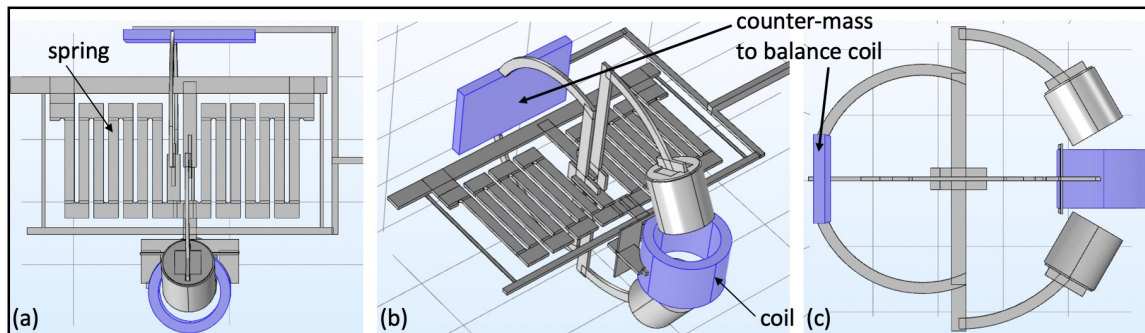


Figure 4.25: Diametrically opposite counter-mass to balance the coil.

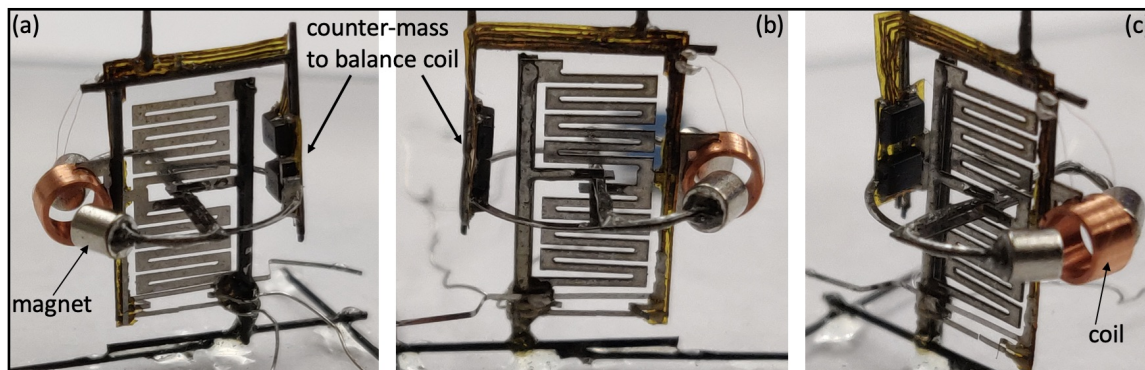


Figure 4.26: Electronics acting as the counter-mass in the assembled device.

to balance our system. Fig. 4.26 shows the designed power electronics unit acting as a counter-mass to balance the coil.

## 4.14 Power Electronics

The electronics unit for the rolling bot weighed 17mg which is more than our 12mg budget set above. We anyways do not intend to use that since one would have to pre-program the resonant frequency into its electronics which is undesirable. This is because the resonant frequency changes a lot both during and post fabrication. During fabrication the resonant frequency changes depending on the amount of glue used, part alignment errors, and other assembly imperfections. Post fabrication the resonant frequency changes due to the presence of variable wing damping, varying with changing amplitude of oscillations.

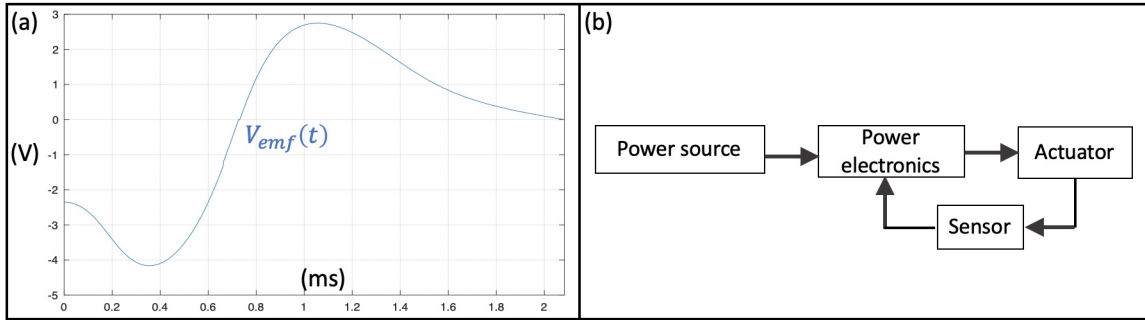


Figure 4.27: Plot of  $V_{emf}(t)$  in the actuator, and the structure of the sensing system acting on the actuator.

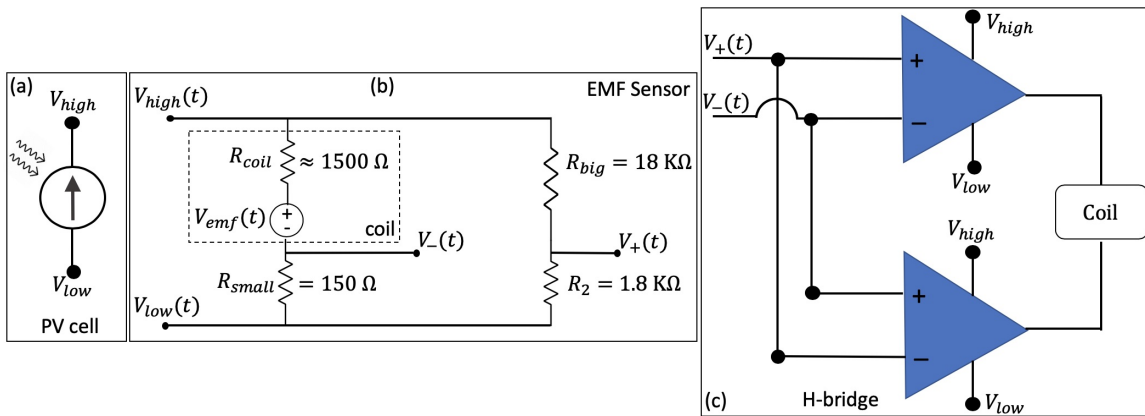


Figure 4.28: Conceptual circuit diagram of the proposed electronics.

## Proposed circuit

We desire an electronics unit that can always excite the coil current at the true resonant frequency of the spring-mass-damper system. Accomplishing this is actually quite simple. Fig. 4.27(a) shows the back-emf  $V_{emf}(t)$  seen by the coil because of its motion. The mechanical power generated in the coil is given by  $I_{coil}(t) \cdot V_{emf}(t)$ . In order to always generate positive mechanical power, the sign of the driving current  $I_{coil}(t)$  and the back-emf  $V_{emf}(t)$  should match. So our power electronics should somehow sense the back-emf from our actuator and based on that change the direction of the current supplied from the power source accordingly (see Fig. 4.27(b)).

Our power source is a PV cell which can be modeled as a constant current source (see Fig. 4.28(a)). Back-emf sensing is done by a simple resistive divider circuit, shown in Fig. 4.28(b), which outputs a voltage difference proportional to the back-emf, that is,  $V_+(t) - V_-(t) = \frac{V_{emf}(t)}{11}$ . We make sure that the series resistance  $R_{small}$  is an order of magnitude smaller than  $R_{coil}$ , and the parallel branch resistance  $R_{big} + R_2$  is an order larger than  $R_{coil}$ , so that this

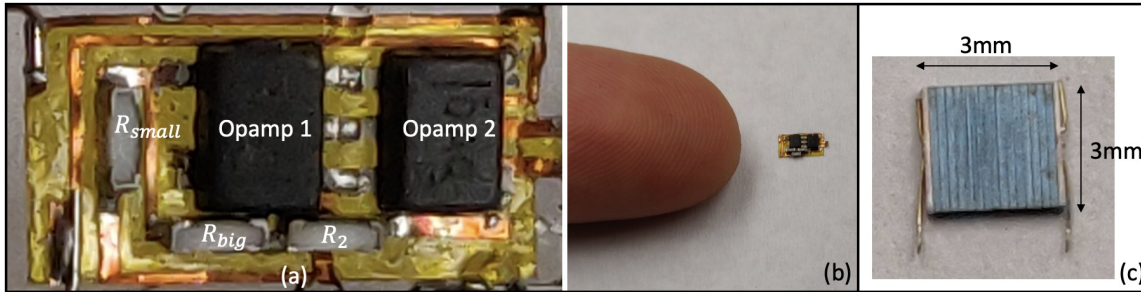


Figure 4.29: Fabricated 9mg circuit, compared to an index finger.

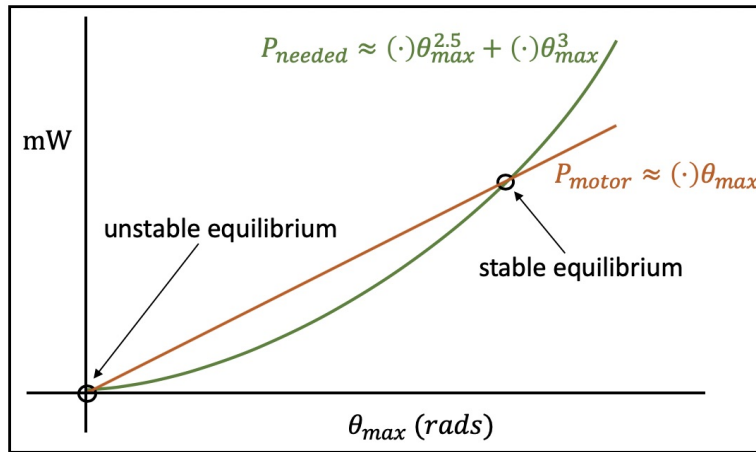


Figure 4.30: Stability of mechanical + actuator + electronics joint system.

sensing circuit consumes an order of magnitude smaller parasitic power than the resistive heat loss in the coil. This voltage differential output is then fed into an H-bridge we have seen before (see Fig. 4.28(c)) which connects the coil in the correct direction with the PV cell.

The result is an electronics unit weighing  $\approx 9\text{mg}$  (see Fig. 4.28(a),(b)). Note that this electronics unit is actually simpler than the electronics unit made for our rolling  $\mu$ bot since this one is made up only of 3 resistors and 2 opamps, and lacks any capacitors. Hence this unit is comparatively lighter as well. With this power electronics unit powering the coil using a constant current source, the system becomes self-resonating.

## Stability

Let us say we are operating the system using a current source at a fixed current value, like a PV cell receiving a fixed light intensity. We can plot the mechanical power generated  $P_{\text{motor}}$  and the mechanical power required  $P_{\text{needed}}$  as a function of the stroke amplitude  $\theta_{\text{max}}$  (see Fig. 4.30). We know that  $P_{\text{motor}} = I_{\text{coil}}(t) \cdot V_{\text{emf}}(t) \propto V_{\text{emf}}(t)$  since  $I_{\text{coil}}(t)$  is constant for

a constant current source. Now back-emf  $V_{\text{emf}}(t)$  is proportional to the coil's velocity, and linearly approximating the coil's curved trajectory with a simple harmonic motion gives the coil position  $x(t) = 4\text{mm} \cdot \theta_{\text{max}} \cdot \sin(\omega t) \Rightarrow V_{\text{emf}}(t) \propto |\dot{x}(t)| \propto \theta_{\text{max}}$ . Thus, the mechanical power generated is approximately linear in  $\theta_{\text{max}}$ . The mechanical power required to overcome wing damping is worked out in [17, 18, 19], and can be approximated using a positive linear combination of  $\theta_{\text{max}}^{2.5}$  and  $\theta_{\text{max}}^3$ .

What is more important than the exact equations for  $P_{\text{motor}}$  and  $P_{\text{needed}}$  is the nature of these 2 quantities as a function of  $\theta_{\text{max}}$ . Their functional form ensures that the  $P_{\text{needed}}$  curve is below the  $P_{\text{motor}}$  curve for small  $\theta_{\text{max}}$ , but eventually intersects the  $P_{\text{motor}}$  curve at some point  $\theta_{\text{max}}^*$  which then determines the operating point of system. Moreover, since the  $P_{\text{needed}}$  curve cuts the  $P_{\text{motor}}$  curve from below, we know from basic stability theory that this is a stable operating point of the system. Here is a brief justification - for the region just right of  $\theta_{\text{max}}^*$ , the required power is higher than the generated power and thus the resonant system will loose energy decreasing its oscillation amplitude  $\theta_{\text{max}}$  until it hits  $\theta_{\text{max}}^*$ . For the region just left of  $\theta_{\text{max}}^*$ , the required power is lower than the generated power and thus the resonant system will gain energy increasing its oscillation amplitude  $\theta_{\text{max}}$  until it reaches  $\theta_{\text{max}}^*$ .

## Photovoltaic cells

Regarding our constant current source, there is limited availability of small PV cells one can use on-board. We use an 8mg 3mm $\times$ 3mm infrared PV cell (MH GoPower 5S0303.4-W) that produces current when a 976nm wavelength laser light (MH GoPower LSM-010) is shone on it. As per the manufacturer's specifications, this cell can generate  $\approx 5\text{mA}$  at  $\approx 8\text{V}$  under  $1.4\text{W}/\text{cm}^2$  illumination while operating at  $25^\circ\text{C}$ . Thus it has good impedance matching with the  $\approx 1500\Omega$  resistance Copper coil we used on our rolling bot (and has  $\approx 16\times$  higher resistance than jumping bot's same-sized coil). This coil was custom made using the thinnest possible wire ( $= 12\mu\text{m}$  diameter) one could use for a machine wound coil, and thus this resistance value is the highest we can achieve for our coil. We require high coil resistance since the opamps used in our H-bridge have  $\approx 150\Omega$  parasitic series resistance at its output, and we want parasitic heat losses in our circuit to be an order of magnitude lower than the resistive heat loss in our coil.

## 4.15 Flapping Motion Using Photovoltaics (Without Wings)

The fully assembled device with the wings, spring, coil, magnets, power electronics and PV cell can be seen in Fig. 4.31, with the mass distribution outlined in Table 4.6. The device starts resonating as soon as the laser hits the cell, with the laser spot seen in green (see Fig. 4.31(c)). We first test the device without putting on wings, and using our laser source at a low intensity. Fig. 4.32 shows snapshots of the motion of the wingless device resonating at  $\approx 120\text{Hz}$ . We observe amplitude of rotations exceeding  $\pm 75^\circ$  which confirms the correct

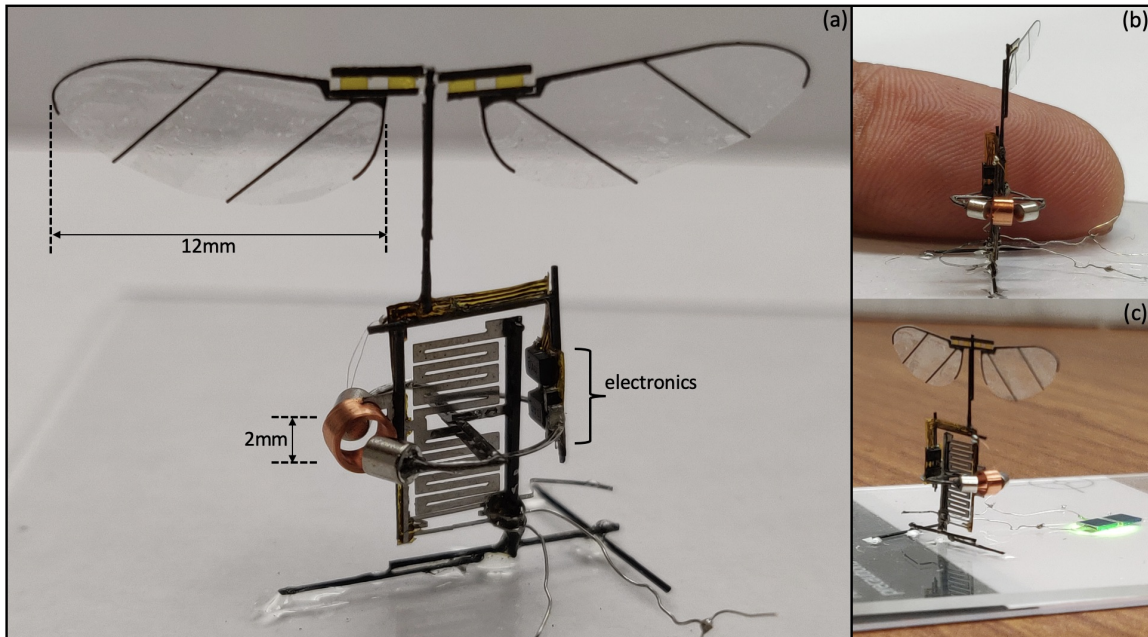


Figure 4.31: Assembled device.

circular trajectory of the coil without any collisions with magnets even for a larger rotation amplitude (compared to our target value of  $\pm 60^\circ$ ).

Table 4.6: Mass distribution of the laser-powered flying  $\mu$ bot.

Sub-component	Mass
Electrical parts	
Power electronics	9mg
Coil	13mg
Magnet	2 × 24mg
PV cell	8mg
Structural parts	
Frames & supports	15mg
Spring	10mg
Wing assembly	2mg
<b>Total</b>	<b>105mg</b>

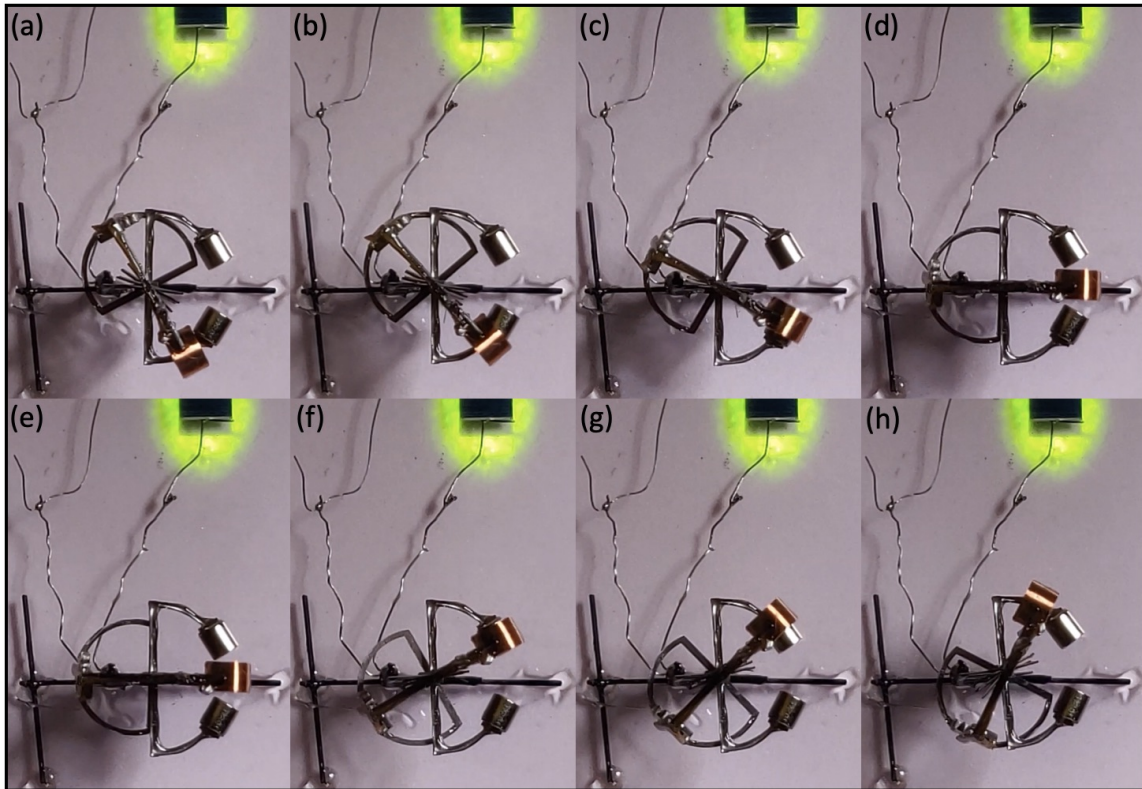


Figure 4.32: Snapshots of the device without wings in motion.

## 4.16 Flapping Motion Using Photovoltaics (With Wings)

We encountered a problem while trying to wirelessly power the device with added wings, so this work is still ongoing. With the wings added the device isn't able to reach the full  $\pm 60^\circ$  oscillation amplitude. This is due to the heating of the PV cells from the IR laser light. The manufacturer specifies the cell's operation and power output at  $25^\circ\text{C}$ , but in practice this temperature exceeds well over  $100^\circ\text{C}$  within a few seconds after the laser is turned on. This causes the power output of the cell to drastically reduce and the coil goes only half the amplitude to around  $\pm 30^\circ$  (see Fig. 4.33).

## 4.17 Summary

In this chapter we designed a 70mg, 3cm wing-span, flapping wing  $\mu$ bot capable of generating up to 60mg of lift using an electromagnetic actuator with low-voltage input ( $\approx 5.5\text{V}$ ). Its design had the actuation and transmission integrated into a single resonant mechanism, and

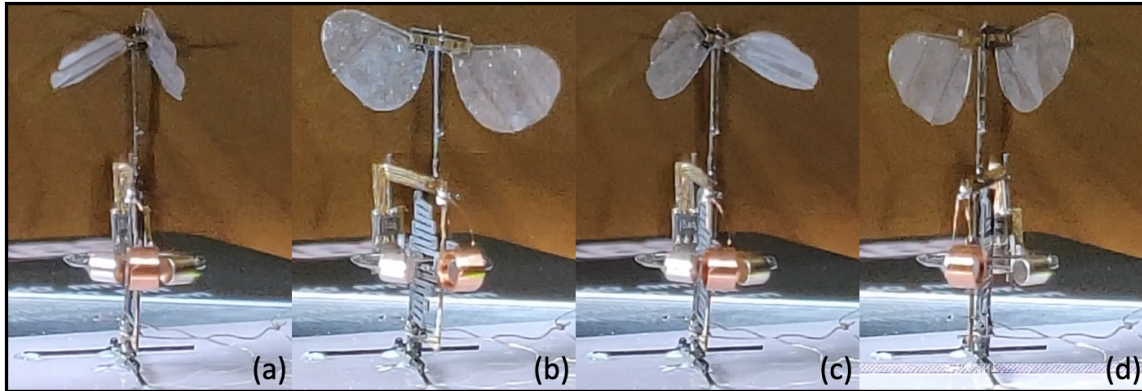


Figure 4.33: Snapshots of the device with wings in motion.

thus it didn't require any small-linear-displacement amplifying stages seen in other works. It produced  $\pm 45^\circ$  wing strokes and  $\pm 45^\circ$  wing pitch at 98Hz operation mimicking relevant insects at this size scale. With a required input power of only 250mW, it is the most energy efficient electromagnetic design at the sub-100mg scale reported to date, and by an order of magnitude.

To drive our actuator we then developed a 9mg power electronics unit that was able to excite the electromechanical system at its true resonant frequency. Apart from being  $10\times$  lighter than the power electronics unit reported for all other flapping wing  $\mu$ bot research, it also consumes  $10\times$  lower power than the actuator whereas all other works consume an order of magnitude more power than the actuator. This makes it 2 orders of magnitude more efficient than all other power electronics units used in flying  $\mu$ bots.

## Chapter 5

# Sub-milligram Flapping Wing $\mu$ bot

We end our contributions on a positive note by giving a very optimistic view of what is possible in the future. This is done, of course, by designing a very futuristic  $\mu$ bot - one weighing less a milligram but still able to mimic insect wing kinematics.

Majority of milligram-scale flapping wing devices reported till date lie in the 100mg mass range [31, 44, 6, 26, 25], with one weighing 3mg [45] but aimed as an actuator for 100mg-scale devices with  $\approx 3$ cm wing spans. This is in part because to mimic insect wing kinematics one needs to produce large wing strokes. It is very tough to do so using other designs like the SCM based fabrication reported in [44] because they are already at  $\approx 70\mu\text{m}$  feature sizes to amplify small piezo displacements for 100mg-scale vehicles and going further down to accommodate for even smaller piezo motion is non-trivial. The work reported here is at  $100\mu\text{m}$  feature sizes (excluding the wing) even at 1mg-scale.

### 5.1 Electromagnetic Actuator

The actuation scheme used is the same magnet-coil system from before but scaled down. The magnet used is Neodymium grade N52 with a height of 0.5mm and a diameter of 0.3mm. The coil is made out of  $25\mu\text{m}$  Copper wire with  $2 \times 14$  number of windings and is 0.45mm in height and has 0.45mm internal diameter. We set the radius of the arc the magnet should move in at  $r = 1.4$ mm to provide sufficient clearance between the magnet and the coil. We use a torsion spring to restrict the motion of the magnet along the desired circular arc (see Figs. 5.1, 5.2).

Fruit flies at similar size scales have wing stroke frequencies around  $\approx 200$ Hz and wing mass around  $\approx 5\mu\text{g}$  [41]. However, the lightest wings we can currently manufacture weigh  $4\times$  times as much (see Table 5.2). Thus, our wing resonance frequency will be approximately half that of the fruit fly. In order to operate the wing quasi-statically we need wing stroke frequency  $\ll$  wing resonance frequency [37, 15, 42], and so we scale down the wing stroke frequency by a factor of  $2\times$  to be near 100Hz.

In order for the magnet-spring system to have a target resonance frequency of, say,

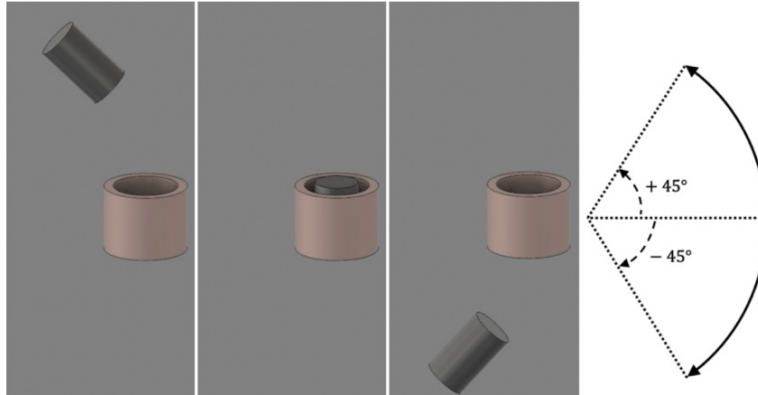


Figure 5.1: Magnet motion. The desired circular arc the magnet should move in. The motion is simple harmonic in the magnet’s rotation angle with  $\pm 45^\circ$  amplitude.

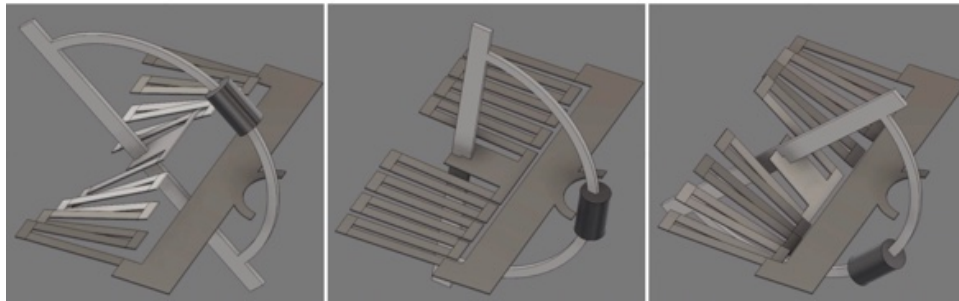


Figure 5.2: Spring motion. The designed torsion spring in its extreme top, neutral, and extreme bottom positions. This shows the intended circular trajectory of the magnet.

$f = 130\text{Hz}$ , the torsional stiffness of the spring should be  $m_{magnet}r^2(2\pi f)^2 = 0.34\mu\text{Nm}$ . To take into account additional inertia of the glue and frames we choose spring stiffness to be  $0.8\mu\text{Nm}$  to be on the safe side. We can always tune down the resonance frequency post-fabrication by adding more mass via glue.

Torsion spring of the desired stiffness is fabricated using the procedure outline in the previous chapter. The material used here is a  $12.7\mu\text{m}$ -thick stainless-steel sheet which is laser cut to make the planar spring. The dimensions of the spring are optimized using 3D FEA simulations such that there is negligible parasitic off-axes motions and resonances. Resulting spring dimensions are reported in Table 5.1.

## 5.2 Wing Fabrication

Wing design is similar to that reported in [44, 6] with flexures included for passive wing pitch. However, there is one key difference. In order to minimize the wing’s rotational

Table 5.1: Spring specifications.

# parallel beams	16
Length of each beam	1mm
Beam width	0.1mm
Beam thickness	12.7 $\mu$ m

inertia (to maximize wing resonance frequency), the veins are made from a single layer of 30 $\mu$ m-thick unidirectional carbon fiber (uni-CF) sheet (30 $\mu$ m was the thinnest CF prepreg sheet we could obtain), as opposed to from a thicker sheet with multiple cured layers with each layer's fibers running along different directions. Due to this design choice we need to ensure that fibers always run along the vein direction in order to strengthen it since uni-CF is weak along the transverse direction.

A 18 $\mu$ m-thick adhesive sheet is first bonded to the uni-CF sheet. We then laser cut the uni-CF such that the leading edge and all the veins are 30 $\mu$ m wide and aligned in the same direction (see Fig. 5.3(a)). 30 $\mu$ m was found to be the narrowest beam we could cut using our UV laser cutter. The veins are placed in the final orientation and then bonded to a 1.5 $\mu$ m polyester membrane using the previously applied adhesive layer (see Fig. 5.3(b)). This assembly is then laser cut to form flexures along the leading edge from the same membrane material (see Fig. 5.3(c)), and the wing is released. The wing length is chosen to be 3.5mm in order to be of similar size to similar sized insects [41]. The shape is chosen for the wing to have an aspect ratio of  $\approx 3$ .

For the wings to deflect by a maximum of 1rad  $\approx 60^\circ$ , the flexure stiffness should be the same as the maximum aerodynamic torque experienced by the wing along the leading edge. Assuming the center of pressure to be 0.4mm away from the leading edge, and the maximum normal force seen by a single wing to be  $= 0.5 \cdot \sqrt{2} \cdot (\text{average lift} = 0.01\text{mN}) = 0.007\text{mN}$ , the maximum aerodynamic torque is estimated at 0.0028 $\mu$ Nm. For a  $w$ -wide and  $l$ -long flexure of  $t = 1.5\mu\text{m}$  thick polyester membrane with an elastic modulus of  $E = 2.5\text{GPa}$ , the stiffness is given by  $\frac{E}{12}t^3\frac{w}{l}$ . This gives one possible desired flexure width = 390 $\mu$ m and flexure length = 100 $\mu$ m. To eliminate any off-axis twisting torques that may be caused by the aerodynamic loading, the flexure is made in 3 parts each 130 $\mu$ m wide and spread out throughout the leading edge of the wing (see Fig. 5.3(c)), thus ensuring the flexure only bends along a single axis.

### 5.3 Assembly

See Fig. 5.4. The planar steel spring in the xy-plane is glued to a 0.28mm diameter CF rod for eventual ease of device handling and mounting. The steel spring has a curved slot in it to position the coil. A planar D-shaped 50 $\mu$ m-thick laser-cut Aluminum frame in the yz-plane is glued perpendicularly to the spring. This D-frame has a gap in the middle of its curved part to insert the magnet. The coil and the magnet with their axis along  $z$  are glued to the

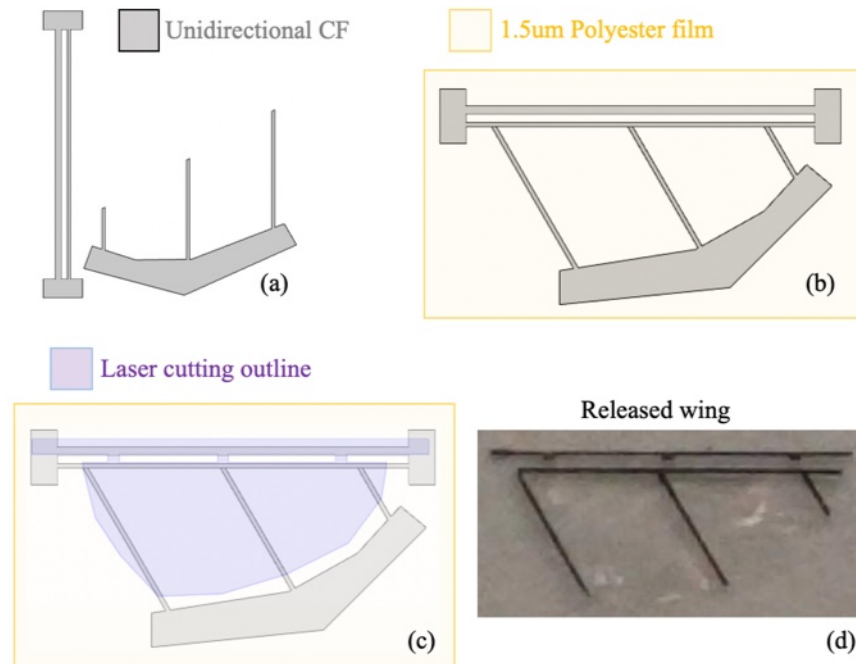


Figure 5.3: Steps of wing fabrication. (a) CF veins are laser cut from a unidirectional single layer  $30\mu\text{m}$ -thick CF sheet. The fibers are oriented vertically. (b) Laser cut veins are aligned and adhered to a polyester film using  $18\mu\text{m}$ -thick adhesive layer. (c) The resulting sandwich is laser cut to remove the excess CF and to form the flexures. (d) Released wing.

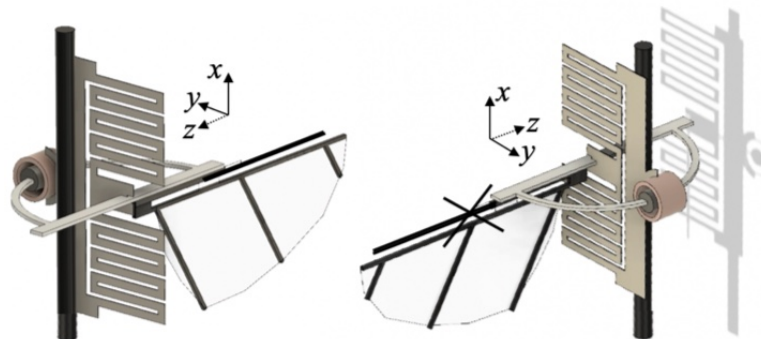


Figure 5.4: Assembled device, animation. Axes defined with respect to the assembled body. The shadow shows the concentricity of the coil and the magnet, and the clearance between them.

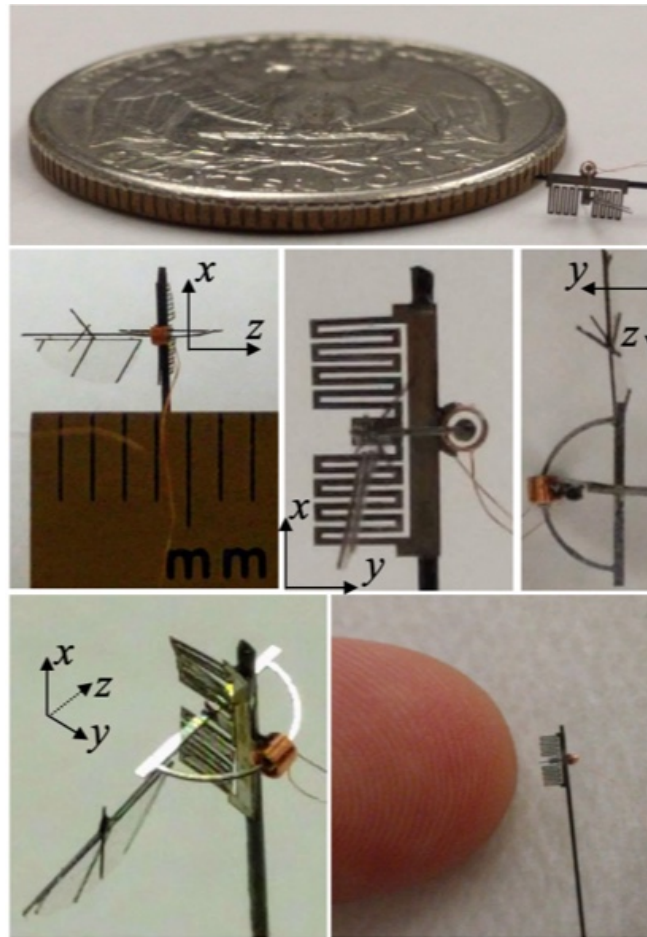


Figure 5.5: Assembled device. (Top) Comparison with a quarter dollar coin. (Middle) Front, side and top views of the device. Front viewed is pictured with a millimeter ruler. (Bottom) Perspective view of the device, and comparison with an index finger.

spring and frame, respectively, so that they are concentric while in spring's neutral position. The wing in the  $xz$ -plane is glued to the straight part of the D-frame at the flexure's top supporting edge. A thin X-shaped CF frame is glued on to the flexure's top supporting edge to limit the wing pitch amplitude. The segments of the X-frame collide with the central wing vein when the wing plane approaches a certain pitch value in either direction. This stops the flexure and wing plane from rotating any further. The coil is connected to a standard function generator. The mass distribution of the assembled device is reported in Table 5.2, and different views of the device is shown in Fig. 5.5.

Table 5.2: Mass distribution.

Coil	0.25mg
Magnet	0.26mg
Spring	0.15mg
D-frame	0.05mg
Wing	0.02mg
Net	0.7mg

## 5.4 Flapping Motion Using External Power

The coil is driven by a square wave and the motion of the device is observed using strobe lights under a microscope. For simplicity, and to reduce the number of steps in the assembly, only one wing is attached to the actuator. Resonance is observed at 132.3Hz, and a  $\pm 45^\circ$  wing stroke is achieved with a  $\pm 70$ mV applied square wave voltage (see Fig. 5.6). A wing pitch of  $+30^\circ/-50^\circ$  is observed with pitch magnitude maximums at neutral stroke angle and zero pitch at extreme stroke angles (see Fig. 5.7). The asymmetry in wing pitch is due to manual assembly imperfections like the wing plane not being perfectly in the xz-plane and the placement of the X-frame. Wing pitch reversal can be observed at extreme stroke angles (see Fig. 5.8). The X-frame can be seen in action when the wing plane tries to pitch more than the set limit (see Fig. 5.9).

The resistance of the coil is  $\approx 1.5\Omega$  meaning Joule heat loss is  $\approx (0.07)^2 \cdot 1.5 = 3.3$ mW. Fruit flies have a body-mass-specific power of  $\approx 29$ W/kg [38] meaning that for producing  $\approx 1$ mg of lift a mechanical power of  $\approx 29\mu$ W is required. We noticed in the previous chapter that since the wing shape and trajectory aren't optimized, the lift generated is about 60% the designed value and the mechanical power consumed is 1.6 times than was theoretically needed to generate the designed lift. We expect a similar behavior here since this work is a miniaturized version of the previous chapter. Thus, with a single wing, we expect a mechanical power output of  $23\mu$ W generating 0.3mg of lift. Presently we lacked the capacity to measure  $\approx 0.1$ mg lift forces. The above figures give the estimated electromechanical efficiency of our device as 0.7%.

## 5.5 Summary

In this chapter we designed the first sub-milligram flapping wing vehicle able to mimic insect wing kinematics. Wing stroke amplitude of  $90^\circ$  and wing pitch amplitude of  $80^\circ$  was demonstrated. Assembly was made simple through use of planar parts with high feature sizes. It required gluing together 5 components in contrast to higher part count and intensive assembly of other milligram-scale  $\mu$ bots. This increased the fabrication speed and success-rate of the fully fabricated device. Low operational voltages (70mV) made testing further easy. It is the smallest wing-span (single wing length of 3.5mm) device reported yet and is at

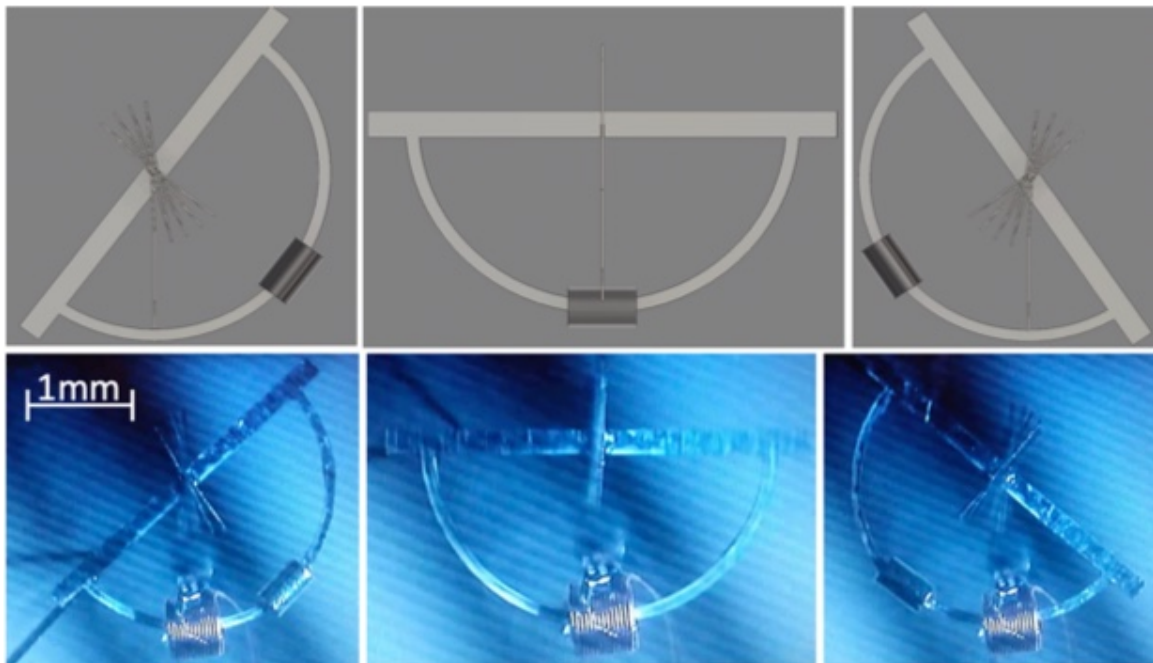


Figure 5.6: Magnet motion snapshots, top view. Extreme right, neutral, and extreme left positions of the moving magnet plus spring system. (Top) An animation of magnet and spring positions. (Bottom) Snapshots of the fabricated device in motion, with Copper coil being stationary.

the same mass-scale as a fruit fly. It is 2 orders of magnitude lighter than all other flapping wing devices reported till date. The artificial wings too are the lightest reported yet but are still heavier than wings of similar sized insects.

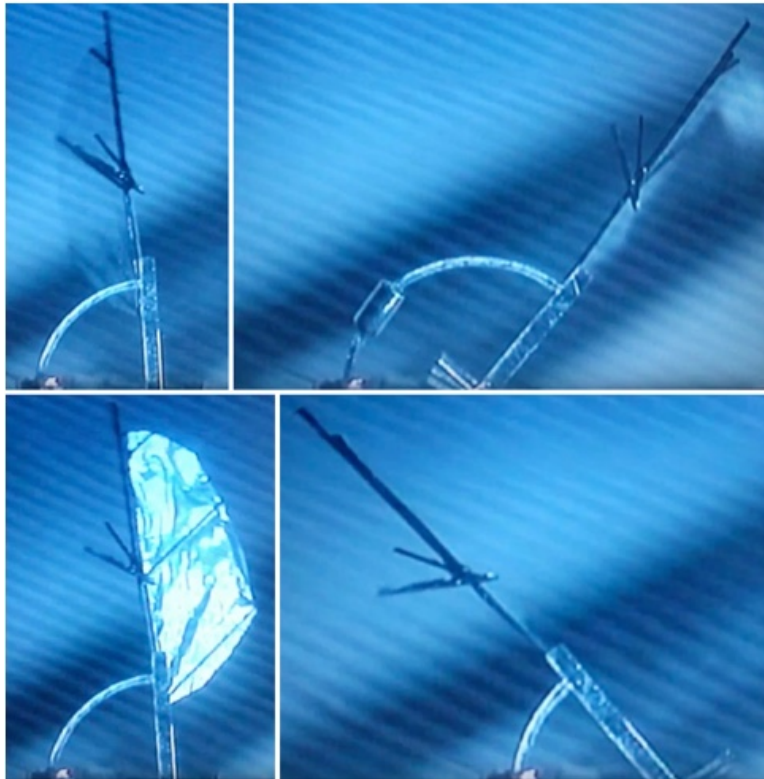


Figure 5.7: Wing pitch, top view. (Top) Positive wing pitch (that is, positive angle of attack) while moving to the right. A maximum pitch of  $30^\circ$  is observed. Zero pitch observed at extreme stroke angle. (Bottom) Wing pitch reversed while moving to the left. Maximum pitch of  $50^\circ$  observed. Zero pitch at extreme stroke angle.

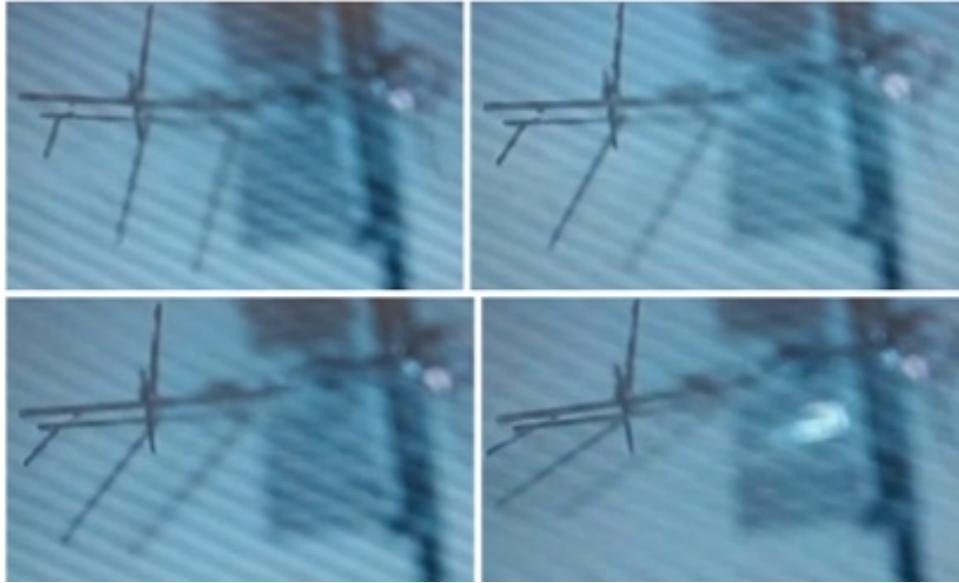


Figure 5.8: Wing pitch, side view. Wing pitch reversal at the end of a stroke cycle (that is, near an extreme stroke angle). The X-shaped CF frame stops the wing from pitching further after reaching a certain angle of attack. This limiting can be seen more clearly in Fig. 5.9.



Figure 5.9: Wing pitch, front view. Wing pitch amplitude increases as the mechanism's stroke speed increases. The X-shaped CF frame hard-limits the pitch magnitude.

## Chapter 6

# Conclusion and Future Work

In this chapter we note some logic next steps and scope for improvements for the  $\mu$ bots designed in this dissertation. Though we note that the eventual deployment of autonomous  $\mu$ bots will need significant strides in milligram-scale batteries, low-power controllers/computers, sensors, and communication modules, this chapter again mainly talks about potential improvements in the mechanical and electrical domains.

### 6.1 Rolling $\mu$ bot

We first designed an insect-sized rolling  $\mu$ bot that could be powered either using photovoltaic cells or supercapacitors. The supercapacitor powered robot could roll freely for 8 seconds after a single charge and is the lightest and fastest self-sufficient rolling  $\mu$ bot reported yet, to the best of our knowledge.

#### Future work

The wheels and the supporting structures in the robot weighed 40mg and can be made much lighter by using carbon fiber or using the material more sparsely. The bot could be made to consume an even lower power if the electronics could function below 1V, but we didn't find any lower voltage light-weight opamps.

The mechanical work done by the actuator to overcome the mechanical losses in the mechanism was negligible compared to the Joule heat loss in the coil. This Joule heat loss is independent of the actuator frequency. Thus, the wheels can be made to rotate much faster simply by increasing the operating frequency of the actuator, and still consume almost the same amount of power while rolling forwards much faster.

The proposed double-ratchet can work with any other actuator and convert small periodic motions to continuous rotation. Using the same principles, one can make a much smaller rolling robot as well but we expect the availability of off-the-shelf power electronics components to be very restricting at smaller scales, and custom chips would have to be made.

## 6.2 Jumping $\mu$ bot

Next we designed an insect-sized jumping  $\mu$ bot that could be powered using onboard photovoltaic cells illuminated by an external infrared laser source. It could jump up by 8mm and is the lightest untethered jumping  $\mu$ bot with onboard power source that has been reported yet.

### Future work

Just like in the case of our rolling  $\mu$ bot, the design of this  $\mu$ bot can in principle work with other small-displacement linear actuators as well. The moment arm of the bot can be made longer, or the shaft can be made narrower, to increase leverage and store more spring energy and thus jump up higher. Further, adding a horizontal component to the launch velocity can help the bot navigate around. The bot can be made more 'flat' (like a coin) to lower its center-of-mass and to ensure that it lands on either one of its bottom or top faces, and is thus always in the correct position to make the next jump.

Instead of pointing the laser manually over the 2 cells, we can add an electronics unit similar to the one in our rolling  $\mu$ bot to provide alternating voltage to the coil. This electronics unit can also be used with an onboard power source like a micro-cell or a supercapacitor (like in the rolling  $\mu$ bot) to enable completely self-sufficient jumps.

## 6.3 Flying $\mu$ bot

Then we designed a flapping wing  $\mu$ bot capable of generating up to 90% of its weight in lift using an electromagnetic actuator. With a required input power of 250mW, it is the most energy efficient electromagnetic design at the sub-100mg scale reported to date, and by an order of magnitude. To drive this actuator we then developed an electronics unit that is an order of magnitude lighter and 2 orders of magnitude more efficient than all other power electronics units that have been reported yet for flapping wing  $\mu$ bots.

### Future work

We encountered a problem with the heating of the PV cells which drastically reduced their power output and was unable to drive our actuator the full amount. But if we had an ideal battery and heating were not a problem our  $\mu$ bot is promising enough to consume low power to generate sufficient lift. Our next experiments will thus be to power this  $\mu$ bot using the same electronics but power it using a solar cell that functions under standard solar illumination and hence won't heat up as much.

## 6.4 Sub-milligram flying $\mu$ bot

Lastly we designed the first sub-milligram flapping wing vehicle able to mimic insect wing kinematics. It is the smallest wing-span device reported yet, is at the same mass-scale as a fruit fly, and is 2 orders of magnitude lighter than all other flapping wing devices reported till date.

### Future work

We estimated the lift generated by the device, but a sensitive anemometer can be used to precisely measure the lift in future work. Current battery technology and power electronics are just barely ready for even 100mg-scale devices so autonomous flight for 1mg-scale devices will have to wait. The efficiency of fruit fly muscles is  $\approx 17\%$  which is an order of magnitude higher than our actuator [38]. So meanwhile we can put our efforts in developing more efficient actuators to be ready for newer batteries and power electronics units, and also design appropriate sub-100 $\mu$ g sensors and controllers for these devices.

The milligram-scale devices mimic insect wing kinematics to function, but can in turn also provide insights and help study aerodynamics at small scales. The device presented here will enable, for the first time, an active study and exploration of flight at the fruit fly scale which is at a low Reynolds number of  $\approx 100$ .

# Bibliography

- [1] D.M. Aukes et al. “An Analytic Framework for Developing Inherently-Manufacturable Pop-up Laminate Devices”. In: *Smart Materials and Structures* 23.9 (2014), p. 094013.
- [2] S.S. Baek, K.Y. Ma, and R.S. Fearing. “Efficient resonant drive of flapping-wing robots”. In: *IEEE Int. Conf. Intelligent Robots and Systems, St. Louis, MO* (Oct. 2009).
- [3] S. Bergbreiter. “Effective and efficient locomotion for millimeter-sized microrobots”. In: *IROS, Nice, France* (Sept. 2008).
- [4] P. Bhushan and C.J. Tomlin. “An Insect-scale Self-sufficient Rolling Microrobot”. In: *submitted to Robotics and Automation Letters* (2019).
- [5] P. Bhushan and C.J. Tomlin. “Design of the first sub-milligram flapping wing aerial vehicle”. In: *MEMS, Seoul, South Korea* (Jan. 2019).
- [6] P. Bhushan and C.J. Tomlin. “Milligram-scale Micro Aerial Vehicle Design for Low-voltage Operation”. In: *IROS, Madrid, Spain* (Oct. 2018).
- [7] C.T. Bolsman, J.F.L. Goosen, and F. van Keulen. “Design overview of a Resonant Wing Actuation Mechanism for Application in Flapping Wing MAVs”. In: *Int. Journal of Micro Air Vehicles* 1.4 (2009).
- [8] C.T. Bolsman, J.F.L. Goosen, and F. van Keulen. “Insect-Inspired Wing Actuation Structures Based on Ring-type Resonators”. In: *Active and Passive Smart Struct. and Integrated Sys.* 6928 (2008).
- [9] C.T. Bolsman et al. “The Use of Resonant Structures for Miniaturizing FMAVs”. In: *MAV07* (Sept. 2007).
- [10] K. Braam and V. Subramanian. “A stencil printed, high energy density silver oxide battery using a novel photopolymerizable poly(acrylic acid) separator”. In: *Advanced Materials* 27 (2015), pp. 689–694.
- [11] D. Campolo et al. “Can DC Motors Directly Drive Flapping Wings at High Frequency and Large Wing Strokes?” In: *IEEE Trans. on Mechatronics* (Feb. 2014), pp. 109–120.
- [12] W.A. Churaman, A. P. Gerratt, and S. Bergbreiter. “First leaps toward jumping microrobots”. In: *IROS, San Francisco, CA, USA* (Sept. 2011).

- [13] W.A. Churaman et al. “The first launch of an autonomous thrust-driven microrobot using nanoporous energetic silicon”. In: *J. Microelectromech. Syst.* 21 (2012), pp. 198–205.
- [14] D.S. Contreras, D.S. Drew, and K.S.J. Pister. “First steps of a millimeter-scale walking silicon robot”. In: *19th International Conference on Solid-State Sensors, Actuators and Microsystems* (2017), pp. 910–913.
- [15] M. H. Dickinson, F.-O. Lehmann, and S. P. Sane. “Wing rotation and the aerodynamics basis of insect flight”. In: *Science* 284 (1999), pp. 1881–2044.
- [16] B.R. Donald et al. “An untethered, electrostatic, globally controllable MEMS micro-robot”. In: *Journal of Microelectromechanical Systems* 15.1 (2006), pp. 1–15.
- [17] C. P. Ellington. “The aerodynamics of hovering insect flight. I. The quasi-steady analysis”. In: *Philosoph. Trans. Roy. Soc. London. Ser. B, Biol. Sci.* 305 (1984), pp. 1–15.
- [18] C. P. Ellington. “The aerodynamics of hovering insect flight. II. Morphological parameters”. In: *Philosoph. Trans. Roy. Soc. London. Ser. B, Biol. Sci.* 305 (1984), pp. 17–40.
- [19] C. P. Ellington. “The novel aerodynamics of insect flight: applications to micro-air vehicles”. In: *The Jour. of Exp. Biol.* 202 (1999), pp. 3439–3448.
- [20] R.S. Fearing et al. “Wing transmission for a micromechanical flying insect”. In: *IEEE International Conference on Robotics and Automation (Cat. No. 00CH37065)* 2 (2000), pp. 1509–1516.
- [21] J. Greenspun and K.S.J. Pister. “First leaps of an electrostatic inchworm motor-driven jumping microrobot”. In: *Hilton Head Solid-State Sensors, Actuators, and Microsystems Workshop, Hilton Head Island, SC* (June 2018).
- [22] L. Hines, D. Campolo, and M. Sitti. “Liftoff of a Motor-Driven, Flapping-Wing Microaerial Vehicle Capable of Resonance”. In: *IEEE Trans. on Robotics* 30.1 (Feb. 2014), pp. 220–232.
- [23] S. Hollar et al. “Solar powered 10 mg silicon robot”. In: *MEMS, Kyoto, Japan* (2003).
- [24] N.T. Jafferis et al. “Multilayer laminated piezoelectric bending actuators: design and manufacturing for optimum power density and efficiency”. In: *J. Smart Materials and Structures* 25.5 (2016).
- [25] N.T. Jafferis et al. “Untethered Flight of an Insect-Sized Flapping-Wing Microscale Aerial Vehicle”. In: *Nature* 570 (2019), pp. 491–495.
- [26] J. James et al. “Liftoff of a 190 mg Laser-Powered Aerial Vehicle: The Lightest Untethered Robot to Fly”. In: *IEEE Int. Conf. on Robotics and Automation, Brisbane, Australia* (May 2018).

- [27] M. Karpelson, G-Y. Wei, and R.J. Wood. “A Review of Actuation and Power Electronics Options for Flapping-Wing Robotic Insects”. In: *IEEE Int. Conf. on Robotics and Automation, Pasadena, CA* (May 2008).
- [28] M. Karpelson et al. “Design and Fabrication of Ultralight High-Voltage Power Circuits for Flapping-Wing Robotic Insects”. In: *Applied Power Electronics Conf., Fort Worth, TX* (Mar. 2011).
- [29] J. Koh et al. “A Jumping Robotic Insect Based on a Torque Reversal Catapult Mechanism”. In: *IROS, Tokyo, Japan* (Nov. 2013).
- [30] Z. Liu et al. “Lateral Moving of an Artificial Flapping-Wing Insect Driven by Low Voltage Electromagnetic Actuator”. In: *MEMS* (Jan. 2016), pp. 777–780.
- [31] K. Ma et al. “Controlled Flight of a Biologically Inspired, Insect-Scale Robot”. In: *Science* 340 (2013), pp. 603–607.
- [32] A. Ostfeld et al. “High-performance flexible energy storage and harvesting system for wearable electronics”. In: *Nature Scientific Reports* 6.26122 (2016).
- [33] I. Penskiy and S. Bergbreiter. “Optimized electrostatic inchworm motors using a flexible driving arm”. In: *Journal of Micromechanics and Microengineering* 23.1 (2012), pp. 1–12.
- [34] R.S. Pierre, W. Gosrich, and S. Bergbreiter. “A 3D-printed 1 mg legged microrobot running at 15 body lengths per second”. In: *Hilton Head Solid-State Sensors, Actuators, and Microsystems Workshop, Hilton Head Island, SC* (June 2018).
- [35] M. Qi et al. “A fast-moving electrostatic crawling insect”. In: *MEMS, Las Vegas, NV* (Jan. 2017).
- [36] K. Saito et al. “Miniaturized Rotary Actuators Using Shape Memory Alloy for Insect-Type MEMS Microrobot”. In: *Micromachines*, 7(4): 58 (2016).
- [37] S. P. Sane and M. H. Dickinson. “The aerodynamic effects of wing rotation and a revised quasi-steady model of flapping flight”. In: *The Jour. of Exp. Biol.* 205 (2002), pp. 1087–1096.
- [38] M. Sun and J. Tang. “Lift and power requirements of hovering flight in *Drosophila virilis*”. In: *The Jour. Of Exp. Biol.* 205 (2002), pp. 2413–2427.
- [39] T. Tantanawat and S. Kota. “Design of Compliant Mechanisms for Minimizing Input Power in Dynamic Applications”. In: *Journal of Mech. Design* 129 (2007), pp. 1064–1075.
- [40] B.P. Trease, Y.-M. Moon, and S. Kota. “Design of Large-Displacement Compliant Joints”. In: *Journal of Mech. Design* 127 (2005), pp. 788–798.
- [41] S. Vogel. “Flight in *Drosophila*. I. Flight Performance of Tethered Flies”. In: *The Jour. Of Exp. Biol.* 44 (1966), pp. 567–578.

- [42] J. P. Whitney and R. J. Wood. “Aeromechanics of passive rotation in flapping flight”. In: *J. Fluid Mech.* 660 (2010), pp. 197–220.
- [43] J.P. Whitney et al. “Pop-up book MEMS”. In: *J. Micromech. Microeng.* 21.11 (2011), p. 115021.
- [44] R.J. Wood. “Liftoff of a 60mg flapping-wing MAV”. In: *IROS, San Diego, CA* (Oct. 2007).
- [45] X. Yan, M. Qi, and L. Lin. “Self-Lifting Artificial Insect Wings via Electrostatic Flapping Actuators”. In: *Proceedings of 28th IEEE Micro Electro Mechanical Systems Conference* (Jan. 2015), pp. 22–25.
- [46] X. Yan et al. “Low Voltage Electromagnetically Driven Artificial Flapping Wings”. In: *MEMS* (Jan. 2016), pp. 1149–1152.
- [47] R. Yeh, S. Hollar, and K.S.J. Pister. “Single mask, large force, and large displacement electrostatic linear inchworm motors”. In: *Journal of Microelectromechanical Systems* 11.4 (2002), pp. 330–336.
- [48] Y. Zou, W. Zhang, and Z. Zhang. “Liftoff of an Electromagnetically Driven Insect-Inspired Flapping-Wing Robot”. In: *IEEE Transactions on Robotics* 32.5 (Oct. 2016).